

School of Science
Department of Physics and Astronomy
Master Degree in Physics

Validation of the “full White Rabbit” setup in the context of the KM3NeT experiment

Supervisor:
Prof. Annarita Margiotta

Submitted by:
Francesco Benfenati

Co-supervisor:
Dr. Tommaso Chiarusi

Academic Year 2020/2021

Contents

List of Figures	ix
List of Tables	xi
Abstract	xiii
Sommario	xv
1 Neutrino astronomy	1
1.1 Neutrinos	2
1.1.1 Neutrino interaction	2
1.1.2 Neutrino oscillation	7
1.2 Cosmic Rays	10
1.2.1 Energy spectrum	10
1.2.2 Cosmic rays below the <i>knee</i>	11
1.2.3 Galactic accelerators	18
1.2.4 Cosmic rays above the <i>knee</i>	19
1.2.5 Ultra High Energy Cosmic Rays	20
1.3 Atmospheric neutrinos	23
1.4 Astrophysical neutrinos and γ -rays	24
1.4.1 γ -ray production mechanisms	25
1.4.2 Neutrino production mechanisms	26
1.4.3 Neutrino and γ -ray Astronomies	27
1.4.4 Neutrino fluxes	28
1.4.5 Astrophysical neutrinos detection	30
1.5 Multi-messenger astrophysics and gravitational waves	32
2 Neutrino telescopes	35
2.1 High-energy neutrino detection	36
2.1.1 Cherenkov radiation	37
2.2 Neutrino signatures	39
2.2.1 Muon neutrino track-like events	40
2.2.2 Shower-like events	41
2.3 Background sources	43
2.3.1 Environmental background	43
2.3.2 Physical background	45
2.4 The KM3NeT experiment	46
2.4.1 ORCA and ARCA sites	47

2.4.2	Digital Optical Modules	48
2.4.3	Detection Units	50
3	KM3NeT Trigger and Data Acquisition layout	53
3.1	Data acquisition network	53
3.1.1	Data acquisition processes	55
3.2	Central Logic Board	57
3.2.1	Central Logic Board Hardware	58
3.2.2	Central Logic Board Firmware	58
3.3	Data handling	62
3.3.1	Optical and acoustic data channels	62
3.3.2	Monitoring data channel	63
3.4	Time synchronization and network implementation	65
3.4.1	“Broadcast” scenario	65
3.4.2	“Full White Rabbit” scenario	66
3.4.3	Next Generation firmware	70
4	“Full White Rabbit” setup validation	71
4.1	The Bologna Common Infrastructure experimental setup	71
4.2	Pulse Per Second synchronization	76
4.3	Control Unit validation	80
4.3.1	Dockerization of the CU and DAQ processes	80
4.3.2	Downsampling of Slow Control data	82
4.4	Clock synchronization validation	84
4.4.1	OctoPAES boards	84
4.4.2	Clock synchronization validation strategy	86
4.5	Monitoring channel validation	94
4.5.1	Dockerization of the monitoring program	96
4.5.2	Clock reset issue	97
4.5.3	Monitoring of the “full White Rabbit” setup	98
4.5.4	Extension for multiple Detection Units	98
4.6	Result discussion	102
	Conclusions	105
	Acronyms	107
	Bibliography	111

List of Figures

- Figure 1.1 CC Neutrino-nucleon (**left**) and antineutrino-nucleon (**right**) cross-sections divided by neutrino energy, as a function of energy. The plot shows the total cross-sections (black lines) and the various contributing processes: quasi-elastic scattering (QE, red line), resonance production (RES, blue line), deep-inelastic scattering (DIS, green line). For prediction evaluation and plotted data refer to [53], whence the picture is taken. 4
- Figure 1.2 Diagrams of the neutrino-nucleon DIS processes: CC interaction (**left**) with the exchange of a W -boson and NC interaction (**right**) with the exchange of a Z -boson. Four-momenta are also shown. Picture taken from [60]. 5
- Figure 1.3 Neutrino-nucleon (**left**) and antineutrino-nucleon (**right**) CC, NC and total cross-sections as a function of neutrino energy, in the high-energy range. One can notice the linear dependence on the neutrino energy, and the difference between CC and NC cross-sections. For the parton distribution used in the calculations refer to [58], whence the picture has been taken. 6
- Figure 1.4 Neutrino scattering cross sections for different processes as a function of energy. The blue curves indicate neutral-current DIS processes for all neutrino flavors, while the purple and orange curves indicate the charged-current DIS processes for ν_e/ν_μ and ν_τ respectively. Solid curves refer to neutrinos and dashed ones to antineutrinos. The red curve instead refers to the Glashow resonance. The y-axis on the right represents the water equivalent mean free path of these interactions. Picture taken from [68]. 7
- Figure 1.5 All-particle energy spectrum of cosmic rays. Data are taken from the labeled experiments, both of the direct and the indirect kind. Picture taken from [56]. 11
- Figure 1.6 Simulated trajectory of charged CRs in the Galactic magnetic field. Particles of energy up to 10^{18} eV are bent by the magnetic field and undergo a chaotic motion inside the Galactic volume, whereas particles of energy of 10^{19} eV are only feebly deflected. Finally, particles with energy of at least 10^{20} eV travel along almost straight lines, allowing the direct identification of their sources. Picture taken from [91]. 12

- Figure 1.7 In the mechanism on the left-hand side of the figure the acceleration by a moving, partially ionized gas cloud is shown. On the right-hand side instead, the acceleration occurs at a plane shock front: the particle direction is isotropized by the magnetic turbulence both downstream and upstream. Thus, it can eventually cross back the shock from upstream to downstream and start another acceleration cycle. 14
- Figure 1.8 Hillas plot: sources above the top full (dashed) line are able to accelerate protons up to 10^{21} eV (10^{20} eV), while sources above the bottom full line are able to accelerate iron up to 10^{20} eV. Even if they are possible candidates in principle, neutron stars are discarded since we have no evidences of UHECRs emitted from Galactic neutron stars. Picture taken from [54]. 21
- Figure 1.9 Expected neutrino fluxes: the black line represents the expected *conventional atmospheric neutrino* flux and the nearby dashed black lines include the contributions of two different models of *prompt neutrino* fluxes from charmed mesons decays. The full green line constitutes the Waxman and Bahcall upper bound from a diffuse neutrino flux coming from extra-Galactic sources. The dashed green line instead is the upper bound for neutrinos produced in GRBs. Eventually, the blue line shows the possible contribution of cosmogenic neutrinos. Experimental points represent measurements of the atmospheric $\nu_\mu + \bar{\nu}_\mu$ flux as a function of energy by ANTARES, IceCube and AMANDA experiments. Figure taken from [91]. 29
- Figure 1.10 **Left:** deposited energies by neutrinos interacting inside IceCube observed in six years of data. The gray region shows uncertainties on the sum of all backgrounds. Also shown are the atmospheric muons and neutrinos flux and two fits to the spectrum, assuming a simple power-law (solid gray) and a broken power-law (dashed gray). **Right:** the same data and models showing the distribution of events with deposited energy above 60 TeV as a function of the sine of the declination (negative values in the Southern Hemisphere). For details see [16], whence the figure is taken. 31
- Figure 1.11 Unfolded ν_μ energy spectrum for the passing muon sample in IceCube. Data are compared to the best-fit fluxes for the conventional atmospheric neutrino flux and for the astrophysical one: above ~ 100 TeV data are not compatible with the background-only hypothesis. Figure taken from [16]. 31
- Figure 2.1 Schematization of a neutrino telescope as a muon detector deep underground. Down-going muons produced by protons in the atmosphere represent the main background for the detector, together with muons (from any direction) related to atmospheric neutrinos. Only up-going muons coming from astrophysical neutrinos constitute the signal we would like to detect in principle. 37
- Figure 2.2 Path length of muons (μ), taus (τ), electromagnetic (em) and hadronic (had) showers in water as a function of energy. 38

Figure 2.3	Scheme of the Cherenkov radiation. The propagation direction of the charged particle is represented together with the Cherenkov angle θ_C and the wavefronts formed by all the spherical lightwaves produced during the passage of the particle.	39
Figure 2.4	Event signatures of neutrino-induced events in neutrino telescopes. Neutrinos are identified by dashed black lines, muons by orange lines, e^+ , e^- in EM showers by red lines, secondary particles in hadronic showers by blue lines and τ by green lines. In the upper ν_τ CC channel the <i>double-bang</i> signature can be seen.	40
Figure 2.5	Angular resolution as a function of the neutrino energy as simulated with Monte Carlo for the ANTARES neutrino telescope. Triangles represent the average discrepancies between the reconstructed muon and the real muon directions, while circles the discrepancies between the reconstructed muon and the parent neutrino directions. Figure taken from [91].	42
Figure 2.6	Photomultiplier count rate, as function of time, for a typical stream of data collected by ANTARES. The baseline indicates the contributions of the ^{40}K decay and the constant signal from bioluminescence. The dark current count rate of the PMT gives a constant contribute as well. Bursts lasting several seconds are also visible. Figure taken from [15].	44
Figure 2.7	Contributions to muon background as a function of the zenith angle. Direct atmospheric muon fluxes are calculated at two different depths (1680 and 3880 meters of water equivalent), while atmospheric neutrino induced muon fluxes are calculated for two different muon energy threshold: the black lines refers to $E_\mu > 1$ TeV and the red line for $E_\mu > 100$ GeV. Figure taken from [91].	45
Figure 2.8	Geographical location of the KM3NeT/ARCA and KM3NeT/ORCA neutrino telescopes in the Mediterranean Sea. The third site, KM3NeT-Gr, is located off the coast of Pylos in Greece, and at present is used only for validation and qualification. Figure taken from [74].	46
Figure 2.9	Sky coverage of KM3NeT detectors in galactic coordinates. Also shown are some known astrophysical objects. Figure taken from [15].	47
Figure 2.10	Internal structure of a Digital Optical Module. Figure taken from [74].	48
Figure 2.11	Left: an assembled Digital Optical Module. Right: internal view of a DOM during assembling phase (incomplete). Pictures taken at the LNS (Laboratori Nazionali del Sud) in Catania, Italy.	49
Figure 2.12	Left: Schematic view of a Detection Unit with 18 DOMs and buoy on top. Right: Photograph of the launcher vehicle (LOM) containing a DU during sea operations The anchor and the Base Module (the cylinder at the base) can also be seen. Pictures taken from [47].	50
Figure 3.1	Scheme of the network topology implemented in KM3NeT. Figure taken from [80].	54
Figure 3.2	Outline of the DAQ infrastructure and components. Figure taken from [80].	56

Figure 3.3	Pictures of a Central Logic Board (Left) and of a Power Board (Right). Figures taken from [44].	59
Figure 3.4	Block diagram of the embedded Central Logic Board FPGA firmware. Figure taken from [32].	60
Figure 3.5	Internal states of the state machine and events (represented by arrows). Text in italics indicates autonomously issued events, while plain text indicates events issued by the user.	61
Figure 3.6	TTDC channel: optical data in form of UDP packets pass through the DataQueue, the optical DataFilters and to the JLigier, which dispatches it to the Quasi Online Analysis (QUOLAM) clients and to the DataWriter for being finally written on disk.	64
Figure 3.7	Layout of the “Broadcast” networking system. Single (double) lines represent 1 GbE (10 GbE) connections. Single directional data-flows are indicated with arrows, while bidirectional connections have only dots. Figure taken from [46].	66
Figure 3.8	Left: Sketch of the “Broadcast” network architecture. The broadcast signal (red arrows) provided by the WRS-Broadcast (WRS-BR) is split and shared among all the DOMs. The GPS timing is transmitted by the WRS-Bridge to the WRS-BR and through the broadcast signal to the DOMs, together with Slow Control commands. DOM data instead are transmitted via unidirectional fibres towards the DOMs Front End Switch (DFES) which is connected through a standard switch to the computing farm. Right: Sketch of the “full WR” network architecture. In this configuration two <i>Wet</i> WR switches (WWRS) are located inside the Base Module of the DU. Both SC messages and DOM data pass only through the two shore links connected to the WWRS. The Base Module and 12 other DOM links are made redundant via a splitter. In addition, an interlink connects the two WWRS and routes the traffic from one switch to the other in case a switch shore link is lost.	67
Figure 3.9	Network scheme of the Full White Rabbit topology, including redundancy. The particular case for ARCA is shown.	69
Figure 4.1	Layout of the “full WR” setup network topology at the BCI.	72
Figure 4.2	“Full WR” test bench at the BCI in its final configuration. It is formed by 19 CLBs, with OctoPAES boards plugged on, two Wet White Rabbit switches and the power supplies for the CLBs and the switches. Up: setup configuration with OctoPAES in stand alone mode, i. e. operating with their internal clock and with an independent start/stop signal generated by pressing a button on the boards. Bottom: setup configuration with the Kintex KC705 board providing a common start/stop signal to all the OctoPAES and acting as their clock source, with the clock signal distributed in daisy chain.	73
Figure 4.3	Left: The rack-mountable elements (standard DELL switch, Dry White Rabbit switch, GPS, power-supply). Those elements refer to the highlighted red box in the scheme (Right).	75

- Figure 4.4 Oscilloscope fine measurement of the delays between the PPS signal of CLB-9 of the dismantled setup with respect to the signal of the reference CLB-1. The random delays fit with a Gaussian curve with mean and sigma as indicated in the adjacent box. The measurement comprises 2000 events, whereas the sampling frequency was set to 100 ps and the time range was equal to ± 50 ns. Delays follow a Gaussian distribution, whose fit curve is shown in red and whose mean and sigma values are written inside the box. 76
- Figure 4.5 Oscilloscope coarse measurements of the delays between the PPS signal of the CLBs of the dismantled setup with respect to the signal of the reference CLB-1. Measurements comprise 10000 events, with sampling frequency set to 10 ns and time range equal to ± 50 ms. Distributions are completely biased by the poor resolution and by jitter, so that the only relevant information that can be extracted is the fact that all observed delays were smaller than 10 nanoseconds and no delays in the range 10 ns - 100 ms were observed. 77
- Figure 4.6 PPS delay measurement between the PPS signal of CLB-16 of the new configuration of the setup and the signal of CLB-1. This measurement comprises 10000 data points. The red line refers to the Gaussian fit, whose mean and sigma are listed in the box. 78
- Figure 4.7 Oscilloscope measurements of the delays between the PPS signal of the CLBs with respect to the signal of the reference CLB-1. The random delays fit with a Gaussian curve with mean and sigma as indicated in Table 4.1. 79
- Figure 4.8 Basic structure of a docker container. 81
- Figure 4.9 Architecture of the Docker system, composed by the Docker client and the Docker daemon. The Daemon can pull pre-built images from a Docker registry, such as Docker Hub, or push images into it. 82
- Figure 4.10 Some monitoring sensor data (the three components of the accelerometer, the third component of the compass sensor, the temperature and the humidity) retrieved by the SRP (red points) and TMCH channel (blue points) as function of time, from CLB-10 of the “full White Rabbit” setup. In this case, the downsampling was set to one update every 60 seconds. 83
- Figure 4.11 Picture of an OctoPAES electronic board; on the bottom left, the dip switches for selecting the MIF file page and the Large/Small type can be seen. 85
- Figure 4.12 Calibration page in the MIF file. The first column refers to the PMT channels. Hits in the rows are highlighted by the red boxes. 87
- Figure 4.13 Scheme of the 4 \times -oversampling technique. The sampling quadruples the clock frequency using four phases of the original clock, shifted by 90 degrees each, thus obtaining a sampling frequency of 1 GHz when using a clock with a period of 4 ns. Figure taken from [36]. 88
- Figure 4.14 Schematic overview of the connections implemented for the OctoPAES system on the “full WR” setup: the external Kintex KC705 board acts as a master and transmits the clock signal in daisy chain to the OctoPAES (Large ones are labelled with an “L” and Small ones with an “S”) and the start/stop signal in parallel. 88

- Figure 4.15 Representation of the Time Over Threshold, i. e. the time during which the signal voltage is above a voltage threshold. 89
- Figure 4.16 Delays between the hits generated by the OctoPAES boards and timestamped by the respective CLBs. Time differences are computed for each CLB with respect to the hits registered by the CLB-1. On the left-hand plots, the time differences are plotted over time, whereas the right-hand plots shows the relative distribution of delay values. Turn-off/turn-on cycles are highlighted by the pink vertical lines on the plots: in the first four cases, the turn-off and turn-on are so near in time that their lines appear superimposed in the plots; in the last case instead, the turn-off and turn-on moment are visibly separated. 91
- Figure 4.17 L1 hit occurrences distribution over time. Black dashed lines highlights the turn-off and turn-on times of data acquisition, due to the power cycles of the CLBs. Gaps in the distribution within acquisition time, as occurred for some CLBs, indicate that the CLB has lost the clock Track-phase. In some occasions, some CLBs were excluded from the measurements due to issues with cables delivering the start and stop signals for the OctoPAES boards or with the software program: those cases are marked with the “excluded” label in the plot. 92
- Figure 4.18 Time Over Threshold distributions of the L1 hits as emulated by the OctoPAES boards and timestamped by the CLBs. Distributions are centered on 25 ns which is the ToT specified in the MIF file, with a discrepancy of 1 ns due to the TDC resolution. 93
- Figure 4.19 Scheme of the processes behind the TMCH monitoring multiprocesses program. The Python programs, the InfluxDB service and the Grafana service run inside separate containers, managed by the docker-compose tool. 97
- Figure 4.20 Screenshots from the Grafana dashboard representing the plot of the difference $T_{100\text{ms}}$ between two consecutive TMCH packets for CLB-1 of the “Broadcast” setup, when clock reset errors were observed. **Up:** positive and negative peaks with height equal to $T_{100\text{ms}} \simeq 51$ years (time difference between the 01/01/1970 and 07/05/2021) indicate the occurrence of a clock reset. In the shown time frame, 40 occurrences with a more or less regular frequency ($\simeq 2$ min. period) can be seen. **Bottom:** zoom on the time frame between two consecutive positive and negative peaks; after the clock resets to the 01/01/1970 date a negative peak appears, as the time difference between consecutive packets is between 01/01/1970 (current packet) and 07/05/2021 (previous packet). Then packets continue to arrive with the correct frequency, i. e. $T_{100\text{ms}} = 100$ ms while the clock is still back at 01/01/1970, and finally after few seconds the clock comes back to the current date and a positive peak appear, as the time difference between consecutive packets is between 07/05/2021 (current packet) and 01/01/1970 (previous packet). 99

Figure 4.21 Screenshot from the Grafana dashboard representing the plot of the transmission ratio $R_{packet\ time}$ for CLB-1 of the “Broadcast” setup, when clock reset errors were observed. The transmission ratio $R_{packet\ time} = N_{observed}/N_{expected}^{packet\ time}$ which is expected to be equal to one if no issue of any kind is present, drops drastically to zero during a clock reset event, as $N_{expected}^{packet\ time}$ grows sharply. 100

Figure 4.22 Screenshots of Grafana dashboards of the monitoring program. **Up:** plots of T_{100ms} over time for the different CLBs (DOMs). **Bottom:** plots of the transmission ratio $R_{packet\ time}$ over time for the different CLBs. 100

Figure 4.23 Screenshot of a Grafana dashboard of the monitoring program. This dashboard includes a summary of the information about DOMs of a DU: the run number, the synchronization status (Track-phase bit value), the plot of T_{100ms} over time, the delay between the *packet time* and the *machine time*, the clock reset counters, and bar plots showing the total number of arrived TMCH packets and the expected numbers $N_{expected}^{packet\ time}$ and $N_{expected}^{machine\ time}$ 101

Figure 4.24 Screenshot of the panel representing the bit value which refers to the synchronization status of the CLBs. Values of CLB-4 are shown. When the CLB loses the Track-phase, the bit value goes to 0. 101

Figure 4.25 Extension of the monitoring program to multiple Detection Units. 102

List of Tables

Table 3.1	Some of the tags assigned by the JLigier process to specific data streams, along with a brief description. L0, L1 and L2 refers to the three implemented levels of trigger.	63
Table 4.1	Oscilloscope measurement of the delays between the PPS signal of the CLBs with respect to the signal of the reference CLB-1. The measures were made with an oscilloscope Rhode&Schwarz RTO 1044 - 4GHz, acquiring in Real Time acquisition mode with a range of ± 25 ns. The red box highlights the largest value among the delays of all CLBs, which is smaller than the nanosecond.	78
Table 4.2	Delays between signals injected by the OctoPAES “Large” boards on the CLBs. Delays are computed with respect to the reference OP on CLB-1, and are measured with an oscilloscope with 200 ps sampling frequency.	90

Abstract

The newborn Neutrino Astronomy is one of the most promising branches of astroparticle physics. Its main goal is to measure the fluxes of astrophysical neutrinos and to identify their sources, thus allowing us to achieve a better understanding of the sources and the acceleration mechanisms of Cosmic Rays. As a matter of fact, due to their unique physical properties, neutrinos constitute an optimal probe to observe high-energy astrophysical phenomena: they interact exclusively via the Weak Interaction and they are of neutral charge. These properties ensure them the capability of propagating throughout the Universe for very large distances without being absorbed or deflected by magnetic fields along their travel. For this reason neutrino astronomy is expected to become decisive for settling questions about Cosmic Ray sources and acceleration mechanisms which cannot be solved by other means. The detection of astrophysical neutrinos is achieved by the deployment of neutrino telescopes deep under ice or water. From their very beginning in the '60s, huge steps forward have been made, and nowadays the second generation of neutrino telescopes is under construction or development.

The development of my thesis has been carried out within the KM3NeT experiment, which consists in two underwater detectors that are going to be installed in the depths of the Mediterranean Sea, reaching a volume greater than 1 km^3 of sea water instrumented with thousands of optical sensors. Due to the inaccessibility of the underwater sites, the technology used in the detectors must be carefully evaluated and validated with great accuracy before the deployment. For this reason, several laboratories throughout the whole collaboration are deputed to development, test and maintenance of the employed instrumentation. Among them, the Bologna Common Infrastructure (BCI) laboratory already hosts a test bench which includes the entire electronic components of a complete KM3NeT Detection Unit and all the required Data AcQuisition system chain.

The work of this thesis is aimed at the integration and validation of a second test bench at the BCI, based on a different network configuration with respect to the one presently used in the detectors. The new strategy relies on a full standard White Rabbit network and will be adopted in the next forthcoming phase of the experiment. A new setup which recreates a full Detection Unit with all electronic boards and relative Data AcQuisition system resources has been built at the BCI, implementing the “full White Rabbit” network topology. In this context, the validation of the setup represents a focal point for the transition of the experiment towards the next phase. In particular, in this thesis the validation of the time synchronization and of the integrity and stability of optical and monitoring channel data streams will be illustrated.

Sommario

La recente astronomia dei neutrini costituisce una delle più promettenti branche della fisica delle astroparticelle. Lo scopo ultimo di questa disciplina è la misurazione dei flussi di neutrini di natura astrofisica e l'identificazione delle loro sorgenti, facendo in tal modo luce sulla loro natura e sui meccanismi di accelerazione dei raggi cosmici, a cui i suddetti neutrini sono legati. Infatti, in virtù delle loro peculiari proprietà fisiche, i neutrini rappresentano una fonte ottimale e unica di informazione riguardo ai fenomeni astrofisici ad alte energie. Interagendo unicamente tramite interazioni deboli ed avendo carica elettrica neutra, essi possono propagarsi per considerevoli distanze attraverso l'Universo senza essere assorbiti dal materiale interstellare o intergalattico e senza essere deflessi da campi magnetici lungo il loro percorso. Per questo motivo, l'astronomia dei neutrini sarà decisiva al fine di dirimere questioni legate alle sorgenti di raggi cosmici che non possono essere risolte sfruttando altri mezzi. La rivelazione di neutrini astrofisici è ottenuta grazie all'impiego di telescopi di neutrini costruiti in profondità sott'acqua, nei mari o nei laghi, o sotto il ghiaccio. Dalla loro ideazione negli anni '60, enormi passi avanti sono stati fatti nel loro sviluppo e, attualmente, la seconda generazione di telescopi di neutrini è in fase di costruzione o progettazione.

Lo sviluppo di questa tesi è stato portato avanti all'interno dell'esperimento KM3NeT, il quale consiste in due telescopi sottomarini, ARCA e ORCA, in fase di installazione nelle profondità del Mar Mediterraneo, raggiungendo al completamento un volume pari a più 1 km^3 di acqua strumentata con migliaia di sensori ottici. Per via della completa inaccessibilità dei siti subacquei dei rivelatori, la tecnologia utilizzata in questi rivelatori deve essere accuratamente studiata e validata prima dell'installazione. Per questo motivo, diverse strutture sparse fra i Paesi della collaborazione ospitano laboratori dedicati allo sviluppo, al collaudo e al controllo della strumentazione impiegata. Fra questi, un ruolo rilevante è assunto dal laboratorio di Bologna denominato "Bologna Common Infrastructure" (BCI), che già ospita un test bench comprensivo delle componenti di elettronica che costituiscono una Detection Unit dei rivelatori di KM3NeT e di tutte le risorse di calcolo necessarie per il sistema di acquisizione dati.

Il lavoro di questa tesi è incentrato sull'integrazione e la validazione di un secondo test bench nel laboratorio BCI basato su una differente configurazione di network rispetto a quella attualmente presente nei due rivelatori. La nuova architettura prevede l'implementazione di un network standard basato su tecnologia White Rabbit che sarà adottato nella prossima futura fase dell'esperimento. Il nuovo setup costruito simula una Detection Unit comprensiva di schede elettroniche e sistema di acquisizione dati, riproducendo fedelmente la nuova topologia di network che verrà utilizzata. In questo contesto, la validazione del setup rappresenta un punto focale per la transizione dell'esperimento verso la sua prossima fase. In particolare, in questa tesi verrà illustrata

la validazione della sincronizzazione temporale del sistema e dell'integrità e stabilità dei flussi di dati ottici e di monitoraggio provenienti dalle schede elettroniche del setup.

Chapter 1

Neutrino astronomy

One of the major topics in Astrophysics is related to Cosmic Rays (CRs). While to date we have learned a lot about nature and composition of cosmic rays, we still have important gaps in our knowledge of their astrophysical sources and their acceleration mechanisms. With this respect, significative progresses have been made in the last decades with the advent of the first generation of experiments in Space and on Earth able to measure the high-energy and ultra-high-energy range of the γ -ray spectrum. As we will see in this chapter, the production of these γ -rays is foreseen in the acceleration and propagation mechanisms of charged CRs, both of electrons and of protons or heavy nuclei ($Z > 3$). The importance of these neutral probes stains in the fact that their travel towards us follows a straight line, since it is not deflected by the Galactic or Intergalactic magnetic fields, allowing us to trace back directly their production point. The opening of this new window on the CRs study represented a breakthrough in our comprehension of the subject, and from the results of γ -ray measurements we have discovered several classes of either Galactic or extra-Galactic cosmic rays accelerators and sources.

Nevertheless, there are still open questions to which we cannot answer by relying exclusively on the use of photons as probes. For example, γ -rays can be produced both in purely electromagnetic processes, such as the synchrotron radiation emission from relativistic electrons or the Inverse Compton scattering, and in hadronic mechanisms, as in the decays of neutral pions produced in pp processes or in photoproduction processes. In order to discriminate between them, it is necessary to detect particles which are produced exclusively in hadronic mechanisms, like neutrinos generated in the decays of π^\pm, K^\pm resulting from hadronic interactions. Neutrinos share with photons the nature of neutral particles and the advantage of following a straight track between the production and observation points, but unlike photons their interactions in the propagation medium are much less probable, thanks to their intrinsically small cross sections. Therefore, while high-energy photons, starting from an energy of several TeV, interact with the infrared background radiation and the Cosmic Microwave Background (CMB) radiation in the Universe producing an electron-positron pair, and they are partially absorbed by interstellar dust, neutrino absorption from the material across their path in the Universe is much more limited and we can detect neutrinos coming even from very far distances, from extremely dense regions of galaxies or from the innermost structure of astrophysical objects. In other cases they carry complementary informations with respect to the ones brought by photons, playing a crucial role in the so-called “Multi-messenger Astrophysics”.

On the other hand, their small interaction probability represents an issue for their detection in an experiment. This is the reason why large volume detectors with very large masses of target material are needed for this purpose. The necessary technological advancements required in order to build such detectors have been made available only in the last decades, and neutrino telescopes represent one of the most recent and promising branches of Astroparticle physics. In this chapter a brief and non-exhaustive review of the experimental status of high-energy astroparticle physics and its theoretical fundamentals is shown, with particular focus on neutrino's properties and neutrino astronomy.

1.1 Neutrinos

Neutrinos are the most elusive fundamental particles of the Standard Model: they are electrically-neutral leptons with tiny masses compared to all other fermions, and among all the fundamental forces they feel only the weak interaction. The existence of such a particle was firstly hypothesized by W. Pauli in 1930, in a desperate attempt to solve the problem of the apparently missing energy in the β -decay process [79]. The idea immediately convinced Enrico Fermi who in the following years developed a theory, based on the analogy with the Q.E.D., which described the mysterious spectrum of the β -decay as the result of the emission of an electron-neutrino (as he named the new particle) couple from the nucleus. After that, the neutrino remained an hypothetical particle until evidence for its discovery was brought forward by Reines and Cowan in 1956 [85]. Later on, as the theoretical frame of the Standard Model progressed and new leptons, the muon and the tau, were discovered, it became clear that a different neutrino for each flavor must exist: nevertheless, the experimental challenges made the ν_μ and ν_τ discoveries possible respectively only in 1962 [49] and in 2000 [71], adding substantial confirmations of the validity of the Standard Model. However, a discrepancy with the prediction of the Standard Model was found for what concerns the mass of neutrinos: while they should have been massless in principle, the observation of the so-called *neutrino oscillation* phenomenon required the postulate of a non-zero mass. This feature represents nowadays the most promising bridge towards a theory beyond the Standard Model, and the hunt for the absolute values of neutrino masses and their hierarchy is in full swing.

The following section is get inspired by [60].

1.1.1 Neutrino interaction

Neutrino interactions are described in the Standard Model by the proper leptonic charged current and neutral current terms which appear into the weak interaction Lagrangian:

$$\mathcal{L} = \mathcal{L}_{I,L}^{(CC)} + \mathcal{L}_{I,\nu}^{(NC)} = -\frac{g}{2\sqrt{2}} \left(j_{W,L}^\rho W_\rho + j_{W,L}^{\rho\dagger} W_\rho^\dagger - \frac{g}{2\cos\theta_W} j_{Z,\nu}^\rho Z_\rho \right) \quad (1.1)$$

In Eq. 1.1 W_ρ and Z_ρ are the gauge boson fields, whereas $j_{W,L}^\rho$ and $j_{Z,\nu}^\rho$ are respectively the leptonic charged current and the neutrino part of the leptonic neutral current, that

is:

$$j_{W,L}^\rho = 2 \sum_{\alpha=e,\mu,\tau} \bar{\nu}_{\alpha L} \gamma^\rho \ell_{\alpha L} \quad (1.2a)$$

$$j_{Z,\nu}^\rho = \sum_{\alpha=e,\mu,\tau} \bar{\nu}_{\alpha L} \gamma^\rho \nu_{\alpha L} \quad (1.2b)$$

Here, ν_α and ℓ_α are the spinorial fields of neutrinos and charged leptons and the additional subscript L , which stands for the application of the left-handed projector $\frac{(1-\gamma^5)}{2}$, indicates that only the left-handed chiral component of neutrino fields takes part in the interactions, i. e. left-handed chiral neutrinos and right-handed chiral antineutrinos, violating the parity. The evidence of this weak interaction parity violation was brought up by Madame Wu in her famous experiment with the ^{60}Co β -decay in 1956 [96].

In neutrino astronomy, only high-energy neutrinos are involved. In general, when a neutrino interacts with an atom, it can interact either with an orbital electron or with a nucleon. Nevertheless, the neutrino-nucleon interaction is dominant at high-energies, with the only exception of the Glashow resonance occurring at the PeV scale, and therefore neutrino-nucleon interactions are the ones we are most interested in when studying astrophysical neutrinos. Moreover, the introduction of the aforementioned neutrino masses generates only small kinematical effects in neutrino interaction processes, so that we can safely neglect them in this description.

Neutrino-nucleon interactions

Neutrinos can interact with nucleons through different processes, whose contributions are shown in Fig. 1.1: below 1 GeV the dominant contribution comes from the *quasi-elastic* scattering process (QE) in which the neutrino scatters elastically off the nucleon ejecting a nucleon from the target; at few GeV the neutrino can excite the target nucleon to a resonance state and this *resonance production* (RES) cross-section overcomes the QE one; finally, above 100 GeV, where the neutrino energy is much larger than the nucleon mass, the neutrino scatters off a quark of the nucleon producing a hadronic system in the final state: this process is called the *deep-inelastic* scattering (DIS) and at these energies becomes the most significant one. Let us consider the DIS interactions, represented in the diagram of Fig. 1.2:

$$\nu_\ell + N \rightarrow \ell^- + X \quad (CC) \quad (1.3a)$$

$$\bar{\nu}_\ell + N \rightarrow \ell^+ + X \quad (CC) \quad (1.3b)$$

$$\nu_\ell + N \rightarrow \nu_\ell + X \quad (NC) \quad (1.4)$$

where $N = p, n$ and X denotes any set of final hadrons.

The scattering can occur either with the exchange of a charged W^\pm boson (Eqs. 1.3a,1.3b) or of a neutral Z^0 boson (Eq. 1.4): these are respectively referred to as Charged Current (CC) and Neutral Current (NC) interactions.

Let us now introduce some denomination: in the following, we denote with E_ν, E_ℓ the neutrino and lepton energy and p_ν, p_ℓ, p_N, p_X respectively the four-momenta of to the

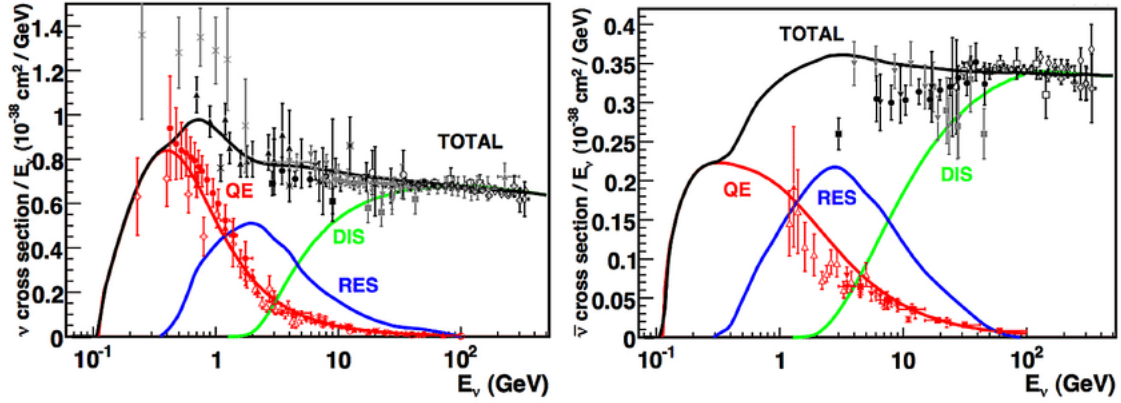


Figure 1.1: CC Neutrino-nucleon (**left**) and antineutrino-nucleon (**right**) cross-sections divided by neutrino energy, as a function of energy. The plot shows the total cross-sections (black lines) and the various contributing processes: quasi-elastic scattering (QE, red line), resonance production (RES, blue line), deep-inelastic scattering (DIS, green line). For prediction evaluation and plotted data refer to [53], whence the picture is taken.

neutrino, of the charged lepton, of the target nucleon and the sum of four-momenta of final hadrons. Considering the kinematics of the process, the transferred four-momentum is defined as:

$$q \equiv p_\nu - p_\ell = p_X - p_N = (q_0, \mathbf{q}) \quad (1.5)$$

and the Lorentz-invariant squared center-of-mass energy is:

$$s = (p_\nu + p_N)^2 \quad (1.6)$$

Other relevant Lorentz-invariant quantities are:

$$Q^2 \equiv -q^2 = 2p_\nu \cdot p_\ell \quad (1.7a)$$

$$x \equiv \frac{Q^2}{2p_N \cdot q} \quad (1.7b)$$

$$y = \frac{p_N \cdot q}{p_N \cdot p_\nu} \quad (1.7c)$$

where x and y are the *Bjorken scaling variable* and *inelasticity* (or *Bjorken y*). Note also that the inelasticity variable in the laboratory frame, assuming $E_\nu \gg m_N$, becomes:

$$y = \frac{q_0}{E_\nu} = \frac{E_\nu - E_\ell}{E_\nu} \quad (1.8)$$

where its physical meaning is immediate: y is the fraction of energy transferred from the neutrino to the nucleon.

The variables in Eqs. 1.7a-1.7c are moreover related by:

$$xy = \frac{Q^2}{s - m_N^2} \quad (1.9)$$

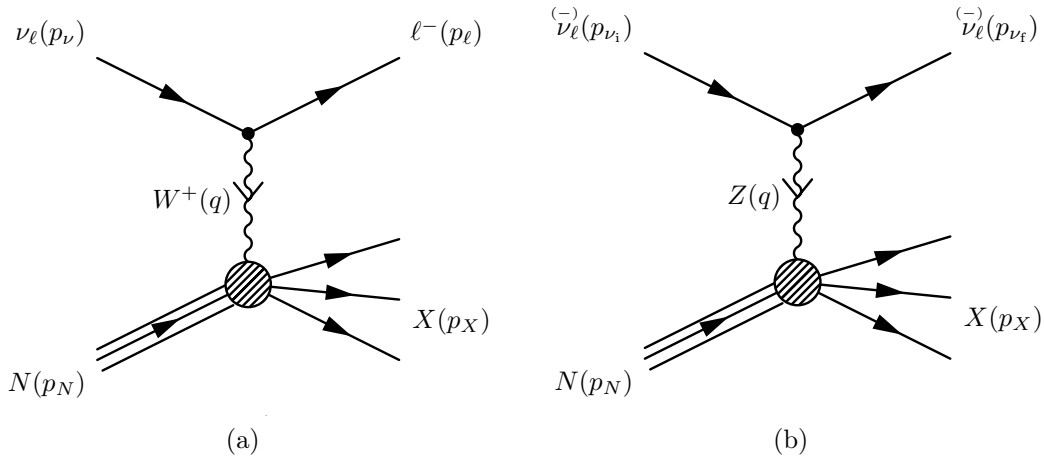


Figure 1.2: Diagrams of the neutrino-nucleon DIS processes: CC interaction (**left**) with the exchange of a W -boson and NC interaction (**right**) with the exchange of a Z -boson. Four-momenta are also shown. Picture taken from [60].

One can show (see [43],[82]) that the differential cross section can be described in terms of three of these kinematic variables, for example:

$$\frac{d^2\sigma_{CC}^{\nu,\bar{\nu}}}{dxdy} = \frac{\sigma_{CC}^0}{2} \left[(F_2(x) \mp xF_3(x))(1-y)^2 + (F_2(x) \pm xF_3(x)) \right] \quad (1.10)$$

with

$$\sigma_{CC}^0 = \frac{G_F^2 m_N E_\nu}{\pi} \left(\frac{m_W^2}{Q^2 + m_W^2} \right)^2 \quad (1.11)$$

where m_W is the W boson mass and $F_i(x)$ the *Bjorken structure functions*. These are real functions of q_0 and Q^2 , but in the high-energy limit they depend only on the dimensionless ratio x . The relation Eq. 1.10 takes more meaning within the grounds of the *quark-parton model* of hadrons, on which is based the current interpretation of the DIS processes [60]. In this framework Eq. 1.10 turns into:

$$\frac{d^2\sigma_{CC}^{\nu}}{dxdy} = 2\sigma_{CC}^0 \left[(xq(x) + x\bar{q}(x))(1-y)^2 \right] \quad (1.12a)$$

$$\frac{d^2\sigma_{CC}^{\bar{\nu}}}{dxdy} = 2\sigma_{CC}^0 \left[(xq(x)(1-y)^2 + x\bar{q}(x)) \right] \quad (1.12b)$$

where $q(x), \bar{q}(x)$ are the quark and antiquark density distribution inside the nucleon. Integrating Eqs. 1.12a and 1.12b as in [43] one obtains the total interaction cross sections. In particular, assuming a small transferred four-momentum compared to the W -boson's mass, in the laboratory frame we have

$$\sigma_{CC}^0 \simeq \frac{G_F^2}{\pi} m_N E_\nu \simeq 1.58 \times 10^{-38} \left(\frac{E_\nu}{\text{GeV}} \right) \text{cm}^2 \quad (1.13)$$

which only depends linearly on the neutrino energy E_ν .

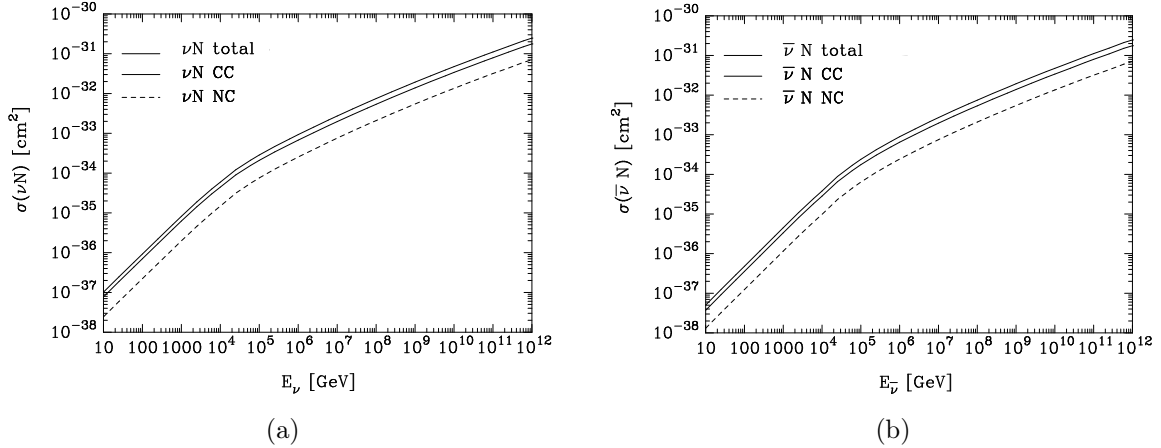


Figure 1.3: Neutrino-nucleon (**left**) and antineutrino-nucleon (**right**) CC, NC and total cross-sections as a function of neutrino energy, in the high-energy range. One can notice the linear dependence on the neutrino energy, and the difference between CC and NC cross-sections. For the parton distribution used in the calculations refer to [58], whence the picture has been taken.

Moreover one finds the important result that $\sigma_{CC}^\nu/\sigma_{CC}^{\bar{\nu}} \simeq 2$, i. e. the probability for a high-energy antineutrino of interacting with matter is half the probability for a neutrino. For larger transferred four-momentum cross-sections must take into account also the vector boson mass: for details of calculations with different parton distributions see [58].

The same calculations which hold for CC interactions hold also for NC interactions, with the obvious substitution of the W -boson with the Z -boson. Hence,

$$\frac{d^2\sigma_{CC}^{\nu,\bar{\nu}}}{dx dy} = \frac{\sigma_{CC}^0}{2} \left[(F_2(x) \mp xF_3(x))(1-y)^2 + (F_2(x) \pm xF_3(x)) \right] \quad (1.14)$$

with

$$\sigma_{CC}^0 = \frac{G_F^2 m_N E_\nu}{\pi} \left(\frac{m_Z^2}{Q^2 + m_Z^2} \right)^2 \quad (1.15)$$

The total cross-section of NC interaction is smaller than the CC one, and one obtains a ratio:

$$\frac{\sigma_{CC}^{\nu/\bar{\nu}}}{\sigma_{CC}^{\nu/\bar{\nu}} + \sigma_{NC}^{\nu/\bar{\nu}}} \approx 0.7 \quad (1.16)$$

meaning that about the 70% of all neutrino-nucleon DIS scattering are charged current ones. Total cross sections of CC and NC interactions for the neutrino and the antineutrino are shown in Fig. 1.3.

Neutrino-electron interaction

Beside the charged and neutral current DIS with nucleons, another kind of interaction takes relevance for high-energy neutrinos: the interaction with electrons mediated by the W and Z bosons. The neutrino-electron cross section is in most cases smaller than

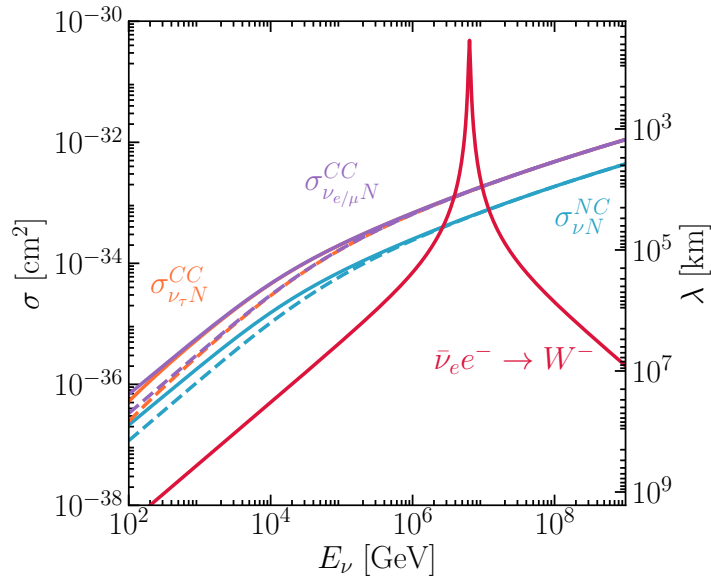


Figure 1.4: Neutrino scattering cross sections for different processes as a function of energy. The blue curves indicate neutral-current DIS processes for all neutrino flavors, while the purple and orange curves indicate the charged-current DIS processes for ν_e/ν_μ and ν_τ respectively. Solid curves refer to neutrinos and dashed ones to antineutrinos. The red curve instead refers to the Glashow resonance. The y-axis on the right represents the water equivalent mean free path of these interactions. Picture taken from [68].

the neutrino-nucleon one by orders of magnitude. However, for the scattering of the $\bar{\nu}_e$ with electrons the cross section of the interaction sharply increases as the center-of-mass energy approaches the W -boson mass, and at the resonant on-shell production of the W the cross section for the process $\bar{\nu}_e + e^- \rightarrow W^-$ reaches a maximum of $\sigma_{\bar{\nu}_e e^-}^{GR} \simeq 4.86 \times 10^{-31} \text{ cm}^2$ when the antineutrino energy is $E_{\bar{\nu}_e} \simeq 6.3 \text{ PeV}$, as shown in Fig. 1.4. This process was put forward in 1959 by S. L. Glashow and it is known as the *Glashow resonance* [61]; due to the difficulties of detecting neutrinos of such high energies, it remained unobserved until very recently. In fact, in 2020 the IceCube collaboration reported the detection by the IceCube observatory of a cascade of high-energy particles consistent with being created at the Glashow resonance [20]. The measured shower energy was $6.05 \pm 0.72 \text{ PeV}$ and the inferred neutrino energy, taking into account the non-visible part of the shower, was about 6.3 PeV. Given its energy and direction, it is classified as an astrophysical neutrino at the 5σ level. Furthermore, other features of the event, as well as the measured energy, are consistent with the hadronic decay of a W^- boson produced on the Glashow resonance.

1.1.2 Neutrino oscillation

The term *oscillation* or *mixing* related to neutrinos is referred to the phenomenon of flavor changing of neutrinos while they propagate in vacuum or in a medium. This feature is based on the non-coincidence between neutrino flavor eigenstates and mass eigenstates. Indeed, if neutrinos are massive their flavor eigenstates ν_e, ν_μ, ν_τ are mixture of at least three different mass eigenstates ν_1, ν_2, ν_3 , exactly as it happens to quarks in the Standard

Model. The hypothesis of neutrino mixing was first anticipated by Bruno Pontecorvo in 1957 [83] and took further by Maki, Nakagawa and Sakata [73] on the basis of a two-neutrino hypothesis. Later on, the theory was generalized to three neutrino families and after the first evidences in the '70s of neutrino oscillations in solar neutrinos, finally in 2002 the definitive proof came with the Sudbury Neutrino Observatory (SNO) [30]. It is important to underline the fact that in order to contemplate neutrino oscillations, the massive nature of neutrinos must be postulated, and a neutrino mass term must be then introduced in the Standard Model lagrangian. Let us now briefly take a look at the oscillation formalism.

Three-neutrino families formalism

The presence of a mass term for neutrinos in the Standard Model lagrangian, as is the case for quarks, implies the possibility of transitions between different neutrino flavors, violating the conservation of the flavor lepton numbers L_e, L_μ, L_τ . Neutrino flavor eigenstates $|\nu_\alpha\rangle$ ($\alpha = e, \mu, \tau$) are then different from mass eigenstates $|\nu_i\rangle$ ($i = 1, 2, 3$) and they can be written in terms of them as:

$$|\nu_\alpha\rangle = \sum_i U_{\alpha i}^* |\nu_i\rangle, \quad |\nu_i\rangle = \sum_\alpha U_{\alpha i} |\nu_\alpha\rangle \quad (1.17)$$

and it holds:

$$\langle \nu_i | \nu_j \rangle = \delta_{ij} \quad (1.18)$$

where $U_{\alpha i}$ is the unitary 3×3 Pontecorvo-Maki-Nakagawa-Sakata (PMNS) mixing matrix:

$$U = \begin{pmatrix} U_{e1} & U_{e2} & U_{e3} \\ U_{\mu1} & U_{\mu2} & U_{\mu3} \\ U_{\tau1} & U_{\tau2} & U_{\tau3} \end{pmatrix} \quad (1.19)$$

The PMNS matrix can be parametrized by 3 mixing angles θ_{ij} and 1 complex CP-violating phase δ as follows:

$$U = \begin{pmatrix} 1 & 0 & 0 \\ 0 & c_{23} & s_{23} \\ 0 & -s_{23} & c_{23} \end{pmatrix} \begin{pmatrix} c_{13} & 0 & e^{i\delta} s_{13} \\ 0 & 1 & 0 \\ -e^{i\delta} s_{13} & 0 & c_{13} \end{pmatrix} \begin{pmatrix} c_{12} & s_{12} & 0 \\ -s_{12} & c_{12} & 0 \\ 0 & 0 & 1 \end{pmatrix} \quad (1.20)$$

where $c_{ij} = \cos \theta_{ij}$, $s_{ij} = \sin \theta_{ij}$. Consider now a neutrino mass eigenstate $|\nu_j\rangle$ with energy E (GeV). The propagation in time of mass eigenstate is described by the time-dependent Schrödinger equation, and since mass eigenstates are eigenstates of the Hamiltonian \mathcal{H} with eigenvalue E one has:

$$i \frac{\partial}{\partial t} |\nu_j(t)\rangle = \mathcal{H} |\nu_j(t)\rangle = E |\nu_j(t)\rangle \quad (1.21)$$

The stationary state solution of Eq. 1.21 is

$$|\nu_j(t)\rangle = e^{-iEt} |\nu_j(0)\rangle \quad (1.22)$$

which due to the low-mass approximation becomes:

$$|\nu_j(t)\rangle = e^{-ipt - im_j^2 L/2E} |\nu_j\rangle \quad (1.23)$$

where $L = t$ in natural units and $|\nu_j(0)\rangle = |\nu_j\rangle$. Then, considering relationships in Eq. 1.17, the amplitude for the transition from a flavor state α to a flavor state β after a time t is:

$$\langle \nu_\beta | \nu_\alpha(t) \rangle = e^{-ipt} \sum_{j=1}^3 U_{\beta j}^* U_{\alpha j} e^{-im_j^2 L/2E} \quad (1.24)$$

Hence, the probability of a neutrino produced with flavor α and energy E of being detected at a distance L with a flavor β is simply:

$$P_{\nu_\alpha \rightarrow \nu_\beta}(L, E) = |\langle \nu_\beta | \nu_\alpha(t) \rangle|^2 = \sum_{i,j} U_{\beta i}^* U_{\alpha i} U_{\beta j} U_{\alpha j}^* \exp\left(i \frac{\Delta m_{ij}^2 L}{2E}\right) \quad (1.25)$$

which can be rewritten also as:

$$\begin{aligned} P_{\nu_\alpha \rightarrow \nu_\beta}(L, E) &= \sum_{j=1}^3 |U_{\beta j}|^2 |U_{\alpha j}|^2 \\ &+ 2 \sum_{i>j} \Re(U_{\beta j}^* U_{\alpha j} U_{\beta i} U_{\alpha i}^*) \cos\left(\frac{\Delta m_{ij}^2 L}{2E}\right) \\ &+ 2 \sum_{i>j} \Im(U_{\beta j}^* U_{\alpha j} U_{\beta i} U_{\alpha i}^*) \sin\left(\frac{\Delta m_{ij}^2 L}{2E}\right) \end{aligned} \quad (1.26)$$

Eq. 1.25 can be seen as separated in two terms: the amplitude of the oscillation is determined by the elements of the mixing matrix, i. e. by the parameters θ_{ij} and δ , while the phase of the oscillation depends on the ratio L/E and on the difference of the squared masses $\Delta^2 m_{ij} = m_i^2 - m_j^2$, which clearly is different from zero only if neutrino masses are different from zero. Note also that the exponential term does not depend on the absolute values of the masses but only on the differences, and since $\Delta m_{31}^2 = \Delta m_{32}^2 + \Delta m_{21}^2$ there are only two independent Δm_{ij}^2 if there are only three neutrino flavors. The determinations of the absolute values of neutrino masses and of their hierarchy are still open problems.

Let us consider now the effect of the oscillation on the flavor content of high-energy neutrinos produced in astrophysical events. These neutrinos travel undisturbed over very long baselines of the order of the Kpc-Gpc, in a medium which substantially is the vacuum. In that case, we can take the limit $L \rightarrow \infty$ in Eq. 1.26 and the probability of mixing becomes:

$$P_{\nu_\alpha \rightarrow \nu_\beta}(L \rightarrow \infty) = \sum_{i=1}^3 |U_{\beta i}|^2 |U_{\alpha i}|^2 \quad (1.27)$$

because both the sine and the cosine which make up the exponential in Eq. 1.26 vanish as a result of averaging over the rapid oscillations for $L/E \rightarrow \infty$. These probabilities can be evaluated inserting the measured values of the mixing parameters, as in [56]. For our purposes we consider only the ‘‘standard’’ scenario in which the most general initial

flux composition of high-energy neutrinos at the sources can be written approximately as $\Phi^0(\nu_e) : \Phi^0(\nu_\mu) : \Phi^0(\nu_\tau) = 1 : 2 : 0$, where we assume that ν_τ production is extremely unlikely and the number of ν_μ doubles the one of ν_e , supposing neutrinos are produced mainly by pion decay chains $\pi^+ \rightarrow \mu^+ \nu_\mu \rightarrow \bar{\nu}_\mu e^+ \nu_e \nu_\mu$ (and equivalently for the π^-). After the oscillations during propagation, the expected detected flux on the Earth is obtained exploiting Eq. 1.27 and it is about $\Phi^0(\nu_e) : \Phi^0(\nu_\mu) : \Phi^0(\nu_\tau) = 1 : 1 : 1$, i.e. an approximately equal neutrino flux for each different flavor is expected on Earth.

1.2 Cosmic Rays

On Earth, we are continuously bombarded by an isotropic flux of high-energy charged particles coming from the sky. This has been known since the beginning of the last century, when Victor Hess conducted several balloon flights at different heights measuring the rate of ionization with an electroscope and discovered that ionization increased with height, leading him to the conclusion that the ionization was originated by radiation coming from space, which will be called in the following years *Cosmic Rays*. For this discovery he was awarded with the Nobel Prize in 1936. Since those first experiments, an enormous amount of effort, both theoretical and experimental, has been spent in the quest for the origin of this radiation and for the investigation of its nature, producing giant leaps forwards in our knowledge of Cosmic Rays, but still leaving us with several unanswered questions.

Nowadays we know that Cosmic Rays are an isotropic flux of high-energy and stable particles originating and accelerated in astrophysical environments. They are classified as *primary* and *secondary* CRs. Primary cosmic rays are protons, fully ionized atomic nuclei and electrons. Part of this radiation can interact either in or near the acceleration regions or during its propagation producing high-energy charged or neutral secondary particles. Among them, γ -rays and neutrinos are stable and can arrive on Earth together with primary particles. Antiparticles, mainly positrons and antiprotons, are produced and are present in the cosmic radiation as well. Instead, secondary CRs are all particles produced far from the acceleration regions, in interactions occurring during the propagation of primary CRs in space or in the Earth's atmosphere. While primary CRs can be detected by detectors and telescopes in space orbiting the Earth, experiments on Earth can study the flux of arriving CRs only in an indirect way by measuring the secondary particles in the showers produced by the interactions of primary CRs in the atmosphere, and they must have a completely different concept with respect to direct CRs detection experiments.

1.2.1 Energy spectrum

Cosmic rays at energies larger than few GeV have an energy spectrum which follows a power law of the kind:

$$\Phi(E) = K E^{-\alpha} \frac{\text{particles}}{\text{cm}^2 \text{ s sr GeV}} \quad (1.28)$$

The lower limit on this energy spectrum is somewhat arbitrarily put to a few GeV due to Solar activity: the winds of ionized plasma emitted by the Sun hinder the propagation of low-energy cosmic rays which have to diffuse upstream against this outflow in order

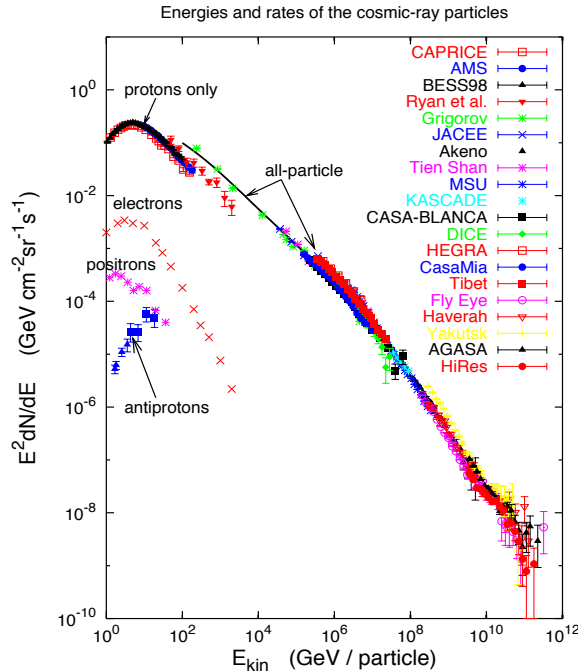


Figure 1.5: All-particle energy spectrum of cosmic rays. Data are taken from the labeled experiments, both of the direct and the indirect kind. Picture taken from [56].

to reach the inner heliosphere and the Earth. This process depends strongly on the Solar activity which is modulated according to 11-years and 22-years cycles [84]. The result is that the flux of low-energy cosmic rays is suppressed and the lowest-energy particles are prevented from reaching the inner solar system at all: the suppression is greater during the period of maximum solar activity in the 11-years cycle and less during the minimum activity. However, for energies high enough which are not influenced by this process, Eq. 1.28 holds and the energy range span over 12 orders of magnitude up to 10^{20} eV. The all-particle spectrum obtained with both measurements of direct and indirect experiments is shown in Fig. 1.5. By fitting the dataset with the proper function Eq. 1.28 we obtain the parameter α , called the *spectral index*, and the normalization factor K .

We immediately see from the figure that we can distinguish three different energy intervals: from 10^{10} eV up to 10^{15} eV the extrapolated spectral index is $\alpha \approx 2.7$. From 10^{16} eV to 10^{18} eV it is $\alpha \approx 3.1$. Then, above 10^{18} eV the spectrum flattens again with $\alpha \approx 2.6$ and finally it apparently cuts off at about 10^{20} eV. The transition region around 10^{15} eV is called the *knee*, whereas the one occurring around 10^{18} eV is the *ankle*. These three energy intervals reflect the nature of the different classes of astrophysical sources and accelerators which give rise to cosmic rays, as well as the differences in their composition and in their propagation throughout the Universe. We should now examine shortly these differences.

1.2.2 Cosmic rays below the *knee*

Cosmic rays in the energy range between 10^{10} eV – 10^{15} eV are the dominant part of the energy spectrum and their flux is high enough to be detected directly with balloon

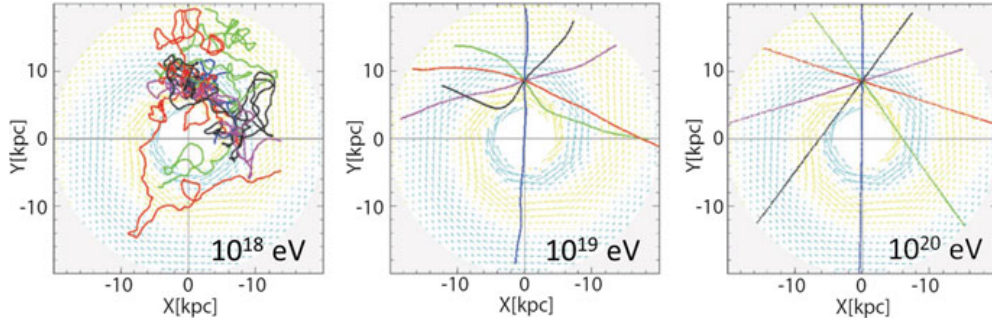


Figure 1.6: Simulated trajectory of charged CRs in the Galactic magnetic field. Particles of energy up to 10^{18} eV are bent by the magnetic field and undergo a chaotic motion inside the Galactic volume, whereas particles of energy of 10^{19} eV are only feebly deflected. Finally, particles with energy of at least 10^{20} eV travel along almost straight lines, allowing the direct identification of their sources. Picture taken from [91].

or satellite experiments. Their chemical composition has been measured with the abundance of nuclei detected by space-born experiments [42] and most estimations agree on a composition dominated mainly by protons ($\sim 85\%$) and Helium nuclei ($\sim 13\%$) followed by heavy nuclei ($\sim 1\%$), electrons ($\sim 1\%$) and antiparticles (less than 1%). The chemical composition of CRs of higher energy is still largely uncertain due to the difficulties in determining the atomic number of the primary cosmic ray from the measurement, made by indirect cosmic ray detection experiments, of the secondary particles produced in the shower they develop in the atmosphere (see Sec. 1.2.5).

Cosmic rays below 10^{18} eV are considered of Galactic origin, because we observe a uniform flux along the Galactic plane. As a matter of fact, the presence of the Galactic magnetic field of mean value $\langle B \rangle \simeq 4 \mu\text{G}$ continuously deflects the charged particles making them diffusing inside the Galactic volume in a chaotic motion, until they reach the boundaries of the Galaxy and escape away. A simulation of this motion in the Galaxy is shown in Fig. 1.6. Hence, such particles are strongly constrained inside the Galactic volume by the Galactic magnetic field and reach us isotropically from the Galactic plane, a completely different situation with respect to cosmic rays of energy higher than 10^{19} eV as we will see in Sec. 1.2.5.

We need now to do a crucial consideration: as the Larmor radius for a relativistic particle with charge Ze , energy E , in a magnetic field B is $R = \frac{E}{ZeB}$, it is then expected that the more energetic the particle is, the less curved its trajectory will be i. e. the less time it will spend diffusing inside the Galactic volume and the earlier it will escape from it. The complete treatment of this argument within the framework of the so-called *Leaky Box model* introduces an energy dependent exponentially decreasing term which must be convoluted with the emission spectrum at the astrophysical source to obtain the observed primary energy spectrum on Earth. This means that:

$$\Phi(E)|_{\text{observed}} \propto \Phi(E)|_{\text{source}} \cdot E^{-\delta} \quad (1.29)$$

Reverting Eq. 1.29 one has:

$$\Phi(E)|_{\text{source}} \propto \Phi(E)|_{\text{observed}} \cdot E^{\delta} \sim E^{-\alpha+\delta} \quad (1.30)$$

The value of the parameter δ can be obtained from measurements of the relative abundance of Light elements with respect to Carbon. Considering the Boron-to-Carbon ratio, a value of $\delta \simeq 0.6$ was derived with a *leaky box* model applied to measurements of the TRACER detector and other experiments [76]. Thus, as $\alpha \approx 2.7$ below the knee, using this value of δ we get the important prediction for the energy spectrum of CRs at the sources:

$$\Phi(E)|_{source} \propto E^{-2.1} \quad (1.31)$$

Models of CR sources below the knee should therefore reproduce this energy dependence, with a spectral index ~ 2 .

The Standard Model of CR production foresees that cosmic rays in this range of energy are accelerated in recursive stochastic mechanisms occurring in violent astrophysical processes that produce shock waves. In this mechanism, theorized for the first time by Enrico Fermi and hence called the *Fermi mechanism*, low-energy particles gain energy after a large number of interactions with a shock wave and reach energies as large as few 10^{14} eV.

The second-order Fermi acceleration mechanism

The idea of a recursive stochastic particle acceleration was developed in 1949 by Fermi [52]. The idea of Fermi was based on the fact that the interstellar medium is filled with clouds of ionized gas in movement with respect to an observer in the “Galaxy rest frame”. These clouds transport turbulent magnetic fields and can in principle reflect the incoming charged particles via magnetic scattering interactions. Let us consider the following simplified situation. An observer in the “Galaxy rest frame” S observes a perfect reflection of a particle with velocity v against a cloud of velocity V moving in the opposite direction: in the cloud rest frame S' , the particle is approaching with velocity $v + V$ and after the reflection, assuming a perfectly elastic shock since no interactions among particles are present, the particle has bounced back with the same but reversed velocity. Back to the S frame, the particle now moves in the same direction of the cloud, with velocity $v + 2V$, hence it has been accelerated. If instead in S the cloud is moving in the same direction of the particle, after the shock by the same reasoning the particle will be decelerated to $v - 2V$. This is the basic idea behind the Fermi mechanism: particles will be accelerated by encounters with magnetic clouds coming towards them and decelerated by encounters with magnetic clouds going away from them, and the energy gain/loss for each encounter can be calculated via a double change of reference frame. In this section and in the following Sec. 1.2.2 the approach in [92],[56] will be followed.

The next step is the assumption that the magnetic field is turbulent so that the charged particle is not perfectly reflected anymore, but it is instead isotropized inside the cloud so that the outgoing angle from the cloud θ'_{out} is random, as depicted in Fig. 1.7. To simplify the derivation we assume also that the particle is ultra-relativistic, i. e. $E \simeq pc$. From Lorentz transformations we have:

$$\begin{cases} E'_{in} = \gamma(E_{in} - p_{x,in} \cdot V) \simeq \gamma E_{in}(1 - \beta \cos \theta_{in}) \\ p'_{x,in} = \gamma(p_{x,in} - \frac{V}{c^2} E_{in}) \end{cases} \quad (1.32)$$

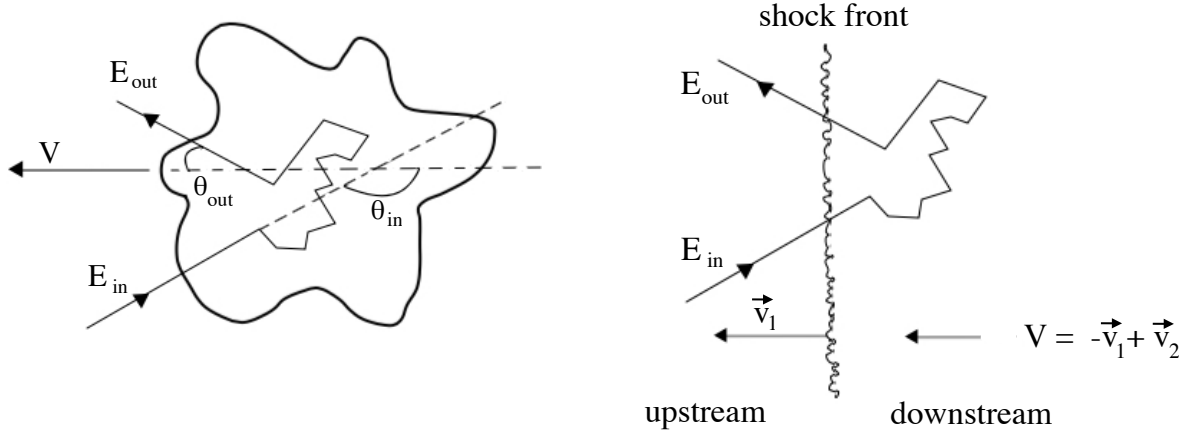
(a) *Second-order Fermi acceleration mechanism.*(b) *First-order Fermi acceleration mechanism.*

Figure 1.7: In the mechanism on the left-hand side of the figure the acceleration by a moving, partially ionized gas cloud is shown. On the right-hand side instead, the acceleration occurs at a plane shock front: the particle direction is isotropized by the magnetic turbulence both downstream and upstream. Thus, it can eventually cross back the shock from upstream to downstream and start another acceleration cycle.

where $\gamma = 1/\sqrt{1-\beta^2}$ and $\beta = V/c$. The subscript *in* and *out* refers to properties of the incoming and outgoing particle respectively, and the apex “'” to the cloud frame S' .

In the S frame with the inverse Lorentz transformation we have

$$E_{out} = \gamma(E'_{out} + p'_{x,out} \cdot V) \simeq \gamma E'_{out}(1 + \beta \cos \theta'_{out}) \quad (1.33)$$

Since the shock is elastic, we have $E'_{out} = E'_{in}$ and combining Eq. 1.32 with Eq. 1.33 we obtain:

$$E_{out} = \gamma^2 E_{in}(1 - \beta \cos \theta_{in})(1 + \beta \cos \theta'_{out}) \quad (1.34)$$

which implies an energy gain of

$$\frac{\Delta E}{E} = \frac{E_{out} - E_{in}}{E_{in}} = \frac{\beta^2 - \beta \cos \theta_{in} + \beta \cos \theta'_{out} - \beta^2 \cos \theta_{in} \cos \theta'_{out}}{1 - \beta^2} \quad (1.35)$$

To get the average energy gain, we need to average the above expression. By hypothesis, the particle is isotropized in the cloud, hence $\langle \cos \theta'_{out} \rangle = 0$. On the other hand, the probability to have an encounter with an incidence angle θ_{in} is proportional to the relative velocity between the particle and the cloud and $\langle \cos \theta_{in} \rangle \simeq -\frac{\beta}{3}$. Substituting in Eq. 1.35 one finally gets:

$$\langle \Delta E \rangle \simeq \frac{4}{3} \beta^2 \langle E \rangle \equiv \xi \langle E \rangle \quad (1.36)$$

The proportionality with β^2 is the reason why this model is called the *second-order* Fermi mechanism. Note that the fractional energy gain in the process of stochastic acceleration

is constant. Hence, after n encounters of magnetic clouds with same β the particle energy will be:

$$E_n = E_0(1 + \xi)^n \quad (1.37)$$

From Eq. 1.37, the number of encounters needed to reach energy E_n is:

$$n = \ln\left(\frac{E_n}{E_0}\right) / \ln(1 + \xi) \quad (1.38)$$

At every encounter the particle has a probability P_{esc} of escaping the region occupied by the magnetic clouds and of stopping from being accelerated. The probability of remaining in the cloud region long enough to have n encounters is therefore $(1 - P_{esc})^n$. Thus, starting with a number N_0 of particles, the number of particles accelerated to energies greater than E_n is given by summing all encounters with $m \geq n$:

$$N(\geq E_n) = \sum_{m=n}^{\infty} (1 - P_{esc})^m = N_0 \frac{(1 - P_{esc})^n}{P_{esc}} \quad (1.39)$$

Substitution of Eq. 1.38 into Eq. 1.39 leads to:

$$N(\geq E_n) = \frac{N_0}{P_{esc}} \left(\frac{E_n}{E_0}\right)^{-\gamma} \quad (1.40)$$

with

$$\gamma = \ln\left(\frac{1}{1 - P_{esc}}\right) / \ln(1 + \xi) \approx \frac{P_{esc}}{\xi} \quad (1.41)$$

The last approximation is justified by the fact that the $\beta \ll c$ which implies $P_{esc} \ll 1$ and $\xi \ll 1$. Stochastic acceleration thus generates power law energy spectra, and in this mechanism the power law index depends on β^2 . The energy gain per unit time depends on the frequency of encounters ν_{enc} and it is:

$$\frac{dE}{dt} = \nu_{enc} \Delta E = \frac{c}{\lambda_{enc}} \xi E = \frac{\xi E}{T_{enc}} \quad (1.42)$$

where λ_{enc} is the mean free path between two consecutive encounters and T_{enc} is the related characteristic time. The acceleration time is thus proportional to the energy and reaching higher energy requires respectively longer time. Fermi soon realized that this mechanism does not work because it is not enough efficient and the acceleration is too slow. Indeed, β^2 is of the order of 10^{-7} or less and λ_{enc} is not shorter than 1 pc. It follows that a sizeable energy increase of a CR particle could be achieved only on very large timescales, too large to explain the very high energies observed for CRs. We need to find a more efficient acceleration mechanism.

The first-order Fermi acceleration mechanism

The problem of the first-order Fermi mechanism is that the energy gain is proportional to β^2 . If we had considered only head-on collisions, the energy gain would have been instead proportional to β , and a mechanism which would provide only head-on collisions between particles and would be much more likely to be a good candidate mechanism

for cosmic-ray acceleration. This is exactly what happens with “astrophysical shocks”, in the so-called *Diffusive Shock Acceleration* mechanism (DSA). In particular, during supernova explosions (see Sec.1.2.3) a shock wave is formed ahead of the expanding supernova remnant because the velocity of the remnant is much higher than the sound velocity of the interstellar medium. When a shock wave propagates through a medium, two distinct region can be defined: the *downstream* region which is the one that have already been shocked and the *upstream* region, which is the region of space ahead of the shock that has not been shocked yet. This situation is depicted in Fig.1.7, where a configuration with a large, plane, non-relativistic shock is considered. The velocities in the two regions are related by the requirement for continuous mass flow through the shock $v_1\rho_1 = v_2\rho_2$, that is $v_2 = v_1/r$ where $r \equiv \rho_2/\rho_1$ is the *compression ratio* between the densities of the two media. In the shock frame, the upstream medium is coming toward the shock with a velocity v_1 (note of course that $v_1 = v_{sh}$ where $v_{sh} \ll c$ is the shock wave velocity). Passing through the shock wave the gas slows down and the downstream medium is moving away from the shock with a velocity $v_2 = v_1/r = v_{sh}/r$. Let us now consider an observer at rest in the upstream frame. He sees the shock approaching with a velocity $v_1 = v_{sh}$ and he also sees the downstream medium approaching with a velocity $\Delta v = v_1 - v_2 = (\frac{r-1}{r})v_{sh}$. Now for an observer at rest with respect to the downstream fluid, the shock is going away with the velocity v_2 we obtained before, but the upstream medium is coming toward the observer, again with a velocity $\Delta v = v_1 - v_2 = (\frac{r-1}{r})v_{sh}$. Let us assume that both the upstream and downstream media are magnetized. We are then in a situation where a particle coming from the upstream medium and passing through the shock would see the downstream medium as a “magnetic cloud” coming towards it with a velocity Δv with respect to it. Likewise, a particle coming from the downstream medium and passing through the shock would see the upstream medium as a “magnetic cloud” coming towards it with a velocity Δv with respect to it. Both downstream and upstream the particle is isotropized in collision-less scattering interactions by the magnetic turbulence and can be reflected back and cross the shock wave again and again. The critical difference with the original mechanism proposed by Fermi is that in this configuration all the elastic collisions are now head-on in the corresponding frame and a particle which crosses several times the shock always gain energy at each encounter. The acceleration process continues until the particle diffuses or is convected away from the shock.

To calculate the average energy gain for this process we can make use of Eqs. 1.32,1.33 where now unprimed quantities refer to the upstream frame and primed quantities to the downstream frame. Let θ_{in} be the the angle between the particle velocity and the shock normal vector at the initial shock crossing in the upstream frame and θ_{out} the angle of the particle with the shock normal when crossing the shock back to the upstream medium. Moreover, in this case we have $\beta = \Delta v/c$, i. e. the relative velocity of the plasma flow, and $\gamma = \frac{1}{\sqrt{1-\frac{\Delta v^2}{c^2}}}$. Assuming elastic scatterings ($E'_{in} = E'_{out}$) we obtain again the expression Eq. 1.35. Averaging the two angles one finds $\langle \cos \theta_{in} \rangle = -\frac{2}{3}$ and $\langle \cos \theta'_{out} \rangle = \frac{2}{3}$. Since $v_{sh} \ll c$ we also have $\Delta v \ll c$ and we can neglect terms in β^2 in Eq. 1.35. We finally get:

$$\langle \Delta E \rangle \simeq \frac{4}{3}\beta \langle E \rangle \equiv \xi \langle E \rangle \quad (1.43)$$

From Eq.1.43 we understand also why this mechanism is also called *first-order Fermi*

mechanism. Shock acceleration is much faster than the original Fermi acceleration mechanism: not only the energy gain depends on β instead of β^2 , but also supernova shock velocity is much higher than the average velocity of molecular clouds. As a result shock acceleration is order of magnitudes more efficient, and correspondingly much faster.

Therefore, shock acceleration gives a definite prediction for the spectral index of the power law spectrum of accelerated particles. For the configuration of the large, plane shock, the rate of encounters is given by the projection of an isotropic CR flux of density ρ_{CR} onto the plane shock front, which gives $c\rho_{CR}/4$. The rate of escaping particles from the shock by downstream convection is instead the product of the same CR density times the convection density v_2 . The escape probability is then the ratio between the escape rate and the encounter rate:

$$P_{esc} = \frac{\rho_{CR}v_2}{c\rho_{CR}/4} = \frac{4v_2}{c} \quad (1.44)$$

and from Eq. 1.41 we obtain

$$\gamma \simeq \frac{P_{esc}}{\xi} = \frac{3}{v_1/v_2 - 1} \quad (1.45)$$

A shock can form when $v_1 > c_1$, the sound speed in the medium. The Mach number of the flow is defined as $M = v_1/c_1$. The continuity of the mass flow across the shock together with the kinetic theory of the gas gives:

$$r = \frac{v_1}{v_2} = \frac{\rho_2}{\rho_1} = \frac{(c_p/c_v + 1)M^2}{(c_p/c_v - 1)M^2 + 2} \quad (1.46)$$

For a monoatomic gas the ratio of specific heats is $c_p/c_v = 5/3$, so Eq. 1.45 becomes:

$$\gamma \approx 1 + \frac{3}{M^2} \sim 1 \quad (1.47)$$

for a strong shock with $M \gg 1$ i. e. with plasma flow velocity much higher than the sound of speed in the medium. For supernova blast shocks with matter flow velocity of the order of 10^9 cm/s and sound speed of the order 10^6 cm/s this condition is fulfilled during a large fraction of the supernova remnant evolution. Unlike the model for second-order Fermi acceleration, the spectral index here is independent of the absolute magnitude of the velocity of the plasma, but it depends only on the shock compression ratio. Not only is the spectral index for the first-order Fermi acceleration universal, but it has a numerical value close to what is needed to describe the observed cosmic ray spectrum up to the knee: from the integral spectral index Eq. 1.47 one derives the differential spectral index $\alpha \approx 2$, which is exactly what we expected (See Eq. 1.31).

Finally, we can derive the maximum energy that a charged particle can achieve in acceleration at the shock. From Eq. 1.42 and following simple arguments [91], one obtains:

$$E^{max} \simeq 300 \cdot Z \text{ TeV} \quad (1.48)$$

where typical values of the radius of supernova expansion, Galactic magnetic field and shock velocity have been used. Thus, this mechanism based on supernova explosions explains the spectrum of CRs up to the knee and it is important to notice that this maximum energy depends on the electric charge of the particle: in this way the knee

structure is explained as resulting from the different maximum energy reached by the different species of nuclei. For all of these reasons and for others, supernova remnants (SNR) are the most accredited sites for CRs acceleration below the knee.

1.2.3 Galactic accelerators

There is nowadays substantial consensus in the scientific community that Galactic CRs are somehow related to supernova explosions and that the acceleration process is mainly due to the DSA mechanism in the presence of the strong shocks formed as a consequence of these explosions, as described in the previous section. In particular, the main candidate are the Supernovae Type II. These occur at the end of the life of massive stars, when the core is completely fused to iron after the fusion cycle. At that point no further exothermal processes are possible and temperature and density in the core are so high that the electron capture in protons bound in iron nuclei is energetically favorable. This reaction reduces the electron pressure and produces neutron-rich nuclei in the core, a fraction of which undergoes β -decay emitting $\bar{\nu}_e$. The electron degeneracy pressure can no longer sustain the core and the star collapses. When the density reaches a value of $\rho \approx 10^{12} \text{ g/cm}^3$ neutrinos can no longer escape from the core and they are trapped inside the so-called *neutrinosphere*. The collapse continues until a value of $\rho \approx 10^{14} \text{ g/cm}^3$ is reached in the inner core: this corresponds to the nuclear density, and at this point the compressibility drops drastically. The core stops abruptly from collapsing and the infalling material bounces back onto it. This generates a shock wave propagating outwards, which triggers the supernova explosion. A fraction of neutrinos in the neutrinosphere leaves the star quickly after the shock wave, causing the *neutrino burst*. These neutrinos carry away energy and the shock is so weakened that it becomes stalled, while a compact remnant forms at the center of the collapsing star: it becomes a neutron star or a black hole depending on whether its progenitor star had a mass lower or larger than about 25 solar masses. The new-born neutron star still contains a large number of trapped neutrinos and inside it thermally generated electron-positron pairs transform into neutrino pairs of all flavours. The absorption of these neutrinos can revive the shock after the stalled phase: the density at its front decreases and becomes smaller than the trapping density, allowing neutrinos from the neutrinosphere to be released. These neutrinos carry almost the 99% of the total gravitational binding energy released from the supernova, which is about $3 \times 10^{53} \text{ erg}$, and only the 1% (of the order of 10^{51} erg) is split among photons and kinetic energy of the expanding material. However, even though only a small fraction goes into kinetic energy, this quantity is exactly what is needed to maintain steady the observed cosmic ray density. As a matter of fact, considering that on average we observe a supernova every 50 years and that only a small fraction (1-10%) of the kinetic energy of material ejected by the supernova goes to high energy particles, we obtain an average output power of emitted cosmic rays of the order of $P_{SN} \sim 10^{40} \text{ erg/s}$, which is equal to the power required to balance the energy loss rate due to the escape of CRs out of the Galaxy $P_{CR} \simeq 3 \times 10^{40} \text{ erg/s}$ in order to have a steady density. This energetic balance, together with the arguments exposed in the previous section, make these sites the most convincing Galactic cosmic ray accelerating sources.

1.2.4 Cosmic rays above the *knee*

In contrast to cosmic rays below the knee, there is no preferred acceleration model for cosmic rays in the energy range between 10^{16} eV and 10^{19} eV and several options are still under investigation. One possibility is that particles already accelerated by supernova remnants get re-accelerated by variable magnetic fields in the acceleration region. Variable magnetic fields, as a matter of fact, generate induced electric field, as described by Faraday's law:

$$\nabla \times \mathbf{E} = -\frac{\partial \mathbf{B}}{\partial t} \quad (1.49)$$

These electric fields induced by the magnetic fields of the remnant star or of more exotic binary systems, would accelerate CRs up to the highest energy before the ankle. One of the main candidates for this role is the *pulsar*, an extremely fast rotating neutron star which emits a beam of electromagnetic radiation along its magnetic axis. Its typical angular velocity can reach values of 12 500 rad/s and its magnetic field a value of $\sim 10^{12}$ G. Particles in the proximity of the pulsar can feel this rapidly varying magnetic field and be accelerated. The mechanism of this acceleration, which is not yet understood in detail [66], is rather complicate so that we will follow the simple dimensional argument in [91] to illustrate the basic idea. Firstly let us assume that the neutron star radius R_{NS} is the region over which the magnetic field varies. Then we can rewrite Eq. 1.49 as:

$$\frac{\mathcal{E}}{R_{NS}} = \frac{1}{c} \frac{dB}{dt} \quad (1.50)$$

where the electric field has been denoted as \mathcal{E} in order to avoid confusion, and the maximum energy gained from a particle over such a length becomes:

$$E^{max} = \int Ze\mathcal{E}dx = \int Ze\frac{R_{NS}}{c}\frac{dB}{dt}dx = ZeR_{NS}B\frac{\omega_{NS}R_{NS}}{c} \quad (1.51)$$

where ω_{NS} is the pulsar angular velocity. Inserting typical values for a pulsar one obtains a maximum value of $E^{max} \simeq 3 \times 10^{18}$ eV.

In some cases, after the supernova explosion and the formation of a pulsar at its center, a type of nebula powered by the pulsar winds of energetic particles emitted by the central pulsar can originate: these objects are called *Pulsar Wind Nebulae* (PWNe). During the transport of these winds, accelerated leptons can lose energy via interaction with the magnetic fields and emit synchrotron radiation from the radio band up to the MeV band. Also the Inverse Compton effect is present and very high energy γ -rays are observed. Even if there is yet no clear physical picture of the accelerating process in PWNe, nowadays we have several evidences that charged particles are accelerated in those regions at least up to 10^{15} eV. Whether the observed γ -rays come exclusively from accelerated leptons or also from hadrons has not yet been clarified (see Sec. 1.4), and the possibility of detecting high energy neutrinos generated in concomitance with the acceleration process of high energy hadrons will be tested with neutrino telescopes. Up to now though, no significant correlations between high energy neutrino detection and PWNe have been found [19].

Some binary systems are also possible candidate sites of CR acceleration. For this purpose binary systems consisting in a compact object such as a neutron star, a pulsar

or a black hole and a normal star are well-suited. In these systems enormous amounts of ionized matter fall from the “donor” component, which usually is the normal star, to the other component, the “accretor”. These motions create very strong electromagnetic fields in the proximity of the accretor, which can then accelerate charged particles to high energies. One relevant example is the *Microquasar*. Microquasars are Galactic X-ray binary systems in which the accretor is a low-mass black hole. The in-falling matter generates jets of relativistic charged particles observed in the radio band, whose underlying process is not yet understood and resembles the one occurring at larger scales in Active Galactic Nuclei (AGN). In few cases, there has been evidence of emission of high energy photons compatible with the acceleration of electrons with an energy of at least hundreds of TeV (as in [26]) and the observed presence of relativistic protons and iron nuclei in the jets [65] suggests that microquasars may produce a small but measurable contribution to the CR spectrum.

1.2.5 Ultra High Energy Cosmic Rays

Cosmic rays with energies above 10^{18} eV are referred to as *Ultra High Energy Cosmic Rays* (UHECRs). Their energies are so high that their Larmor radius is much larger than the thickness of the Galactic disk. Hence, if they came from some Galactic source, their arrival direction should correlate with the source location, since the trajectory follows an undeflected and almost straight line. This is clearly represented in Fig. 1.6. Since those anisotropies from the Galactic plane are not observed, whilst on the contrary there are some evidences from Telescope Array (TA) [70] and Pierre Auger Observatory (PAO) data [51] of large-scale anisotropies pointing away from the plane, we expect UHECRs to have most probably an extra-Galactic origin.

The candidate sources for UHECRs acceleration must of course provide enough energy for them to reach the largest observed energies i.e. 10^{20} eV and in addition the injection energy spectrum must fit, after considering the propagation effects, the observed UHECRs energy spectrum. Following the reasoning adopted in Sec. 1.2.4 and from Eq. 1.51, UHECRs must have necessarily (but not sufficiently) values of magnetic field and size such that they guarantee a value of $E^{max} \simeq 10^{20}$ eV. This requirement is called the *Hillas criterion* and the situation is represented in Fig. 1.8. The most prominent candidate sources which fulfill the requirement are *Gamma Ray Bursts* (GRB) and *Active Galactic Nuclei* (AGN).

Gamma ray bursts are very fast and intense bursts of γ -rays: they are the most energetic transient events in the Universe with an emission of up to 10^{53} erg in a time frame which goes from milliseconds to tens of seconds. Two different classes of GRBs can be identified: *short* bursts last less than 2 seconds, *long* ones more than 2 seconds. These different categories relate to different progenitor types: while long bursts are most probably connected to the collapse of massive stars into black holes, short ones are likely to be originated by the merger of two compact objects such as two neutron stars or a neutron star and a black hole. In 2017, for the first time, a gravitational wave signal compatible with the coalescence of two neutron stars was observed in concomitance with the observation of a GRB [24], confirming this type of objects as a progenitor of short GRBs.

Both types of emission are characterized by the so-called *afterglow*. Following the burst emission of γ -rays with energy distribution peaked at several hundreds of keV and

extending up to several GeV, a delayed emission of radiation at shorter wavelengths is observed. The first detection of the afterglow dates back to the 1997 when the Beppo-SAX satellite detected an emission of X-rays radiation several hours after the burst [48]. Later, a multi-wavelength campaign revealed also the emission of optical radiation [93]. Infrared and radio emission have been also detected in the afterglow, e. g. [41], and [86] for a review.

Independently of the nature of the progenitor, the *fireball model* is the most accredited model describing the process of the bursts. In this description, after either the collapse of the core of the massive star or the merger of the compact objects the consequent explosion causes the formation of two opposite jets along the rotation axis of the accretion disk with a relativistic expansion velocity ($\Gamma \simeq 10^2 - 10^3$), and inside these jets a plasma composed of photons, electrons, positrons and hadrons develops and get accelerated to relativistic velocities in shock fronts emerging in the outflows. Neutrino detection from GRBs would provide evidence that hadrons are indeed accelerated in the jets (see Sec. 1.4.2). Active

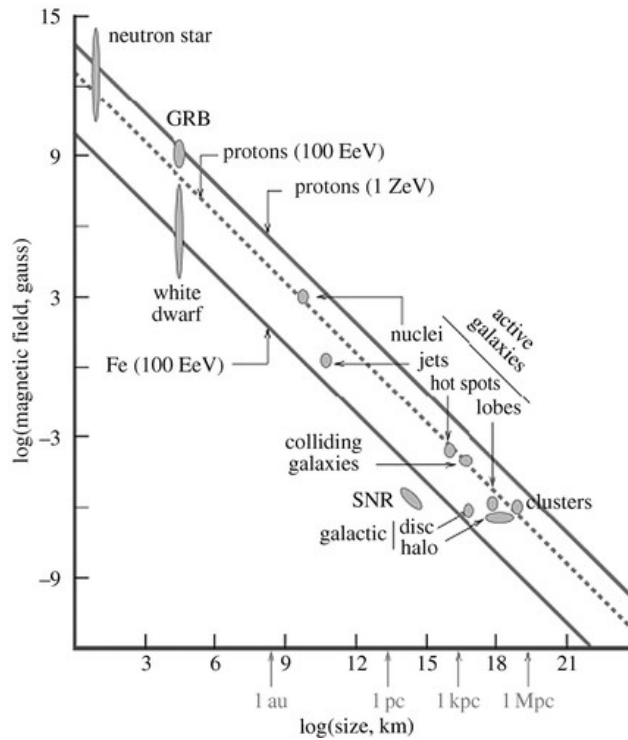


Figure 1.8: Hillas plot: sources above the top full (dashed) line are able to accelerate protons up to 10^{21} eV (10^{20} eV), while sources above the bottom full line are able to accelerate iron up to 10^{20} eV. Even if they are possible candidates in principle, neutron stars are discarded since we have no evidences of UHECRs emitted from Galactic neutron stars. Picture taken from [54].

Galactic Nuclei are galaxies with a central region characterized by a broad band emission (from radio to high-energy γ -rays) with strong time variability and extreme intensity, with powers that can reach even values of up to 10^{47} erg/s. The most widely used model foresees that jets comes out from a supermassive black hole (with a mass in the range of $10^6 - 10^9$ solar masses) in the core of the Galaxy, powered by the gravitational energy released by ionized matter falling from the toroidal accretion disk onto the black hole.

The complex interaction between the strong magnetic fields produced by the ionized matter and the matter in the accretion disk itself results in the formation of the ultra-relativistic jets in a way analogue to the one involved in microquasars (see Sec. 1.2.4). Historically AGN were classified by their emission spectra, but unified models exist which predict that different classes of AGN refer actually to the same object viewed at different angles [38], or which consider only two distinct classes (*radiative mode* and *jet mode*) [64]. No observations up to now have been able to settle which one among the many existing is the correct theoretical framework for jet formation, but anyway particles would be accelerated to high energies in those jets. The first observation in 2017 by the IceCube neutrino telescope of a high energy neutrino event coincident with multi-messenger observations of a particular type of AGN (a *blazar*) [17] has given confirmation that hadrons are accelerated in these astrophysical events (see Sec. 1.4.5).

At this point, however, we must take into account another important effect which arises when UHECRs propagate in the Universe. Soon after the discovery of the *Cosmic Microwave Background* (CMB) in 1966 [81] two papers came out in which G. Zatsepin with V. Kuzmin [98] and independently K. Greisen [62] proposed that UHECRs would have interacted with the recently discovered CMB photons and that this process would have cut off the cosmic ray spectrum making it end at an energy E_{GZK} just below 10^{20} eV. Hence, even if CRs of energy larger than the cut-off would have been produced, they would not have been able to survive their propagation from the sources to us. This limit has been called ever since the Greizen-Zatsepin-Kuzmin (GZK) cut-off. The involved processes are the pion productions through the Δ^+ resonance formation:

$$p + \gamma_{cmb} \rightarrow \Delta^+ \rightarrow \pi^+ + n \quad (1.52)$$

$$p + \gamma_{cmb} \rightarrow \Delta^+ \rightarrow \pi^0 + p \quad (1.53)$$

$$p + \gamma_{cmb} \rightarrow \Delta^+ \rightarrow p + \gamma \quad (1.54)$$

The neutral pion decays into two photons, while the neutron undergoes β -decay producing $p e^- \bar{\nu}_e$. Hence, in the final state we are left with a proton with an energy lower than the energy of initial proton: the global effect is that the flux of protons above threshold is reduced and high-energy photons and neutrinos are produced. The energy threshold for these processes can be derived via simple relativistic kinematics and one can show that the effect starts to become significant for proton energies larger than $E_p \simeq 5 \times 10^{19}$ eV. Also the *energy loss length* defined as $l^{-1} \equiv \frac{1}{E} \frac{dE}{dx}$ can be estimated [91] as

$$l_{p\gamma} \equiv \frac{1}{\langle y \sigma_{p\gamma} n_{\gamma_{cmb}} \rangle} \quad (1.55)$$

where y is the fraction of energy lost per interaction, $\sigma_{p\gamma}$ the cross-section of the proton interaction with photons at resonance energy ($\sim 250 \mu\text{b}$) and $n_{\gamma_{cmb}}$ the number density of CMB photons. Using approximated evaluations of these quantities one obtains a value of $l_{p\gamma} \simeq 30$ Mpc, which is small in terms of the distance of cosmological sources. This means that all protons originating in astrophysical events at distances larger than 30 Mpc arrive on Earth with a suppressed spectrum, i. e. with energies no larger than about 10^{20} Mpc. It is important to note that the reactions in Eqs. 1.52 to 1.54 happen

also to protons in heavy nuclei: for a heavy nucleus with atomic number A and energy E , those reactions occur to one of the nucleus protons, which have energy E/A each. The threshold energy for heavy nuclei therefore is higher by a factor A and the cut-off limit reaches a value of $E_{nuclei} \simeq E_{GZK} A$. It is crucial then to identify the composition of the observed UHECRs: depending on their atomic number, the cut-off in the observed spectrum would be shifted to higher or lower energies. HiRes experiment data [89] and data from the Pierre Auger Observatory and the Telescope Array experiment [50] are in agreement with a steepening of the energy spectrum above few 10^{19} eV, even if there are some differences that will require further studies on systematic uncertainties and improvements in the detections techniques in order to be settled. As we mentioned, this does not automatically prove that the cut-off is due to the GZK effect: in order to do so, the chemical composition of the spectrum must be studied. Unfortunately, inferring the chemical composition of CRs in air shower experiments such as those for UHECRs is extremely difficult since statistical shower-to-shower fluctuations prevent the individual measurement of the primary CR mass number, and up to now it has been only deduced on a statistical basis. HiRes [90] and TA [22] results agree on a lighter chemical composition of events at cut-off energies, whereas PAO data [67] seem to indicate that as the energy increases the composition of CRs tends to heavier nuclei. In order to address the problem, PAO has been recently upgraded [45] and in the next years the collaboration will be able to study the UHECRs composition with much lower uncertainties.

1.3 Atmospheric neutrinos

When a primary CRs such as a proton or a heavy nucleus enters the Earth's atmosphere, it interacts with the nuclei of the atmosphere via the following reaction:

$$p + N \rightarrow \pi^0, \pi^\pm, K^0, K^\pm, p, n, \dots \quad (1.56)$$

where N is a nucleon of the target nucleus and the ellipsis refer to higher mass mesons and baryons. In these interactions, many particles are created, which mostly are neutral and charged pions. These product particles in turn collide with other nuclei and generate a cascade with an electromagnetic component and a hadronic one. The process continues until the hadron energy falls below an interaction threshold. In particular, the π^0 has a lifetime of $\tau_{\pi^0} \simeq 8.4 \times 10^{-17}$ s and decays electromagnetically into two photons:

$$\pi^0 \rightarrow \gamma\gamma \quad (1.57)$$

whereas charged pions π^\pm decay through weak interactions:

$$\pi^+ \rightarrow \mu^+ \nu_\mu \quad (1.58a)$$

$$\pi^- \rightarrow \mu^- \bar{\nu}_\mu \quad (1.58b)$$

with a lifetime $\tau_{\pi^\pm} \simeq 2.6 \times 10^{-8}$ s. Then the muons subsequently decay with a lifetime $\tau_\mu \simeq 2.2 \times 10^{-6}$ s into:

$$\mu^+ \rightarrow e^+ \bar{\nu}_\mu \nu_e \quad (1.59a)$$

$$\mu^- \rightarrow e^- \nu_\mu \bar{\nu}_e \quad (1.59b)$$

Charged kaons K^\pm decay as in Eqs. 1.58a, 1.58b, but in the shower they are produced in a smaller fraction with respect to pions. The flux of neutrinos produced by the decay of pions and kaons is known as the *conventional neutrino flux*. In addition to that, charmed mesons produced in the CR interaction can produce a harder neutrino energy spectrum referred to as the *prompt neutrino flux*, expected to exceed the conventional one at energies above a hundred of TeV. The prompt component at lower energies instead is at present too low to be measured.

Hence, in the development of the cascade, neutrinos and muons are produced, and these are called respectively *atmospheric neutrinos* and *atmospheric muons*. They can penetrate up to several kilometers of water equivalent thanks to their small cross-sections or energy loss and long lifetime, and represent the most abundant shower component at sea level. In particular for our purposes, they play a key role in neutrino detectors, as the atmospheric muons represent the most abundant number of reconstructed events in the detector volume while atmospheric neutrinos constitute an irreducible background in experiments aimed at the detection of astrophysical neutrinos.

The conventional neutrino flux has been measured in the energy range above 100 GeV by neutrino telescope experiments like ANTARES [27] and IceCube [21], as well as in the lower energy range (from less than a GeV and up to few TeV) by experiments like Frejus and Super-Kamiokande [87]. A summary of atmospheric neutrino measurements can be found in [77]. At the same time, the conventional neutrino flux has been calculated by means of dedicated numerical simulations and MonteCarlo models such as FLUKA. The calculations rely on measurements of the energy spectrum and composition of cosmic rays and on models of the hadronic interactions producing the charged pions and kaons that decay into neutrinos. As a result, the flux can be expressed with a simple power-law spectrum:

$$\Phi_\nu(E) \propto E^{-\alpha-1} \quad (1.60)$$

where $\alpha \simeq 2.7$ is the spectral index for CRs below the knee. At high energies (i. e. above the TeV) the flux of ν_e is heavily suppressed so that only ν_μ contribution can be taken into account.

The above-mentioned measurements from experiments gave a conventional flux in agreement with the calculation in Eq. 1.60.

1.4 Astrophysical neutrinos and γ -rays

As we have seen in Sec. 1.2.2 the presence of the Galactic magnetic field deviates the trajectories of charged CRs coming from Galactic sources, making those sources impossible to be localized by usual astronomical methods. One way to get around this problem is to exploit neutral probes, that is γ -rays and neutrinos, produced in the interactions of primary CRs near the acceleration sources. These particles will propagate undeflected by magnetic fields and carry information about the precise location of the astrophysical object where they have been produced. On the one hand, due to their much larger cross-sections photons are much easier to detect than neutrinos. On the other hand, if

other objects (such as interstellar matter) are interposed along the photon path between the source and the Earth, or if the source is thick enough, photon interactions may suppress or greatly reduce the flux of photons reaching the detector. In this cases, neutrino extremely small cross-sections constitute an advantage since they will propagate undisturbed up to us. Moreover, as we will see, there are different mechanisms responsible for photon production, so that photon measurement can also give information on the nature of the underlying process happening at the source, allowing us to characterize it. Subsequent multi-wavelength observations would then help in discovering, classifying and studying the object.

1.4.1 γ -ray production mechanisms

Photons are produced in two different mechanisms. In the so-called *leptonic model* the processes that generate photons are the synchrotron radiation emission from relativistic electrons accelerated in the presence of magnetic fields in the surrounding of an astrophysical event and the mechanism of Inverse Compton scattering, in which ultra-relativistic electrons scatter on low-energy photons, accelerating them to high energies while the electrons slow down. Most probably the relevant role is played by the combination of the two in the so-called Self-Synchrotron Compton mechanism. Synchrotron radiation is made of photons of frequencies ranging from the Infrared to the X-rays, and these photons can in turn represent the target for the Inverse Compton scattering process by their own parent electron population. This way, the ultra-relativistic electrons accelerate those photons up to GeV or TeV energies, which is the region where the peak of the Inverse Compton energy distribution is located, depending on the initial electron energy distribution: this is the Self-Synchrotron Compton mechanism. Clearly the two involved processes are in this case strongly correlated, since an increment of the synchrotron emission implies an increment of the soft-photons population density for the Inverse Compton process.

Furthermore, high-energy photons can be produced as well by accelerated protons. This mechanism is referred to as the *hadronic model*. Those photons are mainly produced in the decays of neutral pions, as illustrated in Eq. 1.57, generated in the process similar to the one already seen in Eq. 1.56:

$$p + p \rightarrow \pi^0, \pi^\pm, K^0, K^\pm, p, n, \dots \quad (1.61)$$

with a cross-section of about 40 – 50 mb. In addition, neutral pions are generated also in the photoproduction process, where high-energy protons interact with low-energy photons in the surroundings of the source. This process is similar to the one in Eqs. 1.52, 1.53 occurring with CMB photons (see Sec. 1.2.5), yet in this case we are dealing not with CMB but instead with ambient photons, i.e. photons with frequencies spanning from the radio band to the UV band and populating the region around the astrophysical source. As discussed in the leptonic model, most of these are produced by accelerated electrons in presence of high magnetic fields. Labelling ambient photons with the subscript ϵ we can rewrite the process as:

$$p + \gamma_\epsilon \rightarrow \Delta^+ \rightarrow \pi^0 + p \quad (1.62a)$$

$$\rightarrow \pi^+ + n \quad (1.62b)$$

The cross-section of the process at resonant energy is about $\sim 250 \mu\text{b}$ for each channel, which is two orders of magnitude smaller than the cross-section for the proton-proton interaction. Nevertheless, in some environments the population density of ambient photons can be much larger than the one of environmental matter, so that the probability of Eqs. 1.62a,1.62b is much higher than the probability of Eq. 1.61. The spectral index of γ -rays in this model is strictly connected to the spectral index of the CR spectrum, since $\Phi_\gamma(E) \propto \Phi_{\text{pions}}(E) \propto \Phi_{CR}(E)$, and $\alpha_{CR} \sim \alpha_\gamma$. This holds for a transparent source, i. e. with a size much larger than the proton interaction length, but smaller than the pion and kaon interaction length, so that protons have a large probability of interacting while secondary mesons can decay before interacting. Hence, γ -ray measurements can give essential information on primary CRs, since they can represent the proof of the presence of high-energy CRs.

In order to understand the sources and mechanisms of CR acceleration a possibility would then be the detection of γ -rays and the capability of distinguishing between the contribution of the hadronic model and the one of the leptonic model: recognizing the hadronic or leptonic origin of detected photons would indeed clarify whether proton and electron accelerators are of different nature. Unfortunately this is a major challenge since in most cases it is generally possible to fit very high-energy γ -ray data with both models, by varying the model parameters properly. At present, no single Galactic or extra-Galactic source has been ultimately proven to accelerate CRs up to PeV energies. At this point, we must shift our attention to the other neutral particle: the neutrino.

1.4.2 Neutrino production mechanisms

Astrophysical neutrinos are produced via the decay of charged pions produced in processes Eq. 1.61 and Eqs. 1.62a,1.62b:

$$\begin{aligned} \pi^+ &\rightarrow \mu^+ \nu_\mu \\ &\hookrightarrow \mu^+ \rightarrow e^+ \nu_e \bar{\nu}_\mu \end{aligned} \quad (1.63a)$$

$$\begin{aligned} \pi^- &\rightarrow \mu^- \bar{\nu}_\mu \\ &\hookrightarrow \mu^- \rightarrow e^- \bar{\nu}_e \nu_\mu \end{aligned} \quad (1.63b)$$

Thus, the mechanisms that produce CRs and γ -rays produce also neutrinos, and candidate neutrino sources are usually also γ -rays sources. Hence, the spectral index of neutrinos is connected to the one of photons and of CRs: recalling what has been said in the previous subsection, it holds $\alpha_{CR} \sim \alpha_\nu \sim \alpha_\gamma$. While γ -rays can be produced both in the leptonic and in the hadronic scenarios, neutrinos can only be produced by hadronic processes. Consequently, the detection of astrophysical neutrinos undoubtedly points towards a source where an hadronic process is undergoing.

Let us now make a simple evaluation of the energy distribution of the produced pions, photons and neutrinos. Experimental observations show that on average, in the process Eq. 1.61, the fraction of the initial proton energy carried by the highest energy pion is $1/5$ [78]. For what concerns the neutral pion, the two photons produced in its decay carry $1/2$ of the parent pion energy each. Instead, in the charged pions decay chain Eqs. 1.58a,1.63 each of the four leptons carry about $1/4$ of the parent pion energy. Thus

the following simple relation between neutrino energy and primary CR energy can be derived:

$$E_\nu \sim \frac{E_\gamma}{2} \sim \frac{E_\pi}{4} \sim \frac{E_p}{20} \quad (1.64)$$

A similar relation holds also for the photoproduction processes Eqs. 1.62a, 1.62b, since by kinematic considerations one obtains that, on average, the pions carry 1/5 of the initial proton kinetic energy. This means that for instance the detection of neutrinos of energy $E_\nu = 100 \text{ TeV} - 10 \text{ PeV}$ corresponds to a parent proton energy of about $E_p \sim 2 \text{ PeV} - 200 \text{ PeV}$. There are however differences between the photoproduction processes and the pp -processes, concerning mainly the spectrum:

1. The photoproduction mechanism, analogously to the GZK cut-off, is a process with a defined threshold. Here, however, the ambient photons (mainly produced by bremsstrahlung radiation) frequencies range between the UV and X bands: if we consider for instance a target photon with energy $E_\gamma \sim 0.1 \text{ eV}$, the parent proton must have a threshold energy of:

$$E_p > \frac{m_\Delta^2}{4E_\gamma} = \left(\frac{100 \text{ eV}}{E_\gamma} \right) \times 4 \text{ PeV} \quad (1.65)$$

which, according to Eq. 1.64, results into a neutrino energy of $\sim 200 \text{ TeV}$. In this case, the neutrino spectrum will reflect the energy distribution of the ambient target photons.

2. The pp -mechanism instead is characterized by the hypothesis of limiting fragmentation, or scaling [97]. According to this hypothesis, the secondary particle spectrum corresponds quite strictly to the primary one: if CRs are power-law distributed, also neutrinos and high-energy γ -rays will be power-law distributed, with almost the same slope. We already mentioned this feature in the previous subsection. In particular, in the case of Fermi acceleration mechanism, we have $\alpha_{CR} \simeq \alpha_\gamma \simeq \alpha_\nu \sim 2$.

Other differences are related to the proportions of the produced neutrinos and γ -rays. While cosmic ray nuclei will still produce neutrinos in pp -processes from individual nucleons, $p\gamma$ -collisions will mostly lead to photo-disintegration of the nuclei, attenuating their energy and resulting in a reduction in the production of secondary neutrinos. Finally, due to isospin conservation, the branching ratio for the process Eq. 1.62a is about twice as large as the one for the process Eq. 1.62b, so that a relatively larger amount of neutral pions is produced than for the pp -mechanism, yielding more γ -rays than neutrinos.

1.4.3 Neutrino and γ -ray Astronomies

Even though the spectra of γ -rays and neutrino, as explained previously, are strictly connected to the spectrum of the primary CRs and to each other, a direct connection between high-energy neutrinos and γ -rays is not so straightforward and requires certain assumptions to be fulfilled. We already mentioned some differences: γ -rays can be produced also in the leptonic mechanisms whereas neutrinos can not; γ -rays can be absorbed in the source if it is thick enough, or by an opaque object along its path. In

addition, γ -rays propagating for long distances may be absorbed in the interaction with background photons via a pair production mechanism:

$$\gamma + \gamma_{\text{bkgr}} \rightarrow e^+ + e^- \quad (1.66)$$

It can be shown [78] that this attenuation effect not only is relevant for propagation over extra-Galactic distances, but it is not negligible for the highest energy Galactic cosmic rays. When the contribution of background infrared photons due to dust-reprocessed star light is included, the Universe is expected to become opaque already at the TeV energy scale. Thus, at the highest energies, the connection between extra-Galactic γ -rays and neutrinos is indirect, and specific detailed numerical codes come into play.

On the contrary, there are other cases in which the connection is more direct. If the hadronic case is at work in a Galactic source, for instance in a SNR, a flux of neutrinos comparable to that of γ -rays might be expected. This is the case of the SNR RX J1713.7-3946, one of the best studied SNRs in the very high energy regime. Its γ -ray spectrum is the subject of an ongoing debate about its nature: at present neither the hadronic nor the leptonic scenarios can be excluded. In any case, its γ -ray flux, as measured by the H.E.S.S. telescopes, can put some constraints on the expected neutrino flux, whose predictions [33] result in:

$$E_\nu^2 \frac{d\Phi_\nu}{dE_\nu} \simeq 10^{-11} \text{ TeV s}^{-1} \text{ cm}^{-2} \quad (1.67)$$

For a source like RX J1713.7-3946, it has been shown [33] that a neutrino telescope such as the KM3NeT detector may be able to make an observation with 3σ significance in about six years of operations. On the other hand, if no signal will be observed after about 5 years, the hadronic contribution to the γ -ray emission can be constrained to be less than 50%.

1.4.4 Neutrino fluxes

Concerning the expected neutrino fluxes on Earth, several contributions sum up and constitute the spectrum shown in Fig. 1.9. The *conventional atmospheric neutrino flux*, introduced in Sec. 1.3 and shown in the Fig. 1.9 as a solid black line, considers only ν_μ and $\bar{\nu}_\mu$ contributions to the overall atmospheric neutrino flux, since the ν_e component is heavily suppressed. The *prompt component* (see Sec. 1.3) derives from the decay of charmed mesons, and is shown in two different models with dashed black lines in the figure. For energies between 1 – 100 TeV the conventional flux follows the power-law spectrum like in Eq. 1.28 with $\alpha \simeq 3.7$, as experimental points confirm. The prompt harder spectrum is expected to exceed the conventional one at energies higher than ~ 100 TeV.

In the $10^{14} - 10^{18}$ eV energy region the upper bound for an extra-Galactic diffuse neutrino flux, as derived in [95] by Waxman and Bahcall, is indicated with a full green line. In the original paper, the flux is estimated taking into account only the contribution of AGNs and GRBs, and neglecting neutrino oscillations. According to their assumption (and considering oscillations) the maximum ν_μ flux becomes:

$$[E^2 \Phi_{\nu_\mu}(E)]_{\text{max}} \approx 0.9 \times 10^{-8} \text{ GeV cm}^{-2} \text{ s}^{-1} \text{ sr}^{-1} \quad (1.68)$$

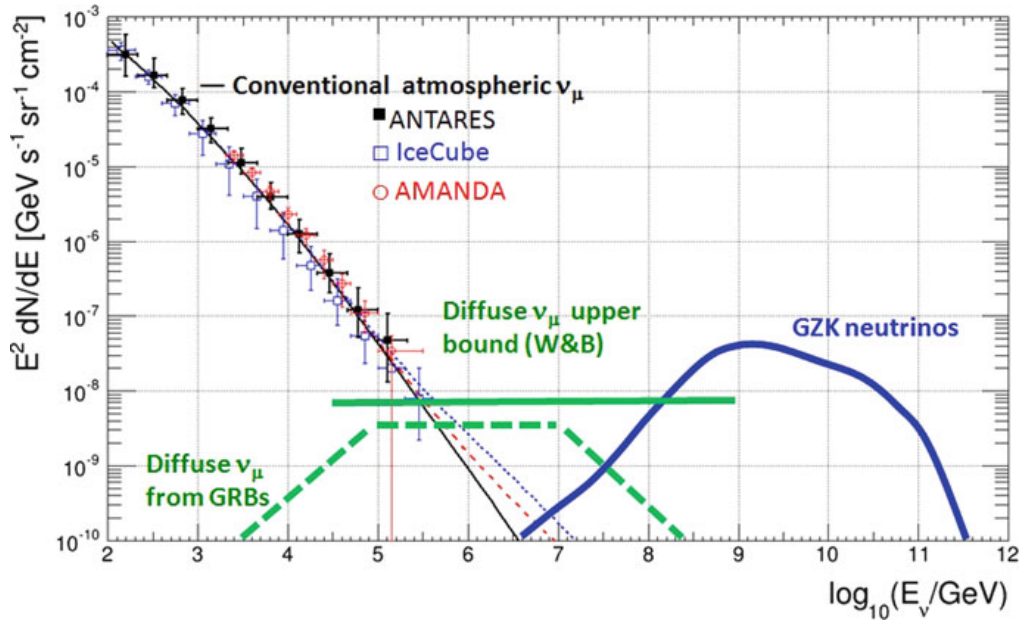


Figure 1.9: Expected neutrino fluxes: the black line represents the expected *conventional atmospheric neutrino* flux and the nearby dashed black lines include the contributions of two different models of *prompt neutrino* fluxes from charmed mesons decays. The full green line constitutes the Waxman and Bahcall upper bound from a diffuse neutrino flux coming from extra-Galactic sources. The dashed green line instead is the upper bound for neutrinos produced in GRBs. Eventually, the blue line shows the possible contribution of cosmogenic neutrinos. Experimental points represent measurements of the atmospheric $\nu_\mu + \bar{\nu}_\mu$ flux as a function of energy by ANTARES, IceCube and AMANDA experiments. Figure taken from [91].

This diffuse component is expected to overcome the atmospheric flux contribution above few hundreds of TeV. Note that this upper limit regards only ν_μ : the all-flavor upper limit is a factor of three larger than Eq. 1.68. Another possible contribution may come specifically from GRBs: in the fireball model (Sec. 1.2.5) protons are shock-accelerated yielding high-energy neutrinos in concomitance with the electromagnetic signal of the burst due to the acceleration of electrons. Waxman and Bahcall again in [95] computed an estimation for the maximum neutrino flux coming from this kind of sources, which is:

$$[E^2 \Phi_{\nu_\mu}(E)]_{\max}^{\text{GRB}} \approx 3 \times 10^{-9} \text{ GeV cm}^{-2} \text{ s}^{-1} \text{ sr}^{-1} \quad (1.69)$$

In Fig. 1.9 this contribution is shown with the dashed green line. The flux indicated with the blue line is the contribution of *cosmogenic* neutrinos: these are ultra-high-energy neutrinos produced by UHECRs, which during their journeys cover cosmological distances and interact with the CMB radiation. Ultra-high-energy protons can produce neutrinos of energies typically 1/20 of the proton energies (Sec. 1.4.2) via the process in Eq. 1.62b, while for nuclei this process is significantly suppressed. Thus, a sizeable flux of cosmogenic neutrinos at EeV energies is expected only if UHECRs above the GZK cut-off are protons.

Therefore, from Fig. 1.9 it becomes clear that there are two different approaches in the quest for astrophysical neutrinos: they can be searched either from a specific direction as an excess of events over the background (point-like searches), or globally as an excess of high-energy events (diffuse search) above ~ 100 TeV, where the diffuse astrophysical flux overcomes the atmospheric one.

1.4.5 Astrophysical neutrinos detection

The first evidence of astrophysical neutrinos was obtained by the IceCube detector, which observed them in two different and independent event samples which showed an excess of neutrinos in the high energy region with respect to the expected conventional atmospheric flux. The first one comprised neutrino events, called *High Energy Starting Events* (HESE), whose interaction vertex was contained inside the instrumented volume: an excess of high-energy events over the atmospheric background has been collected between 2010 and 2016 [16]. Measurements are shown in Fig. 1.10. The background-only hypothesis was disfavored with a statistical significance larger than 6 standard deviations with respect to the hypothesis of contributions from astrophysical sources. The best fit to data yields a spectral index for the neutrino spectrum of about $\alpha_\nu \sim 2.9$. Poor angular resolution prevents the accurate location of the sources of these neutrino signals.

The second data sample was formed by selecting charged-current upgoing muon neutrino events and using eight years of data collected from 2009 to 2017 [63]. The sample contains ~ 500.000 muon neutrino candidates with a negligible contribution of atmospheric muons. For each event the median neutrino energy was calculated starting from the reconstructed neutrino energy and using it to produce via an unfolding method the posterior probability density function of the true neutrino energy: their spectrum is shown in Fig. 1.11, where a clear excess above ~ 100 TeV, which is not compatible with the atmospheric neutrinos expectation, is visible. In this case the significance of the observation with respect to the background-only hypothesis was at 6.7σ and again no

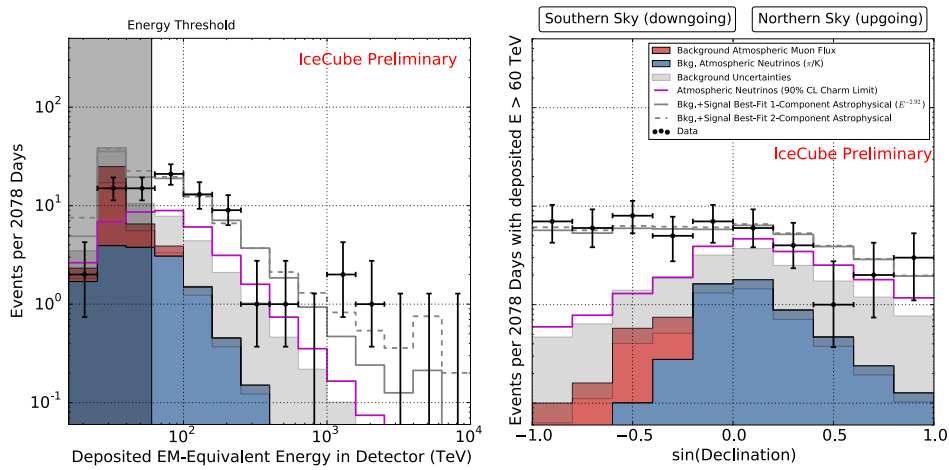


Figure 1.10: **Left:** deposited energies by neutrinos interacting inside IceCube observed in six years of data. The gray region shows uncertainties on the sum of all backgrounds. Also shown are the atmospheric muons and neutrinos flux and two fits to the spectrum, assuming a simple power-law (solid gray) and a broken power-law (dashed gray). **Right:** the same data and models showing the distribution of events with deposited energy above 60 TeV as a function of the sine of the declination (negative values in the Southern Hemisphere). For details see [16], whence the figure is taken.

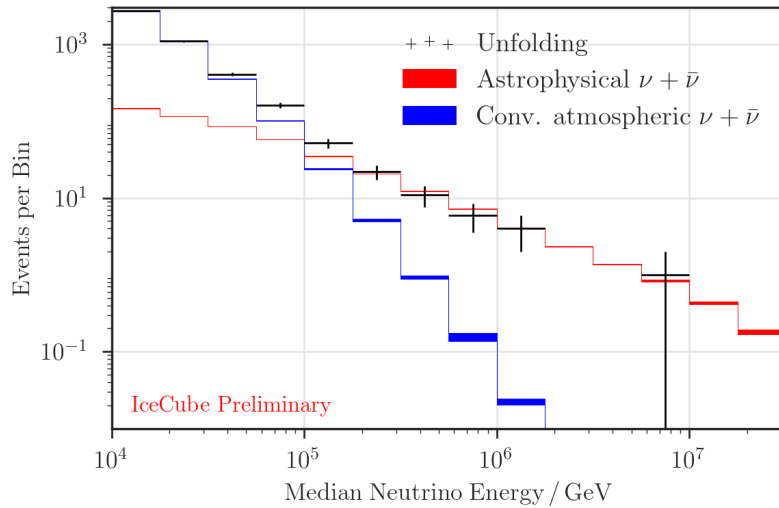


Figure 1.11: Unfolded ν_μ energy spectrum for the passing muon sample in IceCube. Data are compared to the best-fit fluxes for the conventional atmospheric neutrino flux and for the astrophysical one: above ~ 100 TeV data are not compatible with the background-only hypothesis. Figure taken from [16].

correlations with astrophysical sources where found. For this data sample the best fit to measurements results in a spectral index for the spectrum of about $\alpha_\nu \sim 2.2$: the possible origin of the discrepancy between the two sample spectral indices is still debated.

The first correlation of a neutrino event in IceCube with an astrophysical source occurred in September 2017 [17], when IceCube detected a muon-like event induced by a ~ 300 TeV neutrino, alerting other experiments for the searches of the γ -ray counterpart. The Fermi-LAT satellite and the MAGIC telescope reported a coincidence with the neutrino direction of a known γ -ray source, i. e. the blazar TXS 0506+056. The correlation of the observed neutrino with the registered activity of TXS 0506+056 was classified as statistically significant at the level of 3σ . Pushed by this coincidence, the IceCube collaboration examined lower-energy neutrinos detected over the previous years, finding an excess emission at the location of the blazar between September 2014 and March 2015 [18]. Allowing for time-variable flux, data constitutes a 3.5σ evidence for neutrino emission from the direction of TXS 0506+056, independent of and prior to the 2017 flaring episode, suggesting that blazars are candidate sources of a high-energy astrophysical neutrino flux.

1.5 Multi-messenger astrophysics and gravitational waves

Before concluding this brief introductory chapter, it is worth to spend few words about the role of Gravitational Waves (GWs) in Multi-messenger Astrophysics i. e. the discipline which conveys the complementary information carried by different probes such as cosmic rays, photons, neutrino and gravitational waves in order to provide valuable and more complete insights into the properties and the processes of astrophysical sources. We have already encountered one of the most recent successes of the multi-messenger astrophysics: the identification of the first joint electromagnetic and high-energy neutrino source (Sec. 1.4.5). For what concerns gravitational waves, the first detection of a GW by the LIGO collaboration occurred in September 2015 [23] and opened a new window on the Universe. Since then, many other GWs have been detected, but analogously to the neutrino case a new milestone in the development of the multi-messenger scenario was set with the observation in August 2017 by the VIRGO/LIGO collaboration [25] of the first GW in coincidence with its electromagnetic counterpart's signal. The event which originated the GW was the coalescence of two neutron stars about 40 Mpc away from the Earth. In addition, the study of the electromagnetic follow-up in the days following the event revealed the signatures of synthesization of heavy nuclei such as Gold and Platinum, solving a long lasting mystery on the nature of the heaviest elements of the periodic table. On the other hand, no statistically significant excess in the neutrino flux was observed by IceCube, ANTARES and Pierre Auger Observatory collaborations [37]. Until today, no neutrino/GW coincidence has been observed despite the detection of several GWs: the ANTARES collaboration, in collaboration with IceCube and other cosmic ray and γ -ray detectors, has analyzed five events (GW150914, GW151226, LVT151012, GW170104, and GW170817) and no coincidences with neutrinos from the region of interest have been found [88]. Therefore, even though the identification of the first joint electromagnetic/gravitational and electromagnetic/neutrino sources have brought substantial results to the multi-messenger astrophysics, many other questions

are still open which multi-messenger astrophysics may answer to, and even greater rewards are expected in the years ahead, starting from the observation of a coincidence between a GW and an excess of neutrinos. The latter would be of great importance also for neutrino physics since the possible coincident detection could put severe constraints on neutrino mass ordering, and perhaps even on the absolute mass of the neutrino itself, exploiting the measurement of the arrival time difference between the GW and the incoherent neutrino wave packet. These results should be achievable with the advent of the second generation of neutrino telescopes, among which the KM3NeT detector. Thus, in the next chapter we will focus on this topic.

Chapter 2

Neutrino telescopes

Since neutrinos interact exclusively via the Weak interaction and with extremely small cross-sections, their detection is very challenging. In addition, as small fluxes are expected, the usage of a very large target mass with a very good background rejection is essential in order to observe a measurable flux. The idea of using a very large volume of natural water as detection medium was proposed for the first time by M. A. Markov in 1960 [75]. The proposal foresaw the instrumentation of a large volume of water with several optical sensors in order to detect Cherenkov light emitted by the medium along the path of the secondary charged particles produced in the CC interaction of neutrinos in the telescope volume or in water or rocks in its proximity. Position and arrival time of Cherenkov photons as detected by the photosensors would then allow the reconstruction of the direction and the energy of the incoming neutrino and the nature of its underlying interaction. In this concept sea water would act simultaneously as the target, the shield against background atmospheric muons, and the active detection volume. The first serious effort to test the feasibility of a gigaton-scale water detector to search for astrophysical neutrinos was the Deep Underwater Muon and Neutrino Detector (DUMAND) project [40], consisting in the deployment, for few days from a ship, of a single string in the ocean off shore Big Island of Hawaii in 1987. After this pioneering work, the first successful neutrino telescopes, even though with volumes smaller than the gigaton scale, were Baikal [39], installed in the depths of the Siberian Lake Baikal (Russia) in 1999 and the Antarctic Muon And Neutrino Detector Array (AMANDA) [69] completed in 2000 at the Amundsen-Scott South Pole Station, in the Southern hemisphere. AMANDA was the first neutrino telescopes using ice as medium and it was the precursor of the first km^3 scale detector IceCube, built in the same location [55]. It continued to run as a sub-array of IceCube until it was shut off in 2009. Baikal is currently expanding towards a km^3 scale too, planned to become the GVD experiment. The original idea of DUMAND to construct a neutrino telescope in the deep ocean was first realized with the ANTARES detector, consisting in 12 strings of optical modules deployed in the Mediterranean Sea near Toulon and fully operational since 2008, covering a surface area of about 0.1 km^2 [29]. The record of largest neutrino telescope in the Northern hemisphere will soon be snatched from the KM3NeT-ARCA and ORCA detectors, which are under construction in the Mediterranean Sea off shore Sicily in Italy and Toulon in France respectively. Once completed, they will reach an instrumented volume of the km^3 scale. Their unique location in the Northern hemisphere will allow them to survey with a privileged view the sector of the sky comprising the Galactic plane, in contrast to IceCube and its second

generation upgrade planned in the next years, who has a privileged view on the the opposite sector of the sky.

2.1 High-energy neutrino detection

The working principle of neutrino telescopes, common for both underwater and under ice telescopes, is based on the collection of optical Cherenkov photons (refer to Sec. 2.1.1) emitted by the medium along the path of the secondary particles generated in neutrino interactions in the telescope volume or in water or rocks in its proximity. These photons are collected by optical modules containing PMTs, which are arranged usually several tens of meters one after the other along strings. Several strings are then deeply deployed inside drillings in the ice or underwater, anchored to seabed, forming a large scale volume matrix. In order to be sensitive to events coming from different directions, neutrino telescopes should be as isotropic as possible.

High energy neutrinos interact with nucleons of nuclei in the medium via either charged current (CC) weak interactions or neutral current weak interaction (NC). Depending on the flavor of the neutrino and on the kind of interaction, different signatures are expected in the pattern of arrival time and intensity of the light signal on optical modules. Those signatures allow us to reconstruct the main features of the event and the direction and energy of the incoming neutrino. The major difference regards the signatures of muons and electrons or taus. Long tracks are produced by CC ν_μ interactions since the produced muons are highly penetrating particles with a range in water of several kilometers for energies larger than a few hundreds of GeV, as one can see from Fig. 2.2. In this case, the muon's path length usually exceeds the detector's spatial resolution, so that the trajectory of the particle can be resolved with high accuracy. The long range allows muons to be tracked down through the detector even if they are generated in up-going neutrino interactions occurring in the rocks kilometers below the instrumented volume. On the other hand, ν_e and ν_τ CC interactions produce leptons which develop showers: the parent neutrinos can be identified as well, but with a worst angular accuracy with respect to muon neutrinos. Showers are also produced in NC interactions of all neutrino flavors. We will come back on this in Sec. 2.2.

Given the small neutrino cross sections and the expected cosmic neutrino fluxes as derived from γ -ray fluxes, simple considerations motivate the need of at least a cubic-kilometer volume of target material in order to observe a rate of few events per year, as shown in [91]. Their location deep under kilometers of ice or water is required in order to shield the detector with a large amount of material from the background, represented by atmospheric neutrinos and atmospheric muons. These are produced in the showers developed in the atmosphere by protons and heavy nuclei and are generated mainly from the charged pion and kaon decays $\pi \rightarrow \mu \nu_\mu$, $K \rightarrow \mu \nu_\mu$. Atmospheric muons can penetrate up to several kilometers of ice/water and give signals in the detector. Since their flux at the Earth surface is about 10^{11} larger than the expected flux of astrophysical neutrinos and exceeds by many order of magnitude the flux of atmospheric neutrinos, they represent the bulk of reconstructed events in any neutrino telescope. It follows that, at least at present, *down-going* muons produced by down-going neutrinos cannot be considered in the search for astrophysical neutrinos, being signal completely hidden under the overwhelming background. Therefore, the only good candidate muons generated by

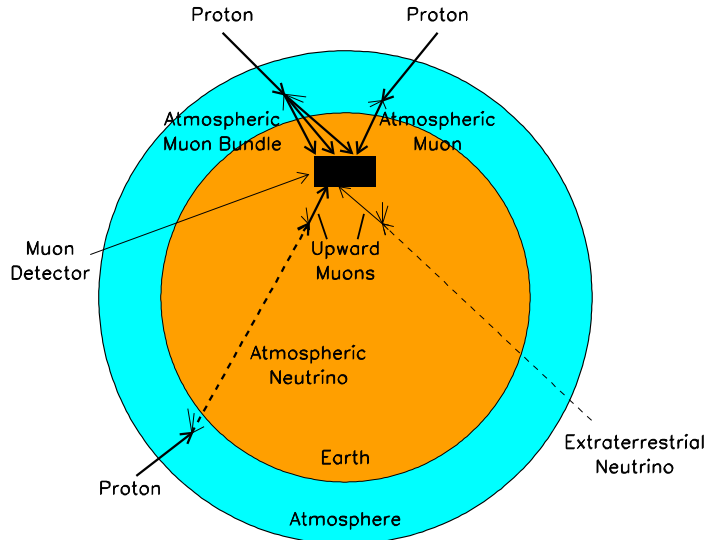


Figure 2.1: Schematization of a neutrino telescope as a muon detector deep underground. Down-going muons produced by protons in the atmosphere represent the main background for the detector, together with muons (from any direction) related to atmospheric neutrinos. Only up-going muons coming from astrophysical neutrinos constitute the signal we would like to detect in principle.

astrophysical neutrino interactions are the upward-going ones: as a matter of fact, only neutrinos are able to pass undisturbed through the entire thickness of the Earth, which has a diameter of almost 13000 km, and to interact beneath or inside the target volume generating *up-going* muon events, while atmospheric muons cannot traverse the Earth in no way, for their maximum range in water at the highest energies of 10^8 GeV is smaller than 50 km, as it can be seen in Fig. 2.2.

Muons produced by atmospheric neutrinos represent the other source of background. Since these can come even from the bottom, they constitute an irreducible background in every experiment aimed at the detection of cosmic neutrinos. This situation is depicted in Fig. 2.1. Nevertheless, it can happen that some down-going events are mis-reconstructed as up-going events and these affect the statistical sample of candidate signal. Reducing at most this kind of bad classification represents one of the most important feature of the detector.

2.1.1 Cherenkov radiation

The *Cherenkov radiation* is an effect arising when a charged particle propagates in a medium of refractive coefficient n with a velocity $v = \beta c$ which is larger than the speed of light in that medium c/n . In this case, collimated photons at a specific angle θ_C , called *Cherenkov angle*, are produced. As a matter of fact, the passage of such a particle polarizes the atoms along its path in an asymmetrical arrangement, inducing a net dipole moment which causes emission of Cherenkov photons when those atoms return back to the initial configuration. In such cases, a coherent conical wavefront is emitted, at a well-defined angle:

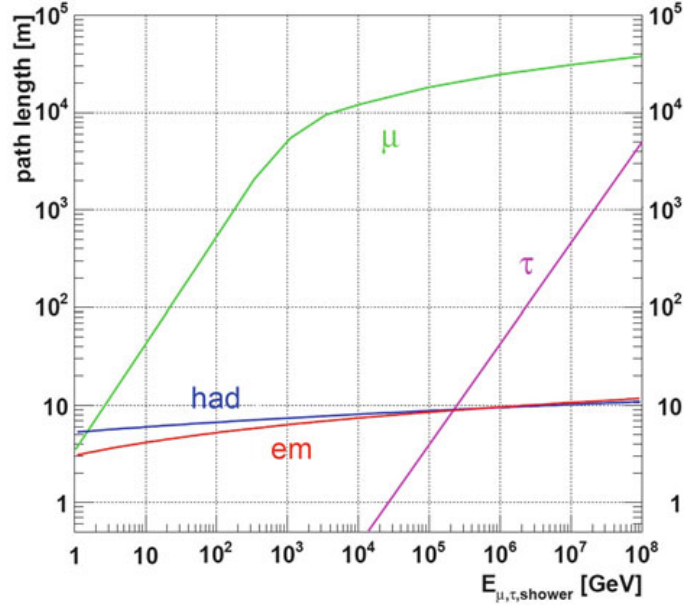


Figure 2.2: Path length of muons (μ), taus (τ), electromagnetic (em) and hadronic (had) showers in water as a function of energy.

$$\cos \theta_C = \frac{1}{\beta n} \quad (2.1)$$

with respect to the particle's trajectory. This implies a threshold velocity β_{thr} for the incoming particle equal to

$$\beta_{thr} = \frac{1}{n} \quad (2.2)$$

and thus a threshold energy for Cherenkov emission of

$$E_{thr} = \frac{mc^2}{\sqrt{1 - 1/n^2}} \quad (2.3)$$

where m is the mass of the particle. The corresponding kinetic energy threshold T_{thr} is then just $T_{thr} = E_{thr} - mc^2$. This situation is depicted in Fig. 2.3.

The number of photons [72] emitted per unit wavelength $d\lambda$ per unit path dx as a particle passes through the radiating medium is:

$$\frac{d^2 N}{d\lambda dx} = \frac{2\pi z^2 \alpha}{\lambda^2} \left(1 - \frac{1}{\beta^2 n^2(\lambda)} \right) \quad (2.4)$$

where α is the fine structure constant and z the atomic number of the radiating medium.

Let us consider now sea water as medium. In the wavelength range from about 300 nm to 600 nm, in which water is transparent, the number of emitted photons per unit path length, obtained by integrating 2.4, is:

$$\frac{dN}{dx} \simeq 340 \text{ photons/cm} \quad (2.5)$$

In this wavelength region, the refractive index of water is $n \simeq 1.35$, which for a highly relativistic particle with $\beta \simeq 1$ results in a Cherenkov angle $\theta_C \simeq 42^\circ$. The kinetic energy

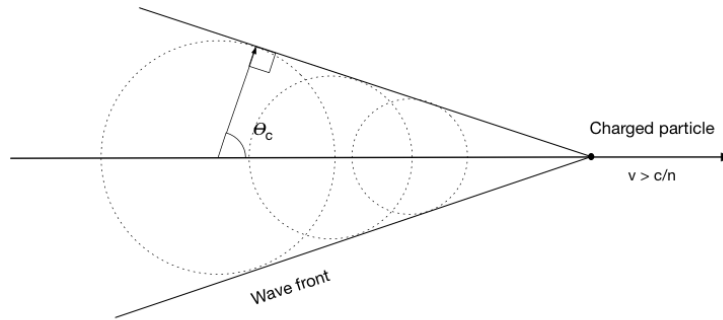


Figure 2.3: Scheme of the Cherenkov radiation. The propagation direction of the charged particle is represented together with the Cherenkov angle θ_C and the wavefronts formed by all the spherical lightwaves produced during the passage of the particle.

threshold corresponds to the values of $T_{thr}^e \simeq 0.25$ MeV for electrons, $T_{thr}^e \simeq 53$ MeV for muons, and $T_{thr}^e \simeq 450$ MeV for protons.

Water properties

Light propagation in a medium is characterized by absorption and scattering of photons. These affect the reconstruction capabilities of the telescope, since absorption reduces the number of photons arriving on PMTs, whereas scattering changes the direction of Cherenkov photons, consequently delaying their arrival time on the PMTs: this results in a degraded angular resolution of the incoming particle. In order to describe these effects, we introduce two parameters: the *absorption length* λ_{abs} and the *scattering length* λ_s . Each of these quantities represents the path after which a beam of light of initial intensity I_0 and wavelength λ is reduced in intensity by a factor of $1/e$ through absorption or scattering, according to:

$$I(x) = I_0 \exp(-x/\lambda_{abs}) \quad (2.6)$$

where x is the distance travelled by the photons. Sea water shows maximum transparency for ~ 400 nm photons, with an absorption length equal to $\lambda_{abs} \approx 60$ m.

For what concerns scattering, an effective scattering length can be defined which takes into account, together with λ_s , the angular distribution of the momentum of the outgoing particles. Scattering typically takes place on water molecules (“Rayleigh scattering”) or on larger particulates (“Mie scattering”) [15]. The effective scattering length is:

$$\lambda_s^{eff} = \frac{\lambda_s}{1 - \langle \cos \theta_s \rangle} \quad (2.7)$$

where $\langle \cos \theta_s \rangle$ is the average scattering angle. In sea water typical values are $\lambda_s \approx 55$ m and $\lambda_s^{eff} \approx 265$ m, as measured for photon wavelength of 470 nm [15].

2.2 Neutrino signatures

In a neutrino telescope events can be separated in two distinct classes: *track*-like events and *shower*-like events. Track-like events are due to muons originated in a ν_μ CC

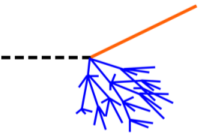
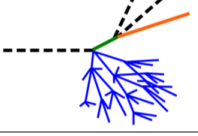
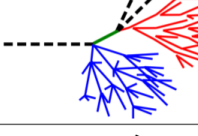
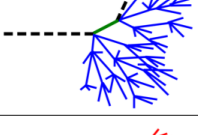
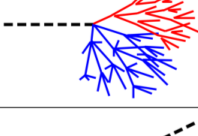
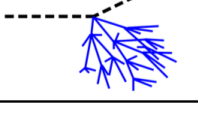
Interaction	Particle signature	Detector signature
$\bar{\nu}_\mu$ CC		hadronic shower and μ track
		track-like
		hadronic shower and μ track ($\tau^\pm \rightarrow \mu^\pm \bar{\nu}_\mu \bar{\nu}_\tau$, $\sim 17\%$ BR)
		hadronic and EM shower ($\tau^\pm \rightarrow e^\pm \bar{\nu}_e \bar{\nu}_\tau$, $\sim 18\%$ BR)
		hadronic showers ($\tau^\pm \rightarrow \text{hadrons}$, $\sim 65\%$ BR)
		point-like or shower-like
$\bar{\nu}_e$ CC		hadronic and EM shower
$\bar{\nu}$ NC		hadronic shower

Figure 2.4: Event signatures of neutrino-induced events in neutrino telescopes. Neutrinos are identified by dashed black lines, muons by orange lines, e^+ , e^- in EM showers by red lines, secondary particles in hadronic showers by blue lines and τ by green lines. In the upper ν_τ CC channel the *double-bang* signature can be seen.

interaction and they are characterized by long tracks since muons have a long path length in water or ice, while *shower-like* events are produced by the CC interactions of ν_e , ν_τ and NC interactions of all neutrinos and they are characterized by the presence of an electromagnetic (EM) or a hadronic (or both) shower, as the produced particles propagate only for a few tens of meters. In all cases, no separation between particles and antiparticles can be made; hence, neutrino and anti-neutrino reactions cannot be distinguished. The event signatures are summarized in Fig. 2.4 and briefly discussed in the following.

2.2.1 Muon neutrino track-like events

Muon neutrinos CC interactions produce a muon crossing the detector with a long track and a clean experimental signal. Inspecting Fig. 2.2 one can see that muons with energy larger than ~ 200 GeV have a path length in water longer than one kilometer, which exceeds the detector's spatial resolution, allowing us to resolve its trajectory with high

angular resolution. The accurate muon track reconstruction in turn allows the accurate reconstruction of the parent neutrino track, since those are closely correlated. The kinematics of the interaction is such that the angle between the produced muon and the parent neutrino is small, of the order of few degrees, and decreases with the energy. This can be seen in Fig. 2.5: in this simulation for the ANTARES telescope the angular resolution gets better than 1° above ~ 600 GeV reaching a maximum precision of about 0.2° above 100 TeV. At these energies, multiple scattering affects the muon direction negligibly, and muon and neutrino can be considered almost collinear. For what concerns the energy, the main energy loss channels for the propagating muon are by ionization of the medium and by radiative losses such as bremsstrahlung radiation and pair production, a contribute which increases with energy:

$$\left\langle -\frac{dE}{dx} \right\rangle = \alpha(E) + \beta(E)E \quad (2.8)$$

where α and β refer respectively to ionization and radiative energy losses.

Energy loss by Cherenkov radiation constitutes only a negligible fraction of the total energy loss, and this is the reason why the neutrino energy reconstruction is much more complicate for muon events than for shower-like events. For energies greater than few TeVs, the radiative processes overcome the loss by ionization and become dominant, generating electromagnetic showers alongside the muon track and in this way characterizing the event classification for muon neutrinos in the TeV-PeV energy range. Eventually, the muon slows down and decays at rest into two neutrinos and an electron which produces an electromagnetic shower.

2.2.2 Shower-like events

Electron neutrinos

An electron neutrino CC interaction produces a high-energy electron which propagates for only few tens of cm (for the radiation length in water is about 36 cm) before radiating a photon via bremsstrahlung and starting an electromagnetic shower. Moreover, in the proximity of the interaction vertex (the nuclear interaction length in water is about 83 cm), an hadronic shower is also generated by the hadronic system X in Eq. 1.3a. The longitudinal extension of these showers are of the orders of a few meters (look at Fig. 2.2), while the lateral extension is negligible compared to the longitudinal. These distances are shorter than the interspace between two sensitive elements in neutrino telescopes; therefore, showers represent point-like sources of Cherenkov photons induced by shower particles. On the one hand this results in a poor angular resolution because the neutrino's direction determination is much more difficult compared to a track-like event; on the other hand, however, this feature makes the neutrino's energy estimation much easier and more reliable with respect to track-like events, since all the neutrino's energy is contained in the showers.

However, the developments and the features of the EM and hadronic showers are somewhat different. In EM showers the total Cherenkov light yield is proportional to the initial energy with fluctuations smaller than 1%, allowing a precise calorimetric measurement. On the contrary, given the same energy, hadronic showers produce less Cherenkov photons, because hadrons in the shower development are more massive than

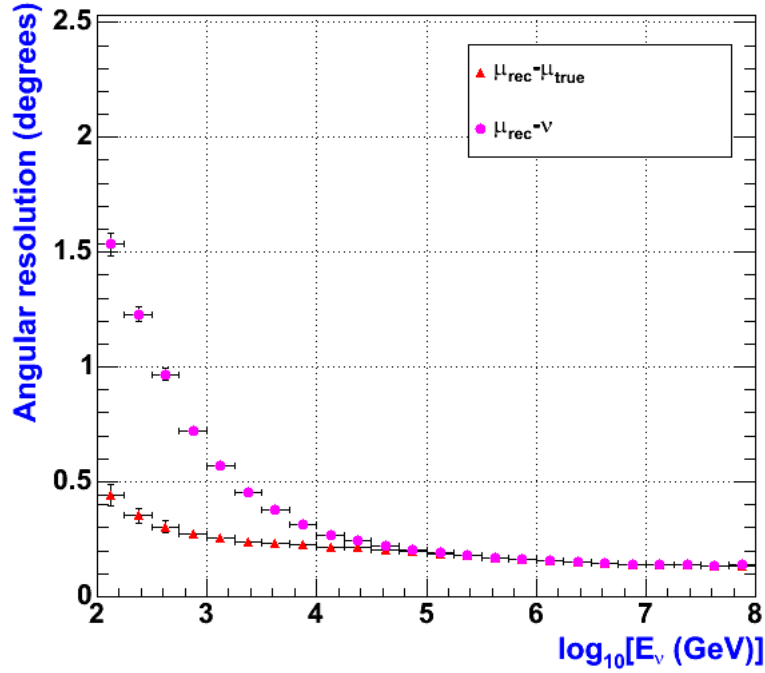


Figure 2.5: Angular resolution as a function of the neutrino energy as simulated with Monte Carlo for the ANTARES neutrino telescope. Triangles represent the average discrepancies between the reconstructed muon and the real muon directions, while circles the discrepancies between the reconstructed muon and the parent neutrino directions. Figure taken from [91].

electrons or positrons, and thus, for Eq. 2.3, have larger energy thresholds for Cherenkov emission. At high energy, though, this effect decreases as all secondary particles reach the energy threshold, and the Cherenkov average light yield for hadronic showers approaches that of EM showers.

Another difference concerns the fluctuations in the shower: event-to-event fluctuations in the Cherenkov light yield are much more important in hadronic showers than in EM showers because of the intrinsic fluctuations in the number, the type and the kind of interactions of secondary particles in a hadronic shower. In addition, for small energies (few GeVs) the initial hadronic shower particle angular distribution is quite spread and the angles between secondary particles are of the order of tens of degrees. Hence, this causes the presence of several Cherenkov light cones with different light yield depending on the hadrons which generated them and their energy. For this kind of showering events, many different signatures of hadronic showers are possible. As with muons, with increasing energy the secondary initial hadrons become more collinear with the parent hadron and less spread, so that the individual Cherenkov cones overlap and the global angular light distribution approaches that of electromagnetic showers. Therefore telescopes targeting neutrinos with energies greater than the TeV do not normally distinguish between EM or hadronic showers.

Neutral Current channel

The NC channel in Eq. 1.4 gives the same signature for all three neutrino flavors, i. e. a Cherenkov light distribution emitted by the hadronic shower generated by the hadronic system X . In this case however, since a fraction of the initial neutrino energy is carried away by the undetected outgoing neutrino, the accuracy on the event energy reconstruction is reduced accordingly.

Tau neutrinos

The signature of a ν_τ depends greatly on its energy. As a matter of fact, by looking at Fig. 2.2 one can see that for τ energies below ~ 1 PeV the τ path length is shorter than the longitudinal dimensions of showers, and therefore its track cannot be resolved. At the end of its track the τ decays producing a second shower. Consequently, the CC ν_τ channel belongs to the showering events, unless the τ produces a muon in its decay, in which case the muon track can be resolved as usual. For greater energies instead, the τ track is typically long enough to allow a separation between the Cherenkov light of the first shower due to the hadron X and light of the second shower caused by the τ decay: this signature is called a *double-bang event* and it is characterized by the presence of a first showers and a following one, connected by a track.

2.3 Background sources

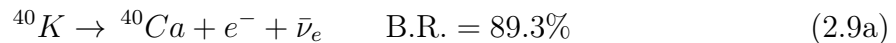
In a water neutrino telescope such as KM3NeT, two different types of noise combine to form the background in the detector: the *environmental* background and the *physical* background. Let us review them.

2.3.1 Environmental background

As we have seen, particle tracks in a neutrino telescope are reconstructed via the Cherenkov photons induced in the medium and detected by PMTs. It follows that any photon which propagates in the detector volume and which does not come from an event track's Cherenkov light constitutes a spurious signal that we need to reject. At the depths in which a neutrino telescope is located, two environmental sources of this optical background are present: the Cherenkov photons originating in the decays of radioactive elements in sea water and the *bioluminescence*, i. e. light produced by biological organisms.

Radioactivity

In the β -decay of radioactive elements dissolved in sea water, the product particles can induce Cherenkov light which constitutes a background source. Among all radioactive elements which can be found in sea water, the most abundant one is ^{40}K , which has two main decay channels:



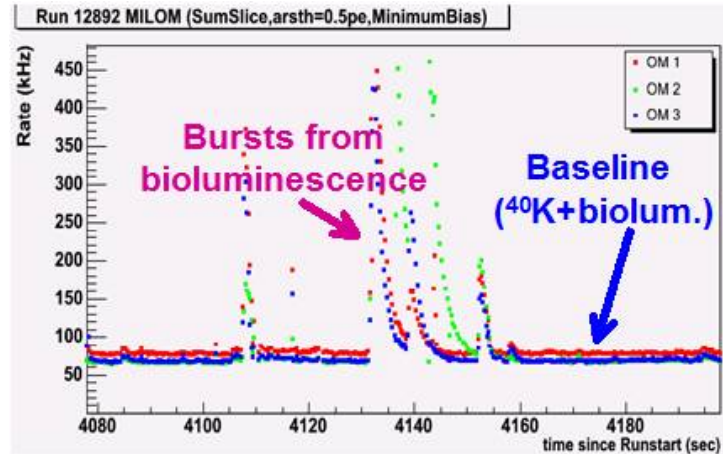


Figure 2.6: Photomultiplier count rate, as function of time, for a typical stream of data collected by ANTARES. The baseline indicates the contributions of the ^{40}K decay and the constant signal from bioluminescence. The dark current count rate of the PMT gives a constant contribute as well. Bursts lasting several seconds are also visible. Figure taken from [15].

The electron produced in Eq. 2.9a has often sufficient energy to induce Cherenkov light in water and in Eq. 2.9b the photon has an energy of 1.46 MeV, which is enough to accelerate electrons via Compton scattering to energies over the threshold for Cherenkov light emission. Even though PMT hits due to ^{40}K decays are uncorrelated there is still a chance that they may mimic the signature of a muon or a shower or, more importantly, contaminate the hit pattern of a neutrino induced event. The intensity of Cherenkov light from ^{40}K radioactive decays depends mostly on the ^{40}K concentration in sea water. Since the salinity in the Mediterranean Sea has small geographical variation, this Cherenkov light intensity is largely site independent and approximately the same contribution is expected to be observed for both the KM3NeT detectors, ORCA and ARCA.

Bioluminescence

Many life forms that inhabit the deep sea emit light. This bioluminescence has two contributions: a continuous and almost constant component, with a variability of the time-scale of seasons, which appears to be related to bioluminescent bacteria, and a component of light bursts with durations of the order of seconds, presumably due to larger size organisms. The distribution of luminescent organisms in the deep-sea varies with location, depth, and time but there is a general pattern of decrease in abundance with depth. These random backgrounds can be reduced by coincidence methods to an acceptable level. For KM3NeT, the mean background rate due to these processes depends on the detector site as they are located at different depths. Considering both the ^{40}K decay and the bioluminescence contributions, the mean background rate per optical module (DOM, see Sec. 2.4.2) in the ARCA detector is ~ 7 kHz, whereas for ORCA is of the order of $O(10)$ kHz.

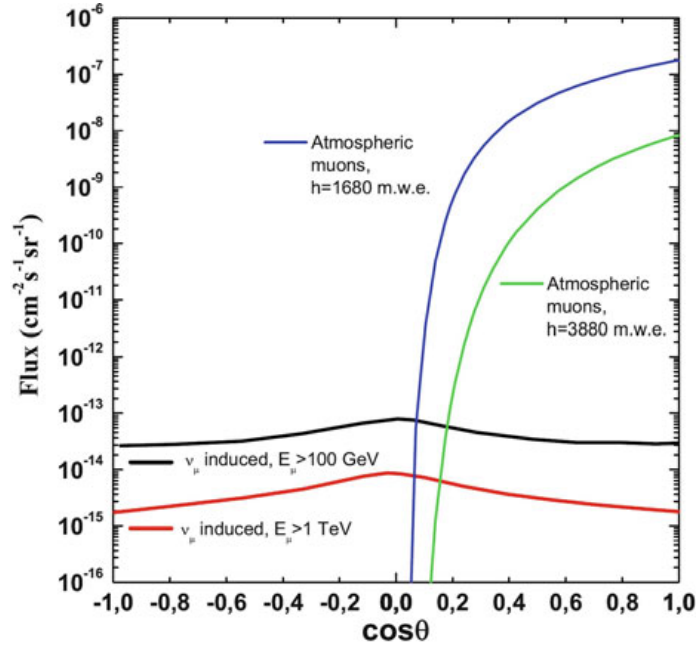


Figure 2.7: Contributions to muon background as a function of the zenith angle. Direct atmospheric muon fluxes are calculated at two different depths (1680 and 3880 meters of water equivalent), while atmospheric neutrino induced muon fluxes are calculated for two different muon energy threshold: the black lines refers to $E_\mu > 1$ TeV and the red line for $E_\mu > 100$ GeV. Figure taken from [91].

2.3.2 Physical background

As we mentioned in Sec. 2.1, only a small fraction of events detected in the detector's target volume are of astrophysical origin, while most part of them constitutes background that must be rejected. Down-going muons can be either produced in the atmosphere in the development of showers or by the decay of atmospheric neutrinos: in both cases they represent a background. At the considered depths, the flux of direct atmospheric muons exceeds by several orders of magnitude the flux of muons induced by atmospheric neutrinos, as shown in Fig. 2.7. As a consequence, the expected background is almost exclusively constituted of down-going muons and, therefore, they can be in principle rejected if we restrict the search for signal exclusively to up-going reconstructed events, as up-going muons can only be produced by up-going neutrinos. In fact, only neutrinos can traverse the Earth and interact inside or near the detector volume, whereas muon maximum range is orders of magnitude shorter than the Earth's diameter. Nevertheless, these up-going neutrinos can be either astrophysical or atmospheric; hence, atmospheric neutrinos represent an always present source of background for a neutrino telescope. For energy larger than about 100 TeV however, the astrophysical neutrino diffuse flux is expected to dominate over the atmospheric one, as shown in Fig. 1.9

Another key problem concerns mis-reconstructed down-going events, which can mimic up-going neutrino induced muons and are therefore extremely dangerous for a detector that searches a signal rate of a few tens of events per year. For this reason it is crucial to reduce as much as possible the direct muon flux, by shielding the telescope deep under

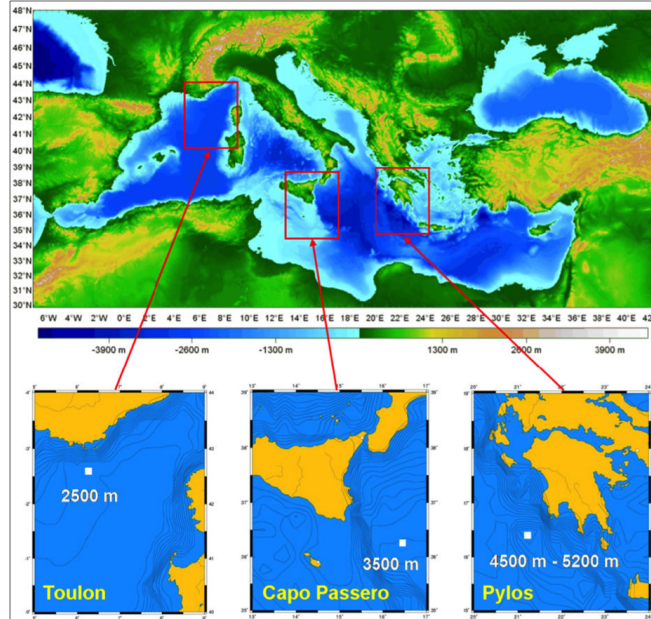


Figure 2.8: Geographical location of the KM3NeT/ARCA and KM3NeT/ORCA neutrino telescopes in the Mediterranean Sea. The third site, KM3NeT-Gr, is located off the coast of Pylos in Greece, and at present is used only for validation and qualification. Figure taken from [74].

kilometers of water, and to improve the reconstruction technique to limit the number of mis-reconstructed events.

2.4 The KM3NeT experiment

KM3NeT [1], which stands for “Cubic Kilometer Neutrino Telescope”, is a multi-km³ next-generation neutrino telescope which is currently under installation phase in the Mediterranean Sea. The design, construction and operation of KM3NeT follow in the footsteps of the precedent neutrino telescopes, in particular of ANTARES. Building on the long-standing experience of ANTARES, KM3NeT is designed to become the largest under-water neutrino telescope, exploiting and improving its predecessor’s detection technique. Once completed, it will be made of two instrumented sites: Oscillation Research with Cosmics in the Abyss (ORCA), located at 40 km offshore Toulon, France at a depth of 2500 m. and Astroparticle Research with Cosmics in the Abyss (ARCA), located at about 100 km offshore Capo Passero, Italy at a depth of 3500 m, as illustrated in Fig. 2.8.

Both detectors will consist of a three-dimensional array of optical modules, called Digital Optical Modules (DOMs), aligned in vertical strings, called Detection Units (DUs), deployed under water and anchored to the seabed. These optical modules will contain photosensors able to collect the Cherenkov photons induced in the water by the particles produced in neutrino interactions, whose trajectories will be then reconstructed. The main difference between ORCA and ARCA lies in the density of the photosensors, which is optimized for each of the two different energy ranges. In addition, the facility will also

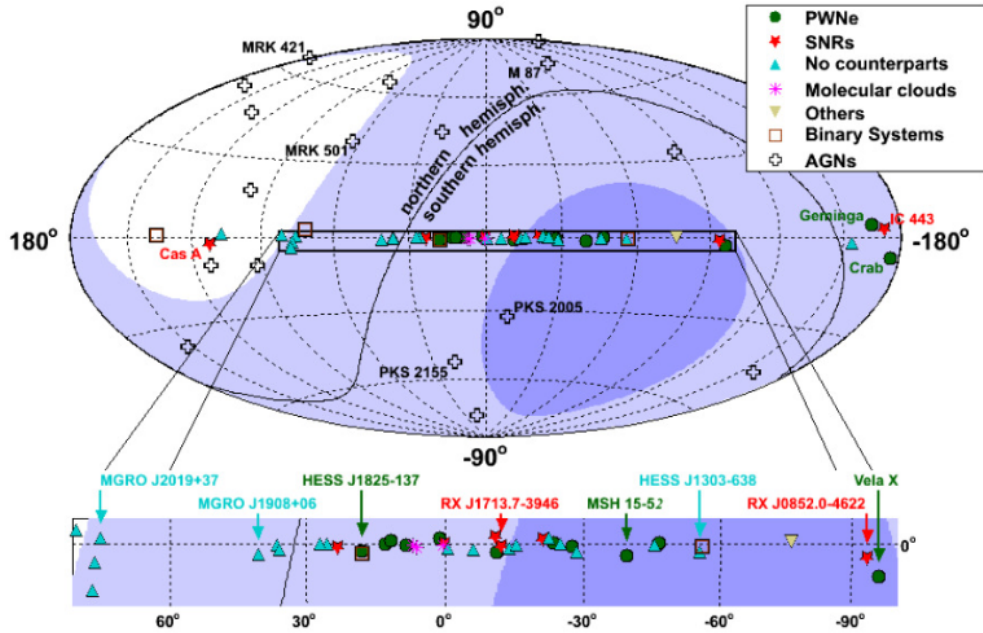


Figure 2.9: Sky coverage of KM3NeT detectors in galactic coordinates. Also shown are some known astrophysical objects. Figure taken from [15].

house instrumentation for Earth and Sea sciences for long-term and on-line monitoring of the deep sea environment and the sea bottom at depth of several kilometers.

2.4.1 ORCA and ARCA sites

As its name hints, ORCA will study the fundamental properties of neutrinos, exploiting the abundant fluxes of neutrinos produced in the interactions of cosmic rays with the Earth's atmosphere.

In particular, it will achieve the angular and energy resolution required for resolving the neutrino mass hierarchy. Dealing with atmospheric neutrinos, it is capable of detecting neutrinos with energy larger than few GeVs and its configuration is optimized for studies of the oscillation region; thus, the strings will contain 18 DOMs interspaced with 9 meters one from the other, while strings will be 20 meters distant one from another. At present, seven strings have been successfully deployed. In the full operational phase ORCA is designed to comprise one building block of 115 detection units.

ARCA aims at detecting high energy neutrinos of astrophysical origin; hence, it is capable of detecting neutrinos with energy larger than 100 GeV and its design is optimized for the detection of neutrinos with energy of the order of the TeV-PeV, which requires a smaller density of DOMs. Each string will contain 18 DOMs, interspaced by 36 meters, and strings will be interspaced by about 100 meters. At present, six strings have been deployed and are taking data. In the final configuration, ARCA will consist of two building blocks of 115 DUs each, reaching an instrumented volume of about one cubic kilometer.

From its location in the Mediterranean Sea, with the ARCA telescope 87% of the sky will be mapped with unprecedented resolution, including most of the Galaxy and

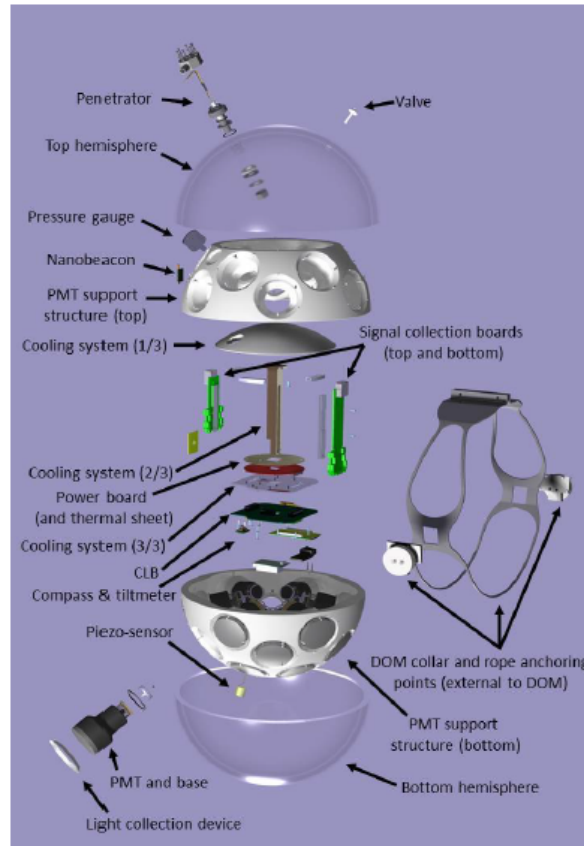


Figure 2.10: Internal structure of a Digital Optical Module. Figure taken from [74].

the Galactic Center, as shown in Fig. 2.9.

2.4.2 Digital Optical Modules

The sensitive elements of the KM3NeT detector are the Digital Optical Modules (DOMs). These are 17-inch glass spheres, resistant to the high pressure present at the sea bottom, housing 31 3-inch photomultiplier tubes (PMTs), their associated readout electronics and power boards, and some additional sensors; these components are shown in Fig. 2.10. The power boards can be controlled individually from the shore in order to set the correct values of HV (about 1000 V per PMT) and discriminating threshold for each PMT. The PMTs are supported by a foam structure and encapsulated inside the glass sphere, with optical gel filling the cavities between the photocathodes and the glass to assure optical contact. Moreover, a reflector ring is placed around each photocathode in order to increase the photon collection efficiency by up to 20-40%, depending on the photon incident angle [74]. The PMTs are arranged in five rings at zenith angles of 50° , 65° , 115° , 130° and 147° , respectively. Six PMTs are arranged along these rings, plus a single PMT placed at the bottom, with a zenith angle of 180° : hence, the lower hemisphere of the DOM contains 19 PMTs and the upper hemisphere 12 PMTs.

PMT photocathodes are made of standard bi-alkali and have a quantum efficiency of about 27% at 404 nm and 22% at 470 nm [31]. This multiple small PMTs configuration, in contrast to “traditional” designs with less, large-area PMTs, offers some advantages:



Figure 2.11: **Left:** an assembled Digital Optical Module. **Right:** internal view of a DOM during assembling phase (incomplete). Pictures taken at the LNS (Laboratori Nazionali del Sud) in Catania, Italy.

it gives a larger total photocatode area over the sphere; it is less sensitive to the Earth's magnetic field, thus not requiring metal shielding; it increases the segmentation of the detection area, improving the discrimination between single-photon and multi-photon hits. PMTs in the DOM register the time of arrival of the Cherenkov photons generated in the sea water and, thanks to their peculiar arrangement inside the DOM, they can give also geometrical information on the direction of those photons. When a photon hits a PMT a small electrical pulse is created, which is then amplified and transformed into a square wave pulse, exploiting the time-over-threshold (ToT) technique. This is sent to a Field Programmable Gate Array (FPGA), hosted on the Central Logic Board (CLB), where the information on its arrival time and pulse length is stored for a subsequent transfer to shore.

In the deep sea DUs are anchored to seabed but they are free to swing around their vertical expansion under the influence of sea currents. Hence, in order to reach a precise angular resolution, continuous calibrating operations are necessary so as to determine and monitor DOM position. For this reason, along with PMTs, DOMs also contain other sensors aimed at calibration purposes: a compass in order to infer the pointing direction of each PMT; accelerometers to measure tilt, pitch and yaw of the module; a gyroscope for measuring rotation; a piezo-acoustic sensor in order to determine the DOM's positioning by exploiting a sonar technique. This acoustic positioning system is expected to measure the positions of DOMs in the sea with an accuracy of 10 cm [94]. In addition, also temperature and humidity sensors are present. Finally, a metallic dome-like structure glued on the sphere dissipates the heat generated by the electronics transferring it to the sea water via the glass.

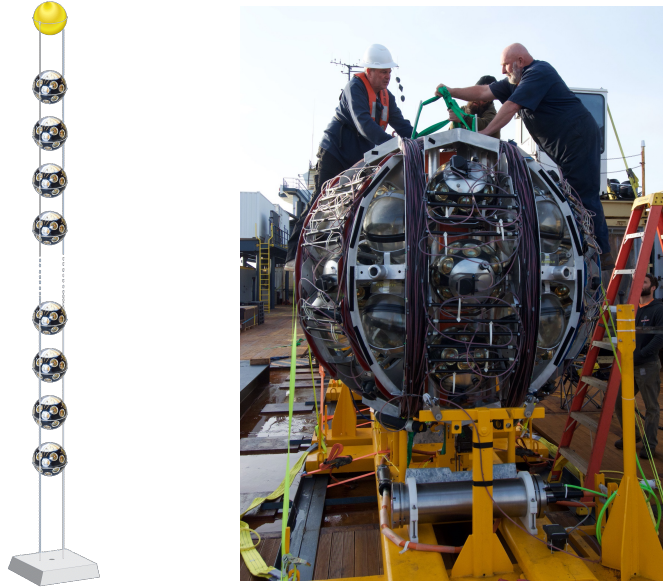


Figure 2.12: **Left:** Schematic view of a Detection Unit with 18 DOMs and buoy on top. **Right:** Photograph of the launcher vehicle (LOM) containing a DU during sea operations. The anchor and the Base Module (the cylinder at the base) can also be seen. Pictures taken from [47].

2.4.3 Detection Units

A Detection Unit is the vertical structure, anchored to seabed, which houses the DOMs. Each of them consists of a flexible string made of two ropes and contains 18 DOMs, with a vertical spacing of 36 m. Since the first DOM is placed at 100 m above sea bottom, the string reaches a length of about 750 m and is kept taut by a system of buoys, which also reduce the transversal displacement due to sea currents. The DOMs are connected to the DU's base, called Base Module, via a vertical electro-optical cable, a hose which runs along the ropes of the string and contains two copper wires for power transmission and 18 optical fibres for data transmission; these cables enter the DOMs through a penetrator located on the top of the spheres.

Power and data transmission to DUs is provided by interlink cables which connect the DU Base Modules to Junction Boxes (JB) laid on the seabed. Each of these boxes is connected to multiple DUs. Then, a main electro-optical cable (MEOC) connects the whole structure to the shore station almost 100 km away providing power and data transmission from sea to shore and viceversa. In order to reduce the number of fibres in the network running from shore to sea, KM3NeT implements a Dense Wavelength Division Multiplexing solution: by assigning to each DOM a dedicated wavelength for data transmission it is possible to transport signals from many different DOMs through a single fibre by multiplexing them. Once arrived to the shore station, these wavelengths are de-multiplexed and their association to the respective DOMs reconstructed. We will come back on this when talking about the data acquisition system of KM3NeT in the next chapter.

The design of the detector is based on the concept of building blocks. A building block is the smallest size detector, i. e. array of strings, with an optimal efficiency. The

latter depends on the number of strings, the number of DOMs along each string, the horizontal spacing between strings and the distance between DOMs along them. The optimization of the configuration has been studied with Monte Carlo simulations [28], considering the scientific goal of the experiment. Given the different aims, the optimal parameters are different for ARCA and ORCA: both of them have building blocks with 115 strings with 18 DOMs each, but while in ARCA the horizontal DU spacing is about 90 m and the inter-DOM spacing 36 m, in ORCA instead the DU spacing is 20 m and the distance between DOMs around 9 m.

For deploying the strings, an innovative technique has been developed which foresees the use of a submarine launch vehicle, called LOM (Launcher vehicle for Optical Modules). Inside the LOM (see Fig. 2.12), an entire rolled up string is contained [34]. The LOM is first lowered to the seabed to anchor the Base Module of the string. Then, it freely floats to the surface gradually unfurling the string. Finally, the vehicle is recovered and used for subsequent deployments.

Chapter 3

KM3NeT Trigger and Data Acquisition layout

The design of the KM3NeT Trigger and Data Acquisition architecture is based on the concept of modularity, which is also at the base of the off-shore detector itself. Its scalable architecture allows to collect data and process them in a progressive way as DUs are deployed, even if the detector is incomplete. No hardware trigger is implemented inside the DOM electronics and all detected optical signals, together with acoustic data required for the detector positioning system and other monitoring data, are transmitted to shore. This “all-data-to-shore” strategy reduces the complexity of the required electronics inside the optical modules but, on the other hand, it implies that the data throughput is completely dominated by the optical environmental background (see Sec. 2.3.1) with a rate of few tens of kHz per PMT and a throughput which ranges from 20 Gbps to hundreds of Gbps, according to the number of DUs. In the final configuration, a maximum data traffic of 500 Gbps from ARCA is expected, if we consider the most conservative scenario that foresees rates higher than 20 kHz per PMT. Considering a more relaxed scenario, a total throughput of about 100 Gbps is expected from ARCA, and of 50 Gbps from ORCA. As a consequence, essential requirements are: a fast and high-performance on-shore online trigger algorithm, fundamental for filtering data (both optical and acoustic) and cutting down the overwhelming background by looking for correlations among photon hit signals, and an expandable on-shore DAQ infrastructure able to cope with an increasing data-rate. In the following, the Trigger and Data Acquisition System network infrastructure and computing resources for the first phase of KM3NeT (involving the so-called “Broadcast” scenario) and its future evolution towards a “full White Rabbit” scenario are briefly described, together with the developed applications for handling and processing data.

3.1 Data acquisition network

The KM3NeT global Data Acquisition (DAQ) networking infrastructure is formed by 3 main subnetworks (see Fig. 3.2):

- Raw data network (RAW-LAN): comprises and connects the off-shore detector elements (DOMs and Base Modules), the on-shore computing resources dedicated

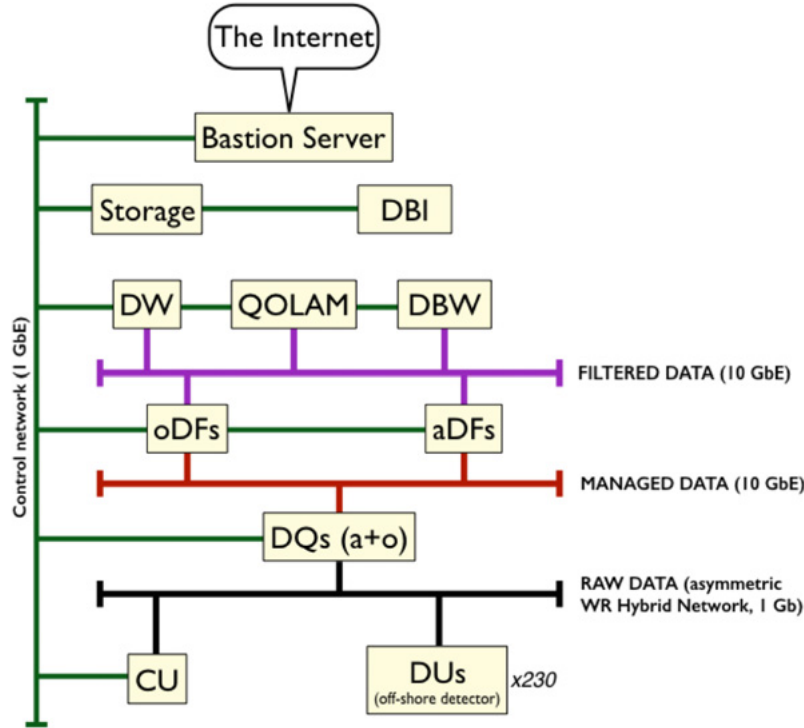


Figure 3.1: Scheme of the network topology implemented in KM3NeT. Figure taken from [80].

to data aggregation and distribution (optical and acoustic DataQueues), and the Control Unit;

- Managed data network: connects the DataQueues with the computing resources dedicated to data filtering (optical and acoustic DataFilters);
- Filtered data network: connects DataFilters with the infrastructure dedicated to analysis and writing of post-trigger data (DataWriter, Quasi On-Line Analysis and Monitoring (QUOLAM), DataBaseWriter).

Moreover, a Control network (CTL-LAN) connects all the shore-station computing elements with the ControlUnit and provides access to the Internet through a Bastion Server, which protects the internal networks.

The RAW-LAN architecture which has been chosen for the first 32 Detection Units of KM3NeT is an asymmetric hybrid LAN which exploits 10 Gbps and 40 Gbps optical Ethernet links in the shore-station for routing the incoming traffic from the detector to the computing farm, and 1 Gbps Ethernet links to implement connections between the detector elements (DOMs and Base Modules) and the shore-station. Data streams flowing out from detector elements are formed by the so-called *fast acquisition data* (FAD) and by the traffic due to data of monitoring instrumentation and to the replies to *Slow Control* (SC) commands, which are the commands given by the Control Unit for operating the DOMs, as described in Sec. 3.1.1. The FAD component contains the digitized optical signals registered by the PMTs, the acoustic data samplings for the detector positioning, and a continuous stream of summary information sent by each

DOM. This payload represents the largest part of the data stream, whereas the load of the remaining part of the data stream (Slow Control replies and additional equipment data) is substantially negligible.

The asymmetry of the RAW-LAN network, which represents its peculiarity, lies in the fact that while each DOM has a unidirectional 1 Gbps uplink through which it delivers its data streams to the shore-station, the latter exploits only few 1 Gbps downlinks, split by dedicated split-points, to *broadcast* the Slow Control commands to all DOMs and steer them. This means that the “Broadcast” signal is shared by every single DOM and not only by the recipient one. Moreover, a White Rabbit Switch fabric [2] is used to achieve a sub-nanosecond time synchronization among the DOMs. The “Broadcast” strategy partially reduces the number of required optical fibres (and so the costs of communication resources), but it involves a specific customization, made by Seven Solutions Company [3], of the White Rabbit switches and of the communicating elements inside the DOMs, in order to adapt the Master-Slave relation between them.

The Managed and Filtered data networks are standard 10 Gbps Ethernet networks, while the Control network is a 1 Gbps Ethernet network.

3.1.1 Data acquisition processes

Processes running on servers in the shore-station computing farm can be divided in three groups, according to their tasks: the Trigger and Data Acquisition System, the Control Unit and the Monitoring system.

The Trigger and Data Acquisition System

The Trigger and Data Acquisition System (TriDAS) comprises the software applications dedicated to the read-out, aggregation and filtering of the FAD stream flowing out from the detector elements. All of its components are inter-connected within the RAW-LAN (see Fig. 3.2) and administered via the CTL-LAN. The latter is also exploited for routing selected data to local (or remote) storages and for publishing monitoring data on external facilities. As soon as data reach the shore-station, its aggregation is handled by DataQueue processes. Their topology is such that each DataQueue client receives data only from a certain sector of the detector, i. e. from a certain group of DOMs. Then, DataQueues gather incoming data according to their timestamps and deliver them to the next process in the chain, which is managed by DataFilter processes. DataFilters are meant to perform the online data filtering process, and they are divided into *Optical DataFilters* and *Acoustic DataFilters*; this step is described ahead in the next section.

At the end of the filtering process, selected data are routed to a DataWriter process which writes it on a local storage in a ROOT-based file. In addition, as already mentioned, the CTL-LAN is exploited by automatic processes in order to periodically transfer selected data also to permanent remote storage devices, located at INFN-CNAF and IN2P3.

Control Unit

The Control Unit (CU) [35] is the user interface to the detector and the computing resources and it is formed by a collection of software processes and a web-server. Through

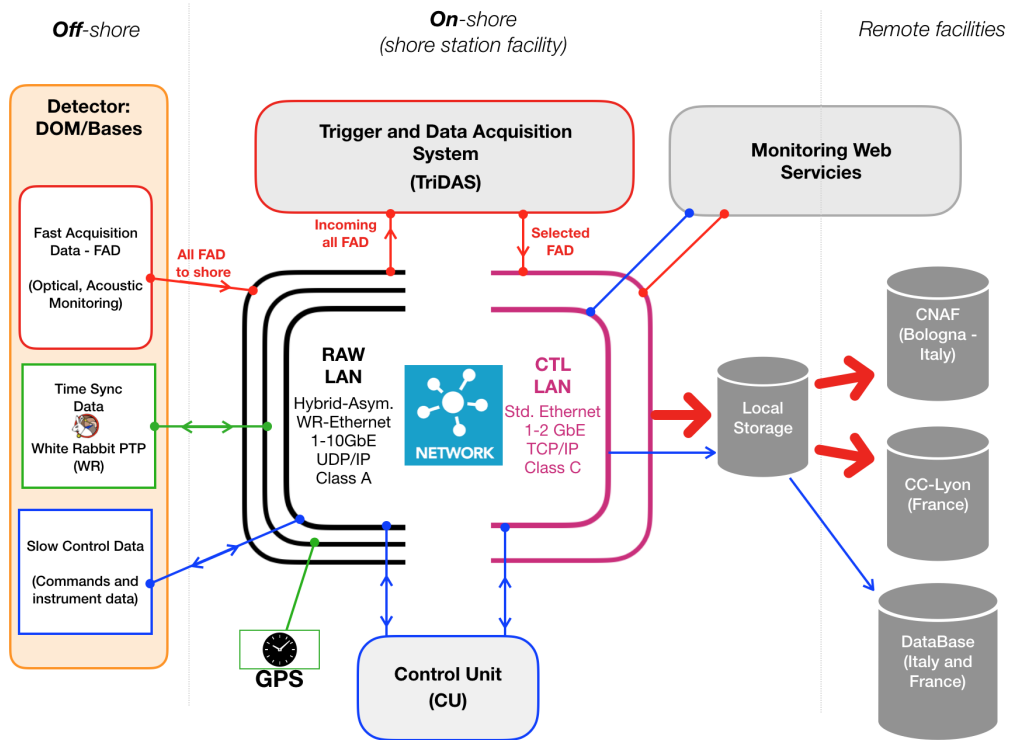


Figure 3.2: Outline of the DAQ infrastructure and components. Figure taken from [80].

the CU, users can start and stop data acquisition sessions, which are segmented into *runs* for which the desired configuration of DOMs and of the TriDAS can be set, composing the so-called *runsetups*. DOMs are operated via the dedicated state machine implemented into the CLB firmware, and the Control Unit commands the transitions between its states. The CU is also responsible for collecting and logging all the instrument and Slow Control data to the central database.

It is composed by the following sub-systems:

- Master Control Program (MCP): it is the main user interface and it allows users to schedule data taking;
- TriDAS Manager (TM): it allows the user to manage the computing resources, setting up the TriDAS processes;
- Detector Manager (DM): it controls and configure the off-shore detector elements;
- DataBaseInterface (DBI): it provides local database caching and synchronization with the remote database;
- DataBaseWriter (DBW): it collects instrument data, Slow Control data and Times of Arrival (TOAs) from the acoustic DataFilters, and writes it on the database.

Let us spend a few words in particular about the Detector Manager. The DM is deputed at steering each CLB and it is responsible for the transaction along the states of a finite state machine. The roles of the DM are the following:

- Configure the DOM input parameters (e. g. the PMT voltages) as specified by the user in the Master Control Program;
- Drive the CLB state machines towards the desired state;
- Read and register DOM output parameters, which will be written in a datalog file at the end of the run of data taking and eventually stored in the database by the DataBaseInterface.

To carry out its tasks, the DM sends and receives messages from all the CLBs of the detector. It communicates with them through the Slow Control protocol, which is built on UDP (User Datagram Protocol) sent on Ethernet and includes a layer called *Simple Re-transmission Protocol* (SRP) responsible for re-transmissions of packets by requiring an acknowledgment message for each sent packet. One of the jobs of the DM is to monitor the activity and status of the CLBs, and intervene and try to restore control on the ones who may possibly stop communicating, minimizing the need of human intervention. SRP allows point-to-point messages from the DM to each CLB and vice versa, as well as broadcast messages to all CLBs and transmission of data in subscription mode; thanks to the latter, the DM is able to request monitoring data from the CLBs just once and to receive them on a regular basis, with a tunable frequency.

Monitoring system

The Monitoring system is formed by a set of programs used to visualize, monitor and analyze a subsample of filtered data. It comprises also a web-server [57], accessible from the internet and constantly updated, used for live-monitoring the status of the data-taking, i. e. showing the PMT and trigger rates and the results of fast reconstruction and calibration checks. In addition, integrity checks on data are continuously performed by processes running in the background. It is composed by the following sub-systems:

- ROyWeb: web-based program which allows to plot monitoring data;
- Rainbow Alga: 3D event display;
- ROyFit: software for fast muon reconstruction.

DAQ processes and programs are not only exploited at the ARCA and ORCA shore-stations, but also in different other sites where the detector components are integrated and tested, as well as in test benches dedicated to DAQ and readout developments. A specific procedure, the Automatic Installation And Configuration procedurE (AIACE), was developed to take care of the installation and configuration of all the computing resources required according to a certain experimental setup [59].

3.2 Central Logic Board

The DOM Central Logic Board (CLB), shown in Fig. 3.3, is the main electronics board in the readout chain of KM3NeT. The PMT bases generate Low Voltage Differential Signals (LVDS) from the PMT electrical pulses. The corresponding Switch and Control Board (SCB) receives and distributes these signals to the CLB, where they are digitized

with a resolution of 1 ns by Time to Digital Converters (TDCs) running in the FPGA programmable logic. After being organized and time stamped in the CLB, TDC data are transferred to the onshore station for further processing and storage. The CLB board also houses the monitoring instrumentation: a compass/tiltmeter, three temperature sensors, and a humidity sensor. In addition, it provides a connection for a LED flasher (the *nanobeacon*) and for a piezo sensor. The control of the CLB is achieved by means of custom software, which runs in a LatticeMico32 (LM32) soft-processor operating in the programmable logic of the CLB FPGA. In the following, the hardware, firmware, and software of the CLB are briefly described.

3.2.1 Central Logic Board Hardware

The CLB printed circuit board (PCB) comprises 12 layers: six of them are dedicated to signals, two of them to power planes, while the remaining four layers are ground, which surround the power planes in order to reduce the electromagnetic interference from the power layers on the signal layers and to improve the signal integrity. The central coordinating component of the CLB is a Xilinx Kintex-7 FPGA, chosen for its relatively low power consumption. Other relevant components are the serial peripheral interface (SPI) flash memory, which can store up to four images of the FPGA and the configuration parameters of the CLB, and the programmable oscillators, which provide the appropriate clock signals needed by the White Rabbit protocol (see below) exploited by the CLBs for time synchronization and with nanosecond accuracy. The CLB board includes a 25-MHz crystal oscillator. The oscillator signal is first transferred from a clock pin to a buffer in the FPGA, and then fanned out to the inner phase locked loop (PLL) to provide two high frequency clocks of 250 MHz but with a 90-deg phase shift needed by the TDC core. The main component used for the communications with the onshore station is the small form-factor pluggable (SFP) transceiver, which interfaces the electronics with the optics system.

The CLB is powered via a *Power Board* (PB), in Fig. 3.3, that provides power to the CLB and to the entire DOM. The Power Board input voltage is 12 V, which is used to generate other six different output voltages: the 1 V, 1.8 V, 2.5 V and 3.3 V voltages are used for powering the FPGA, another one of 3.3 V for the PMT bases and a 5 V voltage for the acoustic piezo. The CLB has undertaken an evolution from the version 2.2.1, exploited in the first phase of the experiment, to the latest version 4, optimized and more performing than the previous version [44]. The main modification in the new CLB version is the improvement of the clocks routing. Also, new oscillator models were chosen to guarantee a better phase noise and stability to improve the White Rabbit (WR) synchronization (see Sec.3.4). New calibration devices were also included in the new design of the CLB, as well as a new model of bidirectional optical transceiver provided by Glenair [4] which ensures a higher reliability than the old transceiver model. The CLB v4 will be used for equipping the next phases of the KM3NeT experiment.

3.2.2 Central Logic Board Firmware

The readout logic of the DOM runs in the programmable fabric of the FPGA. A block diagram of the readout logic is shown in Fig. 3.5. Its main blocks are

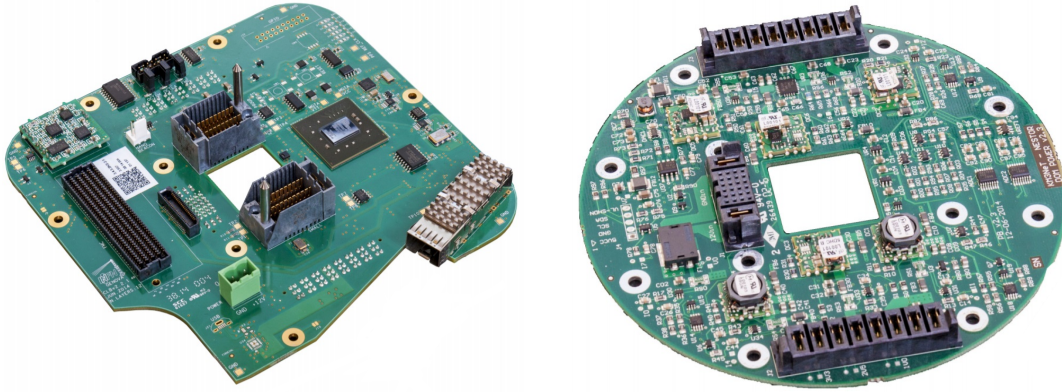


Figure 3.3: Pictures of a Central Logic Board (**Left**) and of a Power Board (**Right**). Figures taken from [44].

- A LatticeMico32 (LM32) processor, running the control and monitoring software for the CLB;
- The White Rabbit Precision Time Protocol Core (WRPC), which implements the White Rabbit protocol (see Sec. 3.4.2);
- The TDC module, which implements the TDCs for digitizing and time-stamping the PMT signals arriving to the CLB;
- The acoustic module, which implements a standard receiver for the read-out of acoustic data from the hydrophone;
- The monitoring module, for handling monitoring information from sensors (compass, temperature, etc.);
- The State Machine which gather TDC, acoustic and monitoring data, frames them inside specific timeframes and wrap them inside UDP packets;
- The IPMux cores, whose task is to dispatch the UDP packets over Ethernet to shore.

Firmware images are located in the SPI Flash accessible by the FPGA, which can contain up to four configuration images. On power up, the FPGA automatically loads the first image, which by convention must be the *golden* image. This contains minimal hardware initialization, and starts the *run-time* image after a 30 seconds delay. The role of the golden image is then to allow reprogramming of the FPGA in case the run-time image is damaged. The run-time image on the other hand implements the actual application logic. This two-stage start-up prevents the CLB from being bricked in case non-essential hardware fails.

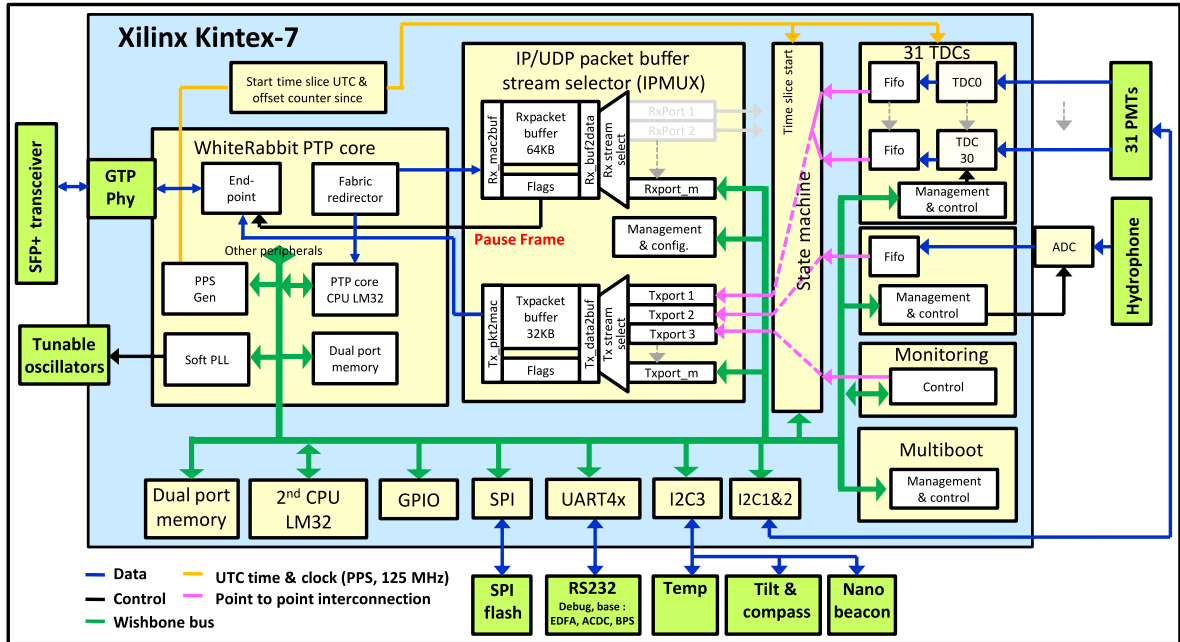


Figure 3.4: Block diagram of the embedded Central Logic Board FPGA firmware. Figure taken from [32].

The White Rabbit Precision Time Protocol Core

The WRPC is an enhanced Ethernet media access controller (MAC), embedded in the CLB FPGA programmable logic. Apart from transferring data as a regular Ethernet MAC does, the WR protocol synchronizes all CLB clocks in the detector. The protocol is based on the synchronous Ethernet (SyncE) and Precision Time Protocol [2] standards. The WRPC synchronizes the CLB through the same optical link that is used for data transmission. The global time of the network is provided by the WR master switch located onshore, which is synchronized to a global positioning system receiver. The WRPC IP core synchronizes with the WR master switch and provides a register with the coordinated universal time (UTC), which is used by the rest of the CLB firmware. It also outputs a pulse per second (PPS) signal, whose rising edge occurs precisely at the second transition of the global CLB UTC.

State Machine

The data acquisition is organized in consecutive frames with a period of typically 100 ms, called *timeslices*. The state machine core orchestrates the data acquisition for the CLB. First, it is responsible for generating the periodic start of the timeslice signal. This signal is synchronized to the start of a UTC second and repeats at the start of every period. All data acquiring IP cores synchronize their acquisition to this start timeslice signal, and all acquired data are sectioned and time-stamped relative to it. Second, the state machine is responsible for gathering the acquired data and merging the UTC time of the timeslice start signal, called the super time, to the acquired data time. By combining the relative timeslice time and the super time, the UTC time for all acquired data can be resolved by the onshore data acquisition system. Once acquired data are ready, the

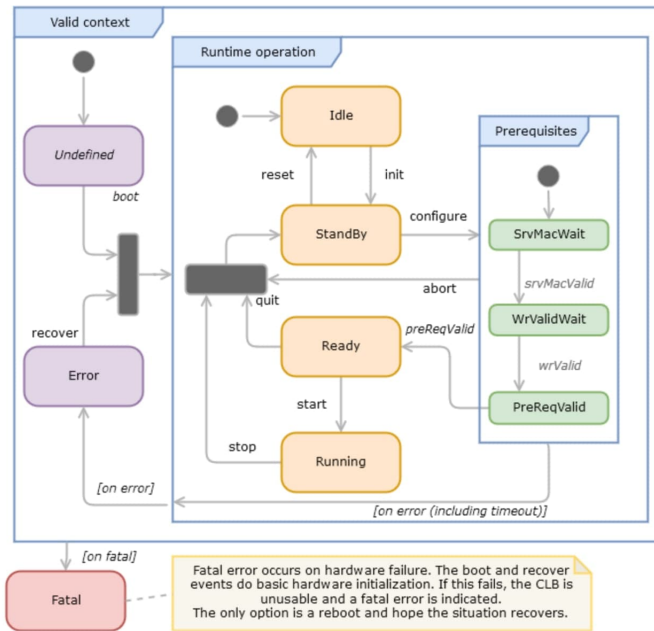


Figure 3.5: Internal states of the state machine and events (represented by arrows). Text in italics indicates autonomously issued events, while plain text indicates events issued by the user.

last responsibility of the state machine is to package it to be dispatched toward the User Datagram Protocol packet generator (IPMux). Data are portioned into frames such that they will fit within the payload of a UDP jumbo packet, i. e. up to 9014 bytes. A frame header containing metadata, such as the stream identifier or the run number, is also prepared.

The state machine is also responsible for implementing the main operations on the software. The operations are performed issuing *events*, which allow the transitions between states of the machine (Fig. 3.5). Each event causes specific actions to be performed and functions to be executed, as for example configuring process variables (e. g. PMT thresholds, High-Rate Veto, etc.). The CLB *First Generation* firmware includes a state machine whose operations were grouped into *subsystems*. A subsystem is a unit of code responsible for a specific logical part of the CLB operation; subsystems and related tasks are:

- System: it is related to general tasks and not specific to other subsystems;
- Optics: it is related to the control of PMTs and TDCs;
- Acoustics: it is related to the control of the hydrophone and the handling of acoustic data;
- Instrumentation: it is related to the monitoring sensors readout (temperature, humidity, etc.);
- Networking: it is related to the IPMux control and White Rabbit MAC address monitoring;

- Base: it is related to specific tasks relevant only for DU Base Modules.

A subsystem indirectly drives hardware related to its function; they are strictly connected to the state machine and act only upon state machine events. Events are usually issued by the user and driven by the Control Unit (as explained in Sec. 3.1.1) via the Slow Control protocol, but some events are autonomously issued by the software, such as when an error occurs.

3.3 Data handling

As soon as a photon hits a PMT, its optical signal is digitized in a LVDS signal which stays high as long as the electrical pulse is above a selected threshold set by the user on-shore via the Master Control Program. The arrival time and the Time over Threshold (ToT) of the signals on the 31 PMTs of a DOM are obtained with nanosecond accuracy by 31 TDCs implemented in the CLB FPGA. An additional TDC is used to timestamp the acoustic data, detected by the digital acoustic piezo hydrophone which samples at 193.5 kHz. The integrated electric charge over the threshold of the optical signals is also registered. These data fill first-in-first-out buffers, monitored in order to avoid overflows in case of excessive rates. For this reason, in standard data-taking condition, a *High-Rate Veto* of 20 kHz is set.

Then, optical and acoustic signals are organized into respective time frames lasting 100 ms, encoded as UDP/IP packets and subsequently sent to shore via the optical Ethernet fibers. In those frames, data packets are preceded by a header which contains the absolute timestamp of the frame. After the header, optical data frames contain the photon hits UDP packets formed by 6 bytes: 1 byte for the PMT channel, 1 for the hit pulse-duration and 4 bytes for the hit time with respect to the header timestamp. Acoustic data frames instead consist in digitized wave-forms encoded in UDP packets. The timestamps marked in the frame header result from the WR-PTP, an enforced PTP protocol with WR features implemented in the FPGA.

3.3.1 Optical and acoustic data channels

For optical data frames, DataQueue processes (see for reference Fig. 3.6) assemble frames coming from several DOMs and send over to each *Optical DataFilters* all frames belonging to a same specific time period. Thus, every Optical DataFilter collect all frames related to the same time period, and combine them to create *timeslices* of 100 ms. Then, the DataFilter process applies the trigger algorithm to the data: if a timeslice starts a trigger, all hits contained in it, plus all hits occurred in the detector between 10 microseconds before and after those hits, are collected in a *DAQ Event* and sent to the JLigier process. The latter is deputed to handle information coming from Optical DataFilters and to distribute it to a number of clients; in this sense, the JLigier is a dispatcher client that connects different processes according to a “many (m) to many (n)” $m : n$ protocol over Ethernet. Thus, the JLigier can dispatch the same information to multiple destinations, e.g. to the DataWriter process and to online or quasi-online analysis clients and applications.

When data arrive finally to the DataWriter process, this writes it down onto a file. Data are delivered by the JLigier according to a subscription principle: the subscription

Tag	Description
IO_TSL0	Information on all the hits exceeding the PMT's threshold, namely "L0" hits.
IO_TSL1	Information on two or more L0 coincident hits from different PMTs in the same DOM, within a fixed time window. These are referred to as "L1" hits.
IO_TSL2	Information on combination of L1 hits from different DOMs, exploiting the knowledge of the PMTs orientation inside DOMs itself and requiring specific patterns as defined by trigger algorithms. These are referred to as "L2" hits.
IO_EVT	Information on hits associated to reconstructed track-like or shower-like events.
IO_MONIT	Information on monitoring data plus some summary information on parameters characterizing the TimeSlice.

Table 3.1: Some of the tags assigned by the JLigier process to specific data streams, along with a brief description. L0, L1 and L2 refers to the three implemented levels of trigger.

consists in a list of tags, where each tag is a string related to specific data. Some examples of tags are "IO_L0", which refers to all the hits in a given timeslice, or "IO_EVT", which refers to all the hits associated to track-like or shower-like events as reconstructed by the reconstruction algorithms. A non-exhaustive summary of the tags exploited by the JLigier process is shown in Fig. 3.1.

Hence, programs which retrieve data from the JLigier can select the desired data by specifying the proper tag. Finally, the JLigier, as well as the DataFilters, exploits the Transmission Control Protocol (TCP) for data transmission, and therefore a conversion from the UDP to the TCP is needed: this is done by the DataQueue process. The channel just described that represents the stream into which optical data flow is referred to as the TTDC channel, and it is outlined in Fig. 3.6.

Acting on the acoustic data stream sent to shore (called TAES) are the *Acoustic DataFilters*. Such processes, one per DataQueue, collect the acoustic data produced by the sector of DOMs connected to the proper DataQueue. Their job is to compare with and correlate the incoming acoustic data stream to a set of prefixed waveforms, this way identifying the waves emitted by the pingers laid on the seabed around the detector and determining the ping Time of Arrival (TOA). The TOAs are then transferred to the central DataBase service for further processing. Indeed, starting from the ping identities and the related TOAs, dedicated algorithms can perform triangulations and determine the position of each DOM with the precision of $O(10)$ cm.

3.3.2 Monitoring data channel

Beside the TTDC and TAES channels, another channel reserved for monitoring information exists, called TMCH channel. Also in this case, monitoring data are sent to

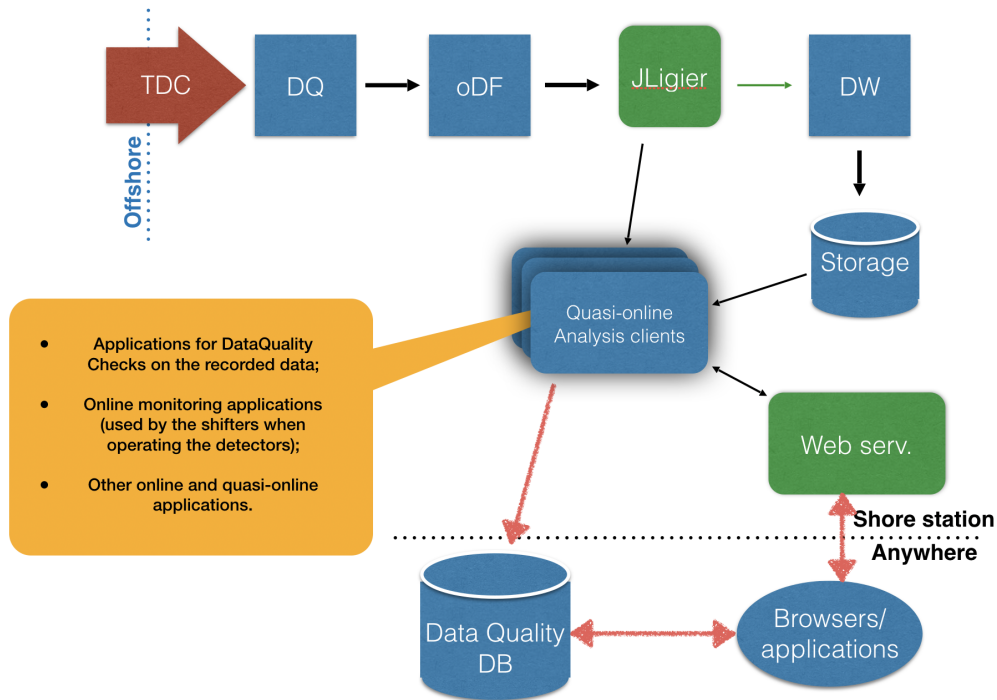


Figure 3.6: TTDC channel: optical data in form of UDP packets pass through the DataQueue, the optical DataFilters and to the JLigier, which dispatches it to the Quasi Online Analysis (QUOLAM) clients and to the DataWriter for being finally written on disk.

shore in UDP packets by DOMs and Base Module CLBs. Each monitoring packet is produced after the completion of each timeslice; it contains a summary of the most relevant parameters describing the status of the DOM or Base Module, i. e. :

- The Run number;
- The DOM identifier;
- The timeslice starting time;
- Yaw, pitch and roll as measured by the AHRS (Attitude and Heading Reference System) sensors;
- The three components x,y,z of the acceleration provided by the accelerometer;
- The three components x,y,z of the gyroscope rotation provided by the gyroscope;
- The three orientation coordinates x,y,z provided by the compass;
- The temperature and humidity values;
- Summary information, such as the TDC Hit counter values and the status of the High-Rate Veto for the PMTs.

On the shore station, one *Monrouter* (Monitoring router) process per sector is continuously receiving the TMCH data stream. Each Monrouter converts each UDP packet to TCP, assign it a “IO_MONIT” tag and send it to a JIlgier, in order to be properly dispatched.

3.4 Time synchronization and network implementation

The angular resolution on track reconstruction in a neutrino telescope depends on several factor, such as the precision on PMT position and the time synchronization precision. Taking into account that muon tracks in the detector can be as long as ~ 1 km, and considering the Cherenkov photon velocity in water, calculations show that a time synchronization precision of the order of the nanosecond is required in order to achieve a resolution on the track angle of the order of $\sim 0.1^\circ$. As already mentioned, the time synchronization of the off-shore detector is achieved by means of the White Rabbit technology. The same Ethernet network infrastructure is in fact exploited both for timing and data distribution. This choice puts strong constraints on the network itself and also on the technology to build DOMs and Base Modules. The implementation of this network has undergone a major design change, starting from a customized White Rabbit technology, which goes by the name of “Broadcast” scenario to the new “full White Rabbit” approach. Before discussing in detail about the latter, being the focus of this thesis, let us review quickly both for a necessary comparison.

3.4.1 “Broadcast” scenario

The custom White Rabbit implementation adopted for the first 32 Detection Unit configuration of the KM3NeT experiment relies on a highly asymmetric network, leveraging on the concept of the single broadcast line for the communication from the shore station to the detector. The term “Broadcast” is motivated by the fact that the data leaving the shore station are mirrored at the detector by passive splitting stages so to be routed to all the DOMs and Base Modules. In practice, any part of the telescope receives the same information from the shore, filtering and processing the sole messages addressed to it. In the standard White Rabbit implementation, a point-to-point connection is established between a WhiteRabbit-Master, generally a White Rabbit switch (WRS) connected to the GPS, and the end-point to be synchronized, which is in Slave mode. Both devices mutually exchange White Rabbit Precision Time Protocol packets for the time synchronization. In the “Broadcast” context instead, the on-shore master functionalities are split into two different WRSs, the WRS-Broadcast and the WRS-Level1, which share the mastership to the off-shore endpoints. The latest customization of the WR for KM3NeT relies on the WRS v4.2. In order to properly interface the off-shore detector to the computing resource in the shore station, where the Control Unit and the TriDAS are running, a dedicated switch infrastructure has been designed (see for reference Fig. 3.7) composed as the following:

- Sets of one WRS-Broadcast plus a number of WRS-Level1 compliant to the number of Base Modules. For every detector sector, a said set of switches is present (see Fig. 3.7);

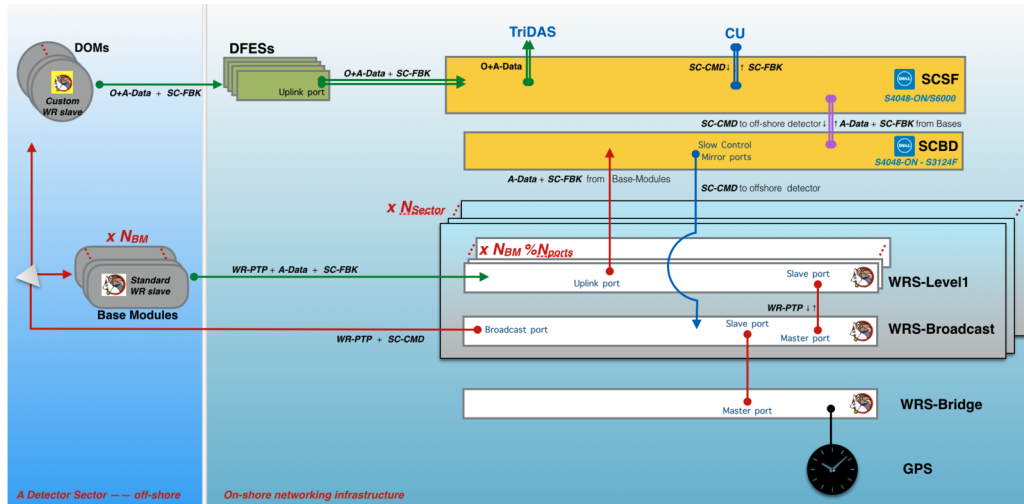


Figure 3.7: Layout of the “Broadcast” networking system. Single (double) lines represent 1 GbE (10 GbE) connections. Single directional data-flows are indicated with arrows, while bidirectional connections have only dots. Figure taken from [46].

- A sufficient number of standard DOM *Front End Switches* (DFES) for hosting the total number of DOMs;
- A *Star Centre Switch Fabric* (SCSF) element to route the optical and acoustic data streams to the TriDAS computing resources;
- A *Slow Control and Base Data* (SCBD) element to connect the standard switch fabric with the White Rabbit one.

In order to preserve the stability of the WR infrastructure and reliability of the time synchronization mechanism, it was mandatory to minimize the traffic passing through the WRS-Broadcast. This has been achieved exploiting the Software Defined Networks (SDN) technology on the switches [46]. In KM3NeT, SDN switches are cleared from any standard switching feature (such as the automatic learning) and implement few dedicated routing rules which can control in a deterministic way the data traffic through such an asymmetric network.

3.4.2 “Full White Rabbit” scenario

The “Broadcast” scenario is applicable only with a small detector and it does not allow the telescope to scale up to the target hundreds of strings and thousands of DOMs. In fact, in this approach each DOM has its own dedicated channel to shore, carried along the optical fibres in the multi-km long main electrical-optical cables (MEOC). However, only a limited number of MEOCs was affordable, with a not sufficient number of optical fibres to supply all the needed channels. For this reason another approach was considered, the so called “Full White Rabbit scenario”. It relies on uplinking to shore the data stream of the DOMs in a DU by means of WRSs located in the Base Module. The actual design foresees two standard WRS per Base Module as depicted in Fig. 3.8. These are referred to as *Wet* WRS (WWRS), as opposed to the *Dry* WRS (DWRS) which is located on-shore. Traffic from DOMs (data and Slow Control replies) of the DU will hence be routed

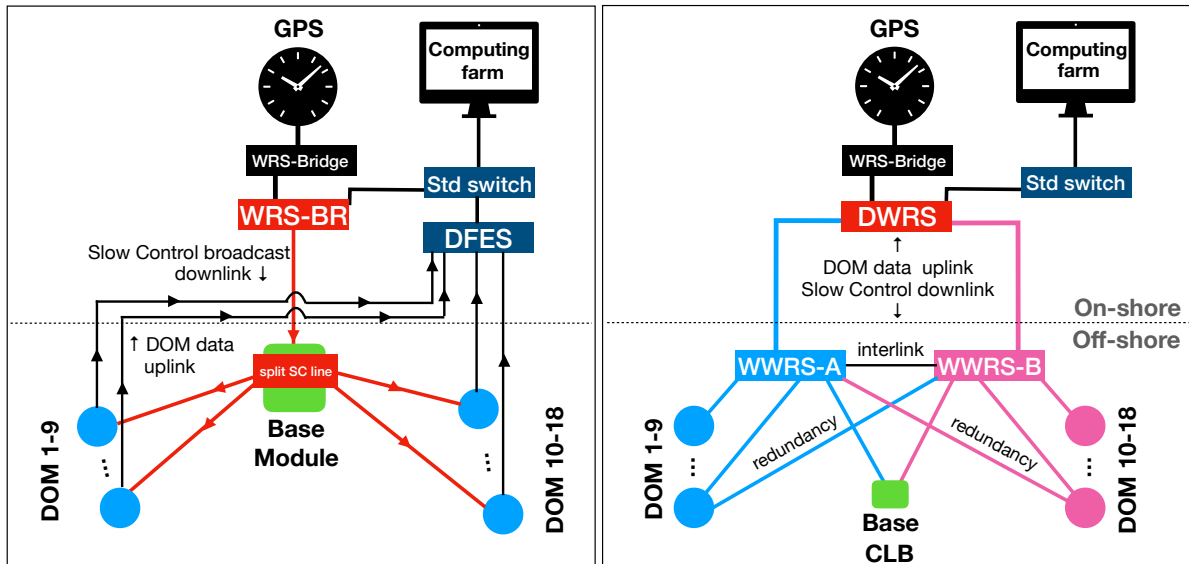


Figure 3.8: **Left:** Sketch of the “Broadcast” network architecture. The broadcast signal (red arrows) provided by the WRS-Broadcast (WRS-BR) is split and shared among all the DOMs. The GPS timing is transmitted by the WRS-Bridge to the WRS-BR and through the broadcast signal to the DOMs, together with Slow Control commands. DOM data instead are transmitted via unidirectional fibres towards the DOMs Front End Switch (DFES) which is connected through a standard switch to the computing farm. **Right:** Sketch of the “full WR” network architecture. In this configuration two *Wet* WR switches (WWRS) are located inside the Base Module of the DU. Both SC messages and DOM data pass only through the two shore links connected to the WWRS. The Base Module and 12 other DOM links are made redundant via a splitter. In addition, an interlink connects the two WWRS and routes the traffic from one switch to the other in case a switch shore link is lost.

through the two bidirectional fibres which connect the WWRS to the DWRS, instead of having one fibre per each DOM running from the detector to the shore station. This way, thanks to the aggregation provided by the switches, a reduction of a factor 10 in the number of fibres is obtained: from 20 connections in the “Broadcast” scenario (broadcast downlink + 19 DOM and Base Module uplinks) to 2 connections (2 WWRS bidirectional links to on-shore).

The design and validation of such a system concerns several of the subsystems of KM3NeT. In particular:

- The electronics: a special focus is put on developing the hardware needed to operate KM3NeT detectors in a standard WR network and assessing its reliability;
- The optical system: a development of a new optical network topology between the DOMs and the Base Module and between the DU and the shore station is required;
- The power system: measurements of the power consumption of the new electronics are needed, estimating the additional power required to implement the standard WRS and verifying that it is compliant with the power that can be delivered off-shore in the two detectors of KM3NeT;

- The DAQ and the readout: the re-design of the DAQ elements must be done, especially regarding the Base Modules. The definition of the network topology and validation of the robustness and reliability of the data transfer and time synchronization of the new architecture are required, as well as the definition and design of the level of redundancy and fail-over procedures which are needed in case of link interruptions;
- The calibration: the calibration and synchronization plan, to be performed in the final validation, must be defined.

The collaboration has performed a proof of concept to the above-mentioned designed architecture exploiting the existing equipment, that is CLBs v2.2.1 and standard rack WRS. The tests which have been conducted shed light on the feasibility of the system, but also emphasized the limitations on the current equipment. As a result of this, new developments have been carried out. The CLB has been revised and the previous version has evolved into the CLB v4, as well as its Power Board. Moreover, the Base Module design has been engineered in order to take into account the required changes due to the introduction of the WRSs; the mechanics of the concept, as well as the power system and the implementation of the optical routing scheme have been evaluated. As stated before, the new architecture involves the deployment of two standard WRSs inside the Base Module. For this purpose, customized WRSs have been designed that preserve the standard WRS functionalities but have a form factor specifically tailored for respecting mechanical limits of the new Base Modules. Furthermore, the CLB firmware has been also revised and a new version called *Next Generation* firmware has been developed (see Sec. 3.4.3). This includes the latest version of WRPC as released by CERN. The use of the standard WRPC will allow the simple update of the core with a plug-and-play approach and without the need of specific customizations, in contrast to what happens for the “Broadcast” scenario. This solution not only will ease the debugging and maintenance tasks but will also reduce the number of issues.

For the appropriate definition of the network topology at both the shore-station and the fabric, in the DU Base Module, an effective estimation of the data rates is also needed. The relevant data streams involved in the DAQ concern the optical and acoustic data. Both of them are monodirectional, from the offshore detector to the shore station. The Slow Control data, although bidirectional, are limited (about 3 kbps/DU downstream and 1 Mbps/DU up-stream). The optical data stream is mainly due to the optical background caused by ^{40}K decays and bioluminescence contributions (see Sec. 2.3). The latter can induce variable increments of the single rate per PMT. For this reason, two scenarios have been considered by the collaboration for the PMT single rates: realistic (7 kHz/3”PMT) and conservative (15 kHz/3”PMT). Given that the payload of a UDP packet containing a digitized optical signal is 6 Byte, and taking into account the acoustic data which are around a 20% of the optical data, it can be concluded that one DU is conservatively expected to produce an overall throughput of 500 Mbps. In practice, one WRS would be capable to uplink the full DU data traffic, with a considerable safety margin. The long range optical communication protocol is based on 4 *colours* per DU (4 Wavelength Division Multiplexer channels spaced 100 GHz apart). The 4 colors are allocated to 2 uplink and 2 downlink channels. Each pair belongs to a WRS, being the main components of the system:

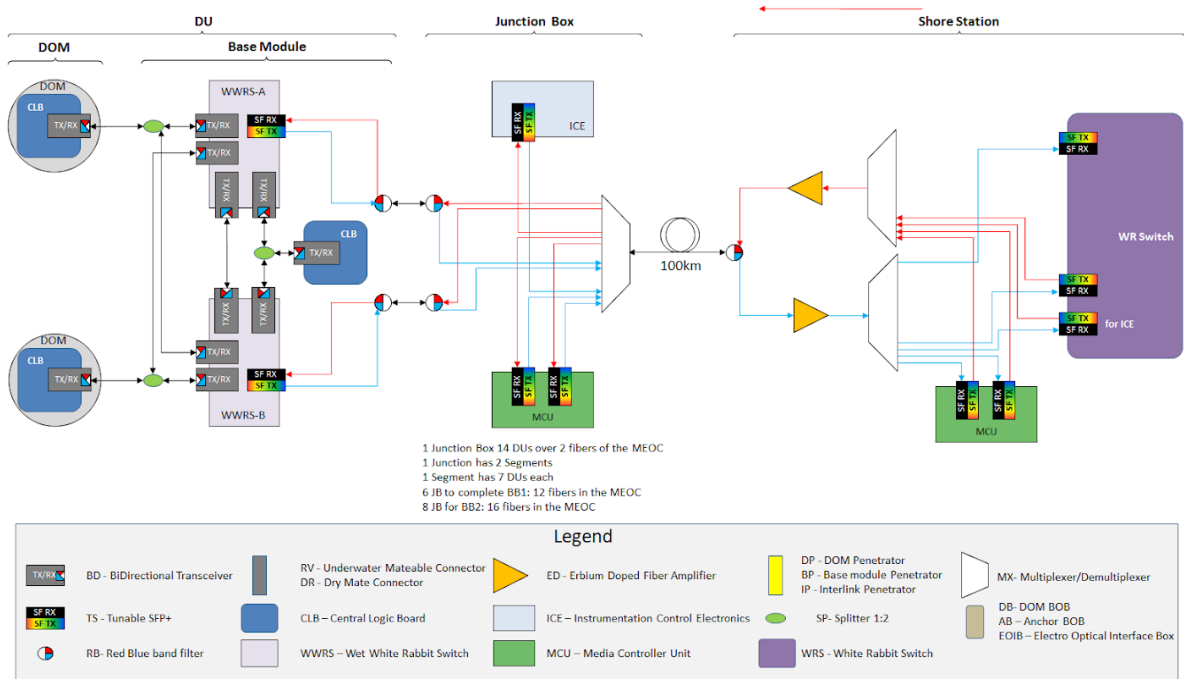


Figure 3.9: Network scheme of the Full White Rabbit topology, including redundancy. The particular case for ARCA is shown.

- 2 red/blue band optical filters (it applies only to the ARCA detector);
- 1 wide band multiplexers (it applies only to the ORCA detector);
- 2 tunable SFP plus Dense Wavelength Division Multiplexers long range transceivers for connecting with the on-shore station;
- 2 WRS per DU: 9 DOMs connected per WRS;
- 1 Base CLB connected to one of the two WRSs and redundant connection to the other;
- 17 bidirectional short range transceivers per WRS for DOM connections (3 direct + 12 redundant), Base CLB connection (1), inter-WRS connection (1).

There are several types of possible failure at the DU Base or in the fibres up to the node or the Junction Box (JB). One of them is the loss of the uplink due to a failure at the fibre (up to the node or JB) or at the uplink transceiver. The solution provided in KM3NeT is to redirect data from one WRS to the other one. The redundancy has been already implemented and several tests have been performed to validate it. A functional failure in one WRS is also foreseen. In order to overcome this problem an optical redundancy has been implemented, allowing the optical communication of a DOM with the two WRSs, being active only one of them. In the case of a WRS failure, it is possible to redirect the DOM communication from the failing WRS to the working WRS. The total number of ports on the current generation of WRS is 18, out of which one is reserved for the long range communication to shore. When the maximum redundancy is introduced then one port per WRS is assigned to the communication with the DU

Base CLB and one port per WRS is assigned to the intra-WRS connection. Therefore, six ports per WRS are used to connect DOMs in a redundant way. Thus, regarding the DOMs, the redundancy obtained is partial and only 12 DOMs will be connected in a redundant way to the WRSs in the DU Base. The redundancy proposed architecture is shown in Figure 3.9.

For what concerns transceivers, one of the main components of the system, a Glenair connectorized transceiver, with lower power consumption and higher reliability than the transceiver previously used in KM3NeT, has been chosen and is now implemented in the new version of the CLB and in the WRS backplane developed for KM3NeT.

3.4.3 Next Generation firmware

As stated above, the introduction of the Full White Rabbit required the development of a new firmware version for the CLBs. With respect to the First Generation firmware, the upgrade presents several differences. It has been in development and under constant review since the 2019, and it has been named *Next Generation* (NG) firmware. Let us briefly summarize its main architectural improvements with respect to the previous version. The main difference in the NG firmware lies in the state machine architecture, which has changed from the multiple subsystems concept to a monolithic state machine where all the different subsystems act as one during a state transition. In fact, the previous state machine required, for the correct and smooth functioning of the CLB, a specific order of transitions of the different subsystems. This order was not respected autonomously by the state machine upon event initialization, unless it was explicitly specified by the Control Unit. In order to overcome this problem, the concept of separated subsystems was dropped, so that in the NG firmware the state machine performs the required operations in the correct order, regardless of which subsystem they refer to. Then, of course, the support for both the “Broadcast” and “full White Rabbit” architectures has been implemented, including the integration of the latest release of the White Rabbit protocol whereas the previous firmware supported only the White Rabbit PTP up to version 2.1. In addition, the NG firmware is compatible with both CLBs v2 and v4.

Chapter 4

“Full White Rabbit” setup validation

The implementation of the “full White Rabbit” network architecture requires the design and the assessment of new technology. For this purpose, several laboratories throughout the whole collaboration are deputed to development, test and maintenance of the employed instrumentation. Among them, the Bologna Common Infrastructure (BCI) hosts a test bench which recreates a full detector string with all the electronic boards and the relative Data Acquisition System resources, implementing as a whole the “full White Rabbit” network topology. The validation of this setup, which was the main goal of my thesis, represents a focal point for the transition of the experiment towards the next phase. In particular, the conducted validation involved the time synchronization of the apparatus and the test of the integrity and stability of the optical and monitoring channels. In this chapter I will first report about the preliminary studies I have done on a first test bench for optimizing the ultimate setup for the validation process. I will discuss the analysis tools and the measurement strategies I have developed. Finally, I will show the results obtained with the validation setup.

4.1 The Bologna Common Infrastructure experimental setup

The Bologna Common Infrastructure (BCI) is a unique setup, over the whole KM3NeT collaboration, which puts in place all the data processing key-points due to a real implementation of the full DAQ chain inside a controlled environment. The BCI offers the incomparable opportunity to test any new development or upgrade of the DAQ-related hardware and software components before the final string deployment under the sea. At present, the BCI comprises two full DU-size test benches, each of them formed therefore by 18 CLBs acting as DOMs plus 1 CLB acting as the Base Module CLB, together with all the electronics and power supplies required for the correct functioning of the apparatus. One of the test benches implements the “Broadcast” network configuration, while the other (see Fig. 4.2) implements the “full White Rabbit” upgrade, as outlined in Fig. 3.8.

The main goal of my work at the BCI was focused on the validation of the “full WR” setup, so here I will pay particular attention on that test bench. When I started my activity at the BCI, the “full WR” test bench consisted in:

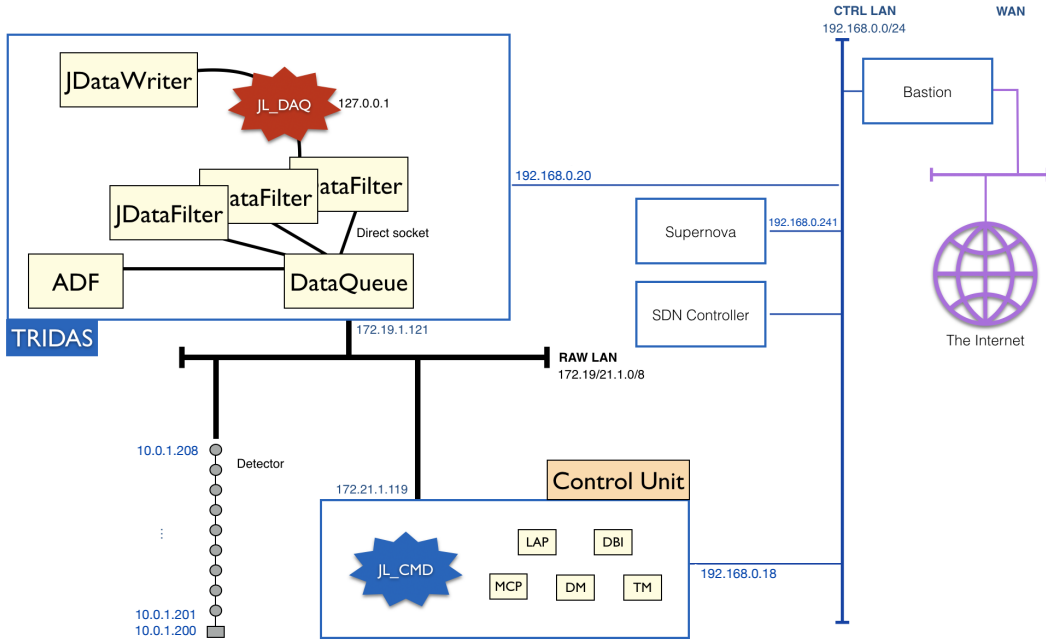


Figure 4.1: Layout of the “full WR” setup network topology at the BCI.

- 9 CLBs version 2.2.1 powered via PBs version 2 and implementing standard SFP transceivers;
- Two SCBs version 3.4 provided by the Seven Solution company;
- Two custom Chromium Backplanes-20SFP with standard SFP transceivers, provided by the Nikhef University.

The CLBs are independently powered by means of a ELC 12V-25A power supply. Since only the CLB boards are present, these act as DOMs without the outer casing, the pressure resistant glass sphere, the PMTs, their related PMT bases and the two electronic boards (called “Octopus” boards) used to connect the PMT bases to the CLB.

Upgraded configuration

After some preliminary measurements, illustrated in the next section, this setup was dismantled in order to leave room to a full-string reproduction including newly developed versions of the components. The latter, shown in Fig. 4.2, comprises the following items:

- 19 CLBs version 4 powered via PBs version 3 and implementing Glenair Bidi 057-0231-33-1G transceivers. 18 CLBs act as DOM CLBs, 1 as the Base Module CLB;
- Two SCBs version 3.4 provided by the Seven Solution company;
- Two Glenair backplanes version 2, implementing Glenair Bidi 057-0231-33(27)-1G transceivers and a standard SFP transceiver for connection with the shore facility (i. e. the DWRS);
- A splitter for implementing the redundancies;

4.1. THE BOLOGNA COMMON INFRASTRUCTURE EXPERIMENTAL SETUP73

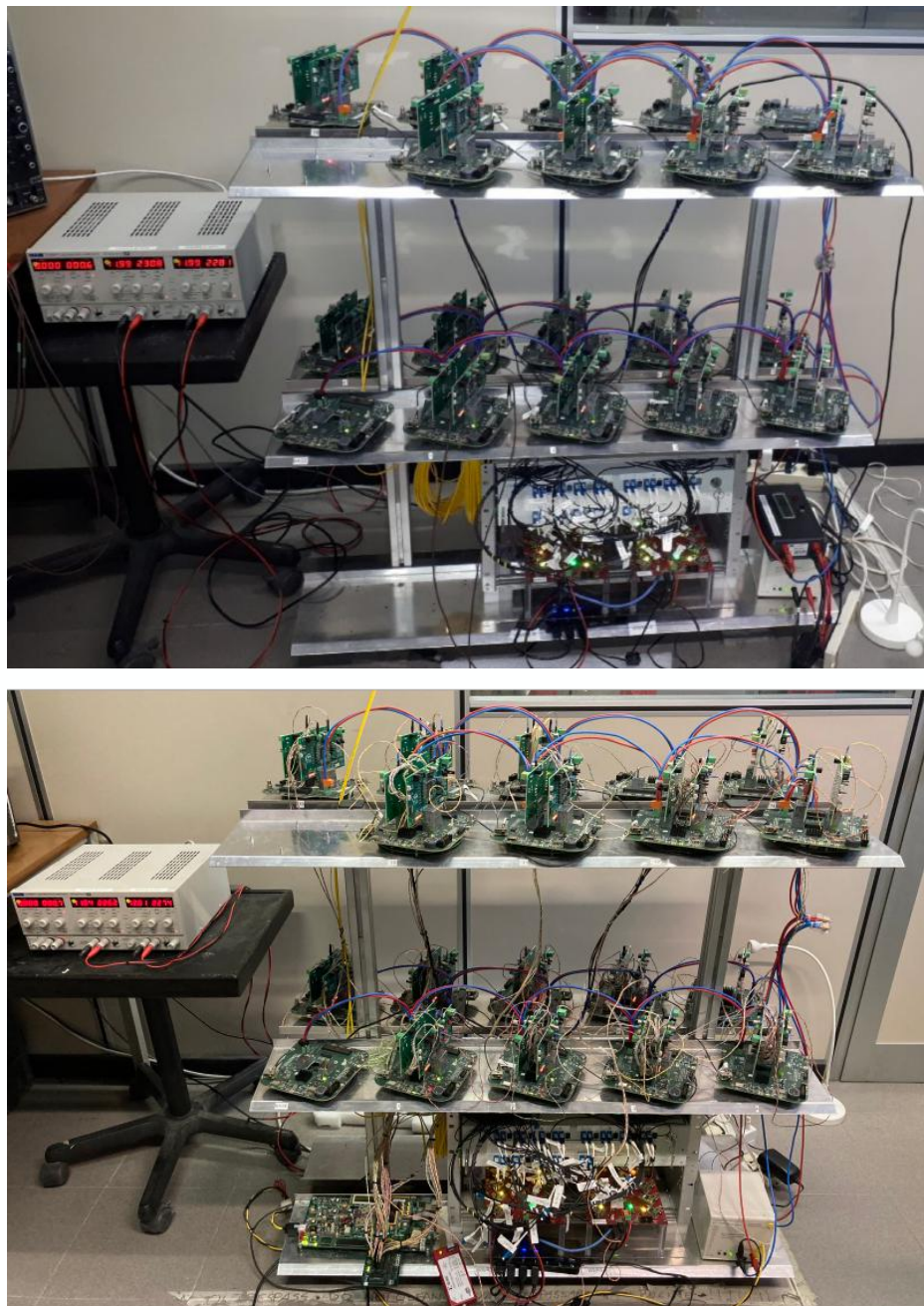


Figure 4.2: “Full WR” test bench at the BCI in its final configuration. It is formed by 19 CLBs, with OctoPAES boards plugged on, two Wet White Rabbit switches and the power supplies for the CLBs and the switches. **Up:** setup configuration with OctoPAES in stand alone mode, i. e. operating with their internal clock and with an independent start/stop signal generated by pressing a button on the boards. **Bottom:** setup configuration with the Kintex KC705 board providing a common start/stop signal to all the OctoPAES and acting as their clock source, with the clock signal distributed in daisy chain.

- Glenair optical fibres for connections between CLBs and WWRSs, and standard optical fibres for connections between WWRSs and the DWRS.

The presence of the PMTs and of the Octopus board is mocked by the integration of the OctoPAES boards. Each CLB can host two OctoPAES boards, able to emulate optical signals for the PMTs and also acoustic signals. Different PMT single-rates can be selected and customized hit patterns can be configured for each PMT, as described in Sec. 4.4.1.

In addition to the hardware parts which stand for the off-shore detector, the BCI implements also the effective elements of the network infrastructure, concerning both the submarine part and the one in the shore station. A schematic overview of the BCI connections between the DU and the shore station is depicted in Fig. 4.3. The BCI shore station facility for the “full WR” setup is composed by:

- 1 GPS;
- 2 White Rabbit Switches (a WRS-Bridge and a DWRS);
- 1 DELL S3124F which links up the DWRS with the CU and TriDAS servers.

The White Rabbit Switches ensure the required nanosecond time synchronization of the CLBs. The 10 MHz GPS receiver generates the master clock which is then provided to the DWRS through the WRS-Bridge. The DWRS sends the clock signal to the WWRSs which then distribute it to the connected CLBs. The clock is passed from master to slave embedded into WR-PTP packets. Its reconstruction is achieved by the slave thanks to dedicated hardware and firmware logics, including a dedicated PLL. When synchronized, each CLB is able to expose from a Lemo[®] connector the *Pulse Per Second* (PPS) signal, i. e. a repeated signal at 1 Hz. As described ahead in the text, I used such a PPS signal to perform synchronization checks between the CLB boards and a common reference. In this way, sub-nanosecond synchronizations can be achieved, allowing us to correlate in time the events detected by the various CLBs. In order to do so, each CLB marks the registered data with a timestamp before forwarding them on-shore in the way explained in the previous sections.

Finally, the BCI is equipped also with the necessary computing resources, described in Sec. 3.1.1 (see Fig. 4.1), accordingly to the shore station networking layout:

- A BCI Bastion server which serves as portal for the users and hosts the hypervisor of the virtual machines;
- A Control Unit server hosting the CU services;
- A DAQ server hosting DataQueue, JDataFilters, JDataWriter, JLigier processes, the Acoustic Data Filter and the CLBSwissKnife [5], a program which connects to the JLigier and collects “IO_MONIT” data for monitoring the status of the CLBs;
- A monitoring server called *Supernova* installed into a virtual machine on the Bastion server.

The equivalent ensemble of computing resources is present also for the “Broadcast” test bench, which includes its own Bastion server and all the other services.

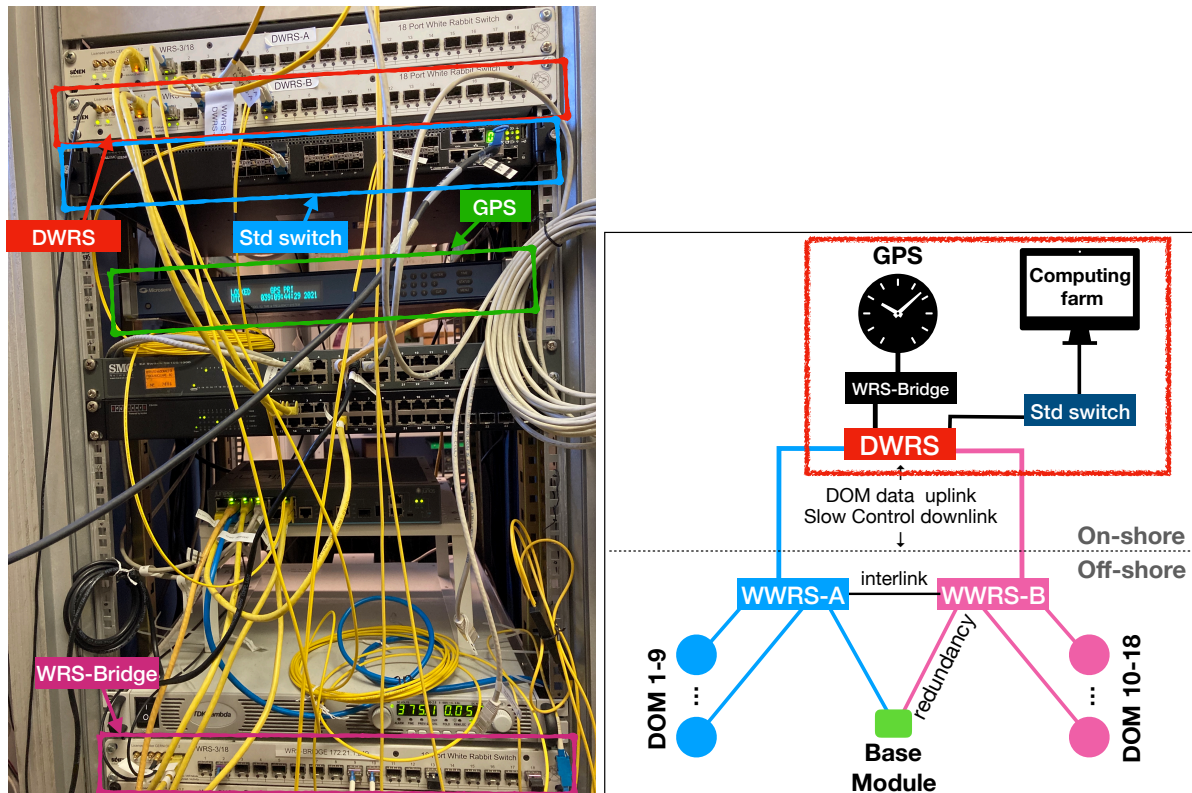


Figure 4.3: **Left:** The rack-mountable elements (standard DELL switch, Dry White Rabbit switch, GPS, power-supply). Those elements refer to the highlighted red box in the scheme (**Right**).

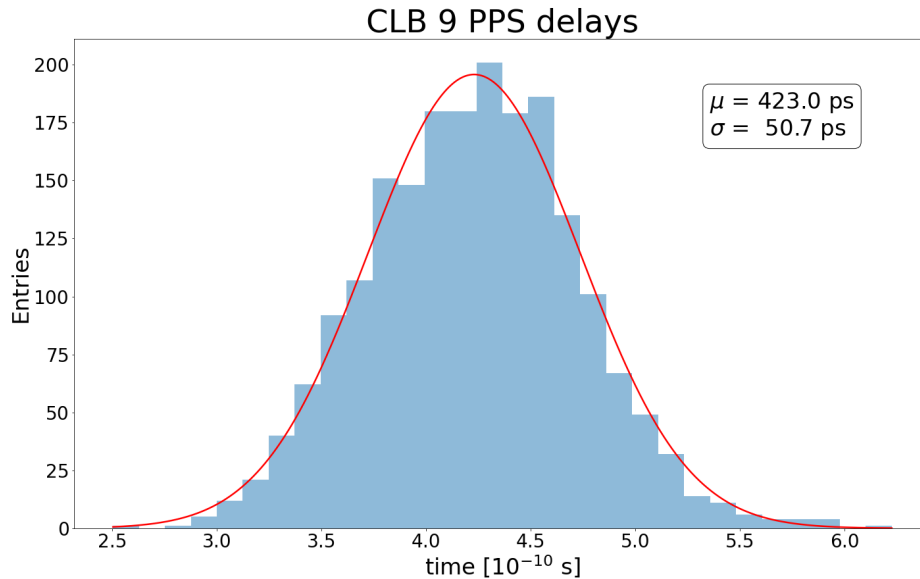


Figure 4.4: Oscilloscope fine measurement of the delays between the PPS signal of CLB-9 of the dismantled setup with respect to the signal of the reference CLB-1. The random delays fit with a Gaussian curve with mean and sigma as indicated in the adjacent box. The measurement comprises 2000 events, whereas the sampling frequency was set to 100 ps and the time range was equal to ± 50 ns. Delays follow a Gaussian distribution, whose fit curve is shown in red and whose mean and sigma values are written inside the box.

4.2 Pulse Per Second synchronization

The first preliminary test that I conducted was carried out on the first configuration of the “full WR” setup, that is the one described in Sec. 4.1. As part of the time synchronization validation, the Pulse Per Second signal was studied. The aim is to provide a clear statement that the time offset between the CLBs is much smaller than one nanosecond. The delay between the PPS signals produced by the CLBs is an optimal indicator of such offsets. I started this measurement with the preliminary “full WR” setup with 9 CLBs. I measured with an oscilloscope the time delay between the PPS signals of the nine CLBs acting as DOMs with respect to a reference one among them, which I chose to be the board numbered as CLB-1. Two different kind of measurement were made: a fine measurement with oscilloscope sampling frequency set to 100 ps and time range equal to ± 50 ns was made on only one CLB (namely CLB-9) in order to verify that the synchronization accuracy was better than the nanosecond; a coarse measurement instead, with sampling frequency set to 10 ns and time range equal to ± 50 ms, was made on all the CLBs in order to check for the presence of de-synchronizations larger than 10 ns. The reason behind this choice was that within the “Broadcast” network architecture it had occurred in the past that temporary de-synchronizations between CLBs of the order of the microsecond were observed. This issue was never again observed after a software upgrade of the WR switches and it was never observed during the validation test performed by the collaboration on the full standard White Rabbit implementation, yet a tentative test was done also on this setup. For the coarse measurements, the delay between the PPS waveforms was much smaller than the sampling frequency so that measures were biased by the poor resolution and jitter. However, eventual delays larger

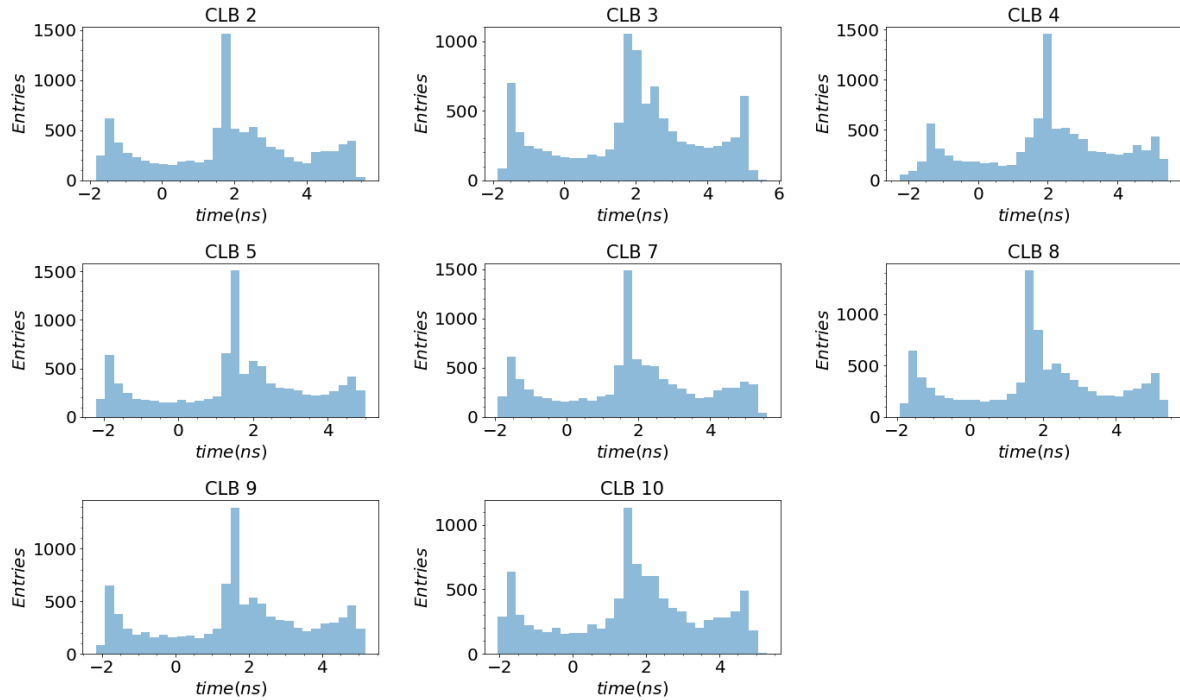


Figure 4.5: Oscilloscope coarse measurements of the delays between the PPS signal of the CLBs of the dismantled setup with respect to the signal of the reference CLB-1. Measurements comprise 10000 events, with sampling frequency set to 10 ns and time range equal to ± 50 ms. Distributions are completely biased by the poor resolution and by jitter, so that the only relevant information that can be extracted is the fact that all observed delays were smaller than 10 nanoseconds and no delays in the range 10 ns - 100 ms were observed.

than 10 ns would have been correctly detected: hence, the only relevant information that one can derive from those measurements is the potential occurrence of delays in the range between 10 ns and 100 ms. The fine measurement consisted in 2000 data points, while for the coarse ones 10000 points were taken. The fine measurement on the CLB can be seen in Fig. 4.4: the random delays follow a Gaussian distribution, whose fit curve is also shown in the figure. On the other hand, the complete set of coarse measurements is shown in Fig. 4.5 For what concerns the fine measurement on CLB-9, the observed synchronization accuracy was smaller than the nanosecond, as expected. For the coarse measurements instead, no delays in the range between 10 ns and 100 ms were observed, indicating the absence of microsecond out of synchronization issues.

These measures were useful for defining the technique for testing the PPS synchronization in the upgraded configuration of the setup which was built shortly after.

Just after the installation of the final configuration of the “full WR” test bench, I have replicated the test for validating the PPS sub-nanosecond time synchronization. Therefore, I measured with an oscilloscope the delay between the CLB PPS with respect to the reference one (CLB-1). The oscilloscope sampling frequency was set to 50 ps with time range equal to ± 25 ns, and 10000 data points were taken for each CLB. Again, measures fit with a Gaussian distribution as the delay values are randomic. The results of these measurements are shown in 4.7, whereas a magnification of such a plot is shown

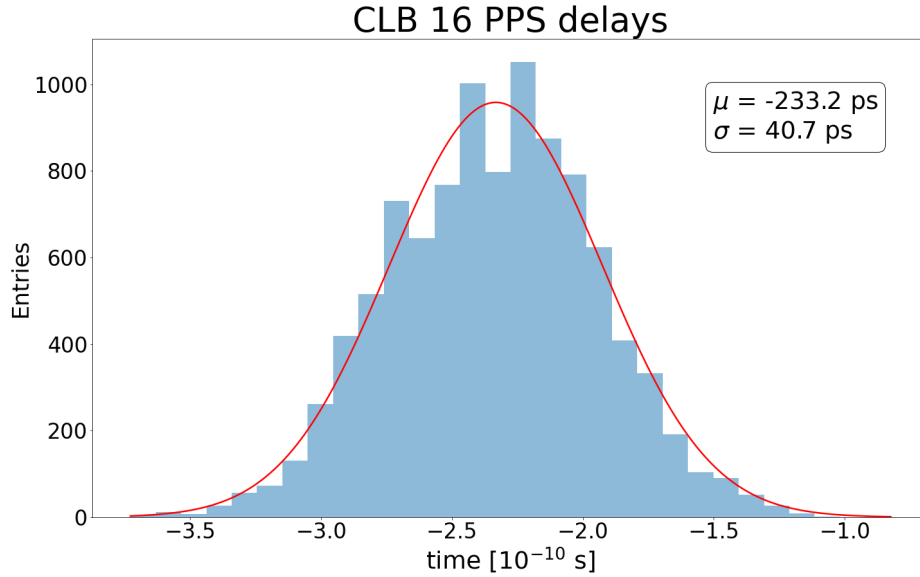


Figure 4.6: PPS delay measurement between the PPS signal of CLB-16 of the new configuration of the setup and the signal of CLB-1. This measurement comprises 10000 data points. The red line refers to the Gaussian fit, whose mean and sigma are listed in the box.

CLB	Mean (ps)	Max (ps)	Min (ps)	σ (ps)	Measures	Fit mean	Fit σ (ps)	$\tilde{\chi}^2$
Base	-209	-50	-355	41	10000	-209	42	8.05
2	-107	25	-240	41	10000	-107	42	4.88
3	-15	126	-165	41	9928	-14	42	4.74
4	-662	-434	-917	48	10000	-663	50	8.27
5	-282	-125	-435	42	10000	-282	42	4.16
6	-8	113	-131	34	9999	-7	33	10.50
7	-42	95	-178	32	10000	-42	34	5.39
8	-235	-103	-365	34	10000	-233	34	7.21
9	-234	-117	-362	34	10000	-232	34	7.67
10	-560	-350	-763	65	10000	-565	69	12.34
11	-264	-13	-443	49	10000	-265	41	14.30
12	-554	-419	-715	39	10000	-554	40	7.86
13	-491	-339	-639	43	10000	-491	45	6.45
16	-234	-82	-373	39	10000	-233	41	6.64
17	191	327	37	41	10000	192	41	6.39
18	44	175	-86	38	10000	44	39	6.06

Table 4.1: Oscilloscope measurement of the delays between the PPS signal of the CLBs with respect to the signal of the reference CLB-1. The measures were made with an oscilloscope Rhode&Schwarz RTO 1044 - 4GHz, acquiring in Real Time acquisition mode with a range of ± 25 ns. The red box highlights the largest value among the delays of all CLBs, which is smaller than the nanosecond.

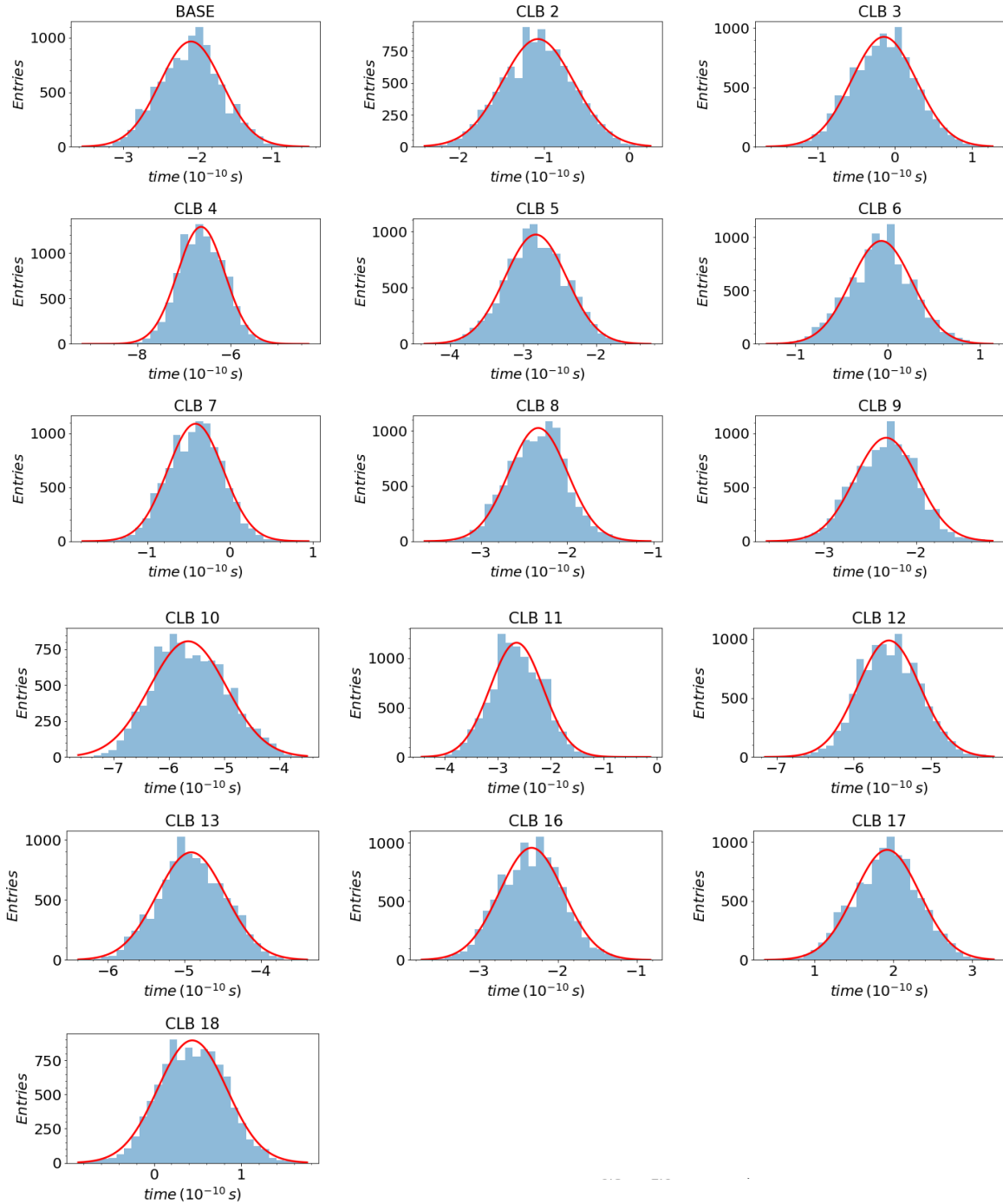


Figure 4.7: Oscilloscope measurements of the delays between the PPS signal of the CLBs with respect to the signal of the reference CLB-1. The random delays fit with a Gaussian curve with mean and sigma as indicated in Table 4.1.

in Fig. 4.6. The results of the statistics for the measurements are listed in Table 4.1. As one can see from the plots, all CLB PPS signals were synchronized with an accuracy better than one nanosecond, as expected. As a further check, I compared the PPS signal of the CLBs with the PPS signal produced by the DWRS, verifying by visual inspection the sub-nanosecond synchronization between them.

4.3 Control Unit validation

As explained in Sec. 3.2, a new firmware version, called Next Generation firmware, has been developed for the CLBs and it is going to replace the old one starting from the summer of 2021. The Next Generation firmware features several improvements, such as an upgraded, more reliable software design for a better control and modernized development tools for simpler builds. Because of these modifications, it has become necessary to upgrade also the Control Unit accordingly, in order to make it compatible with the NG firmware. For this purpose, a new version of the CU, the CU v10, has been developed. During the work for my thesis, thanks to the BCI equipment, I had the opportunity to elaborate the testing procedure for the new CU v10 and some of its feature, as described below. It is worthy to mention here that the correct functioning of the NG firmware and the CU v10 was crucial for the validation of the “full WR” setup. In fact, the CLB v4 boards used in the “full-WR” setup can operate only with the NG firmware, and a working CU was necessary for steering a large number of CLBs. Furthermore, at the same time a new strategy for the deployment and installation of the CU and DAQ processes on servers was designed. Once more, the BCI offered the chance of trying it out.

4.3.1 Dockerization of the CU and DAQ processes

At present, the installation of the Control Unit and DAQ processes on local servers can be rather cumbersome; as a matter of fact, they both require the installation of several software: the CentOS7 operating system, the Control Unit services, the Jpp module (Jpp is a Java inspired set of C++ interfaces, classes and methods, developed and extensively adopted within the KM3NeT project), and the Monrouter (see Sec. 3.3.2). These in turn depend on several software libraries and packets, such as C++, root 6, and many others. An independent installation of all these softwares is error prone. This usually translates into a big amount of work for developers and those in charge of operations.

For these reasons, the modularization and automatization of the CU and DAQ processes inside “docker” containers is under development. Docker [6] is an open source software development platform which allows one to package applications inside *containers*, allowing them to be portable to any other system. Containers virtualize the operating system splitting it into virtualized compartments, which share the kernel of the host machine, to run container applications. This structure is outlined in Fig. 4.8.

The Docker architecture is quite simple. The developer communicates with the docker infrastructure via the Docker client; the client sends the commands to the Docker daemon, which is responsible for actually executing the commands, such as the assembling, the running and the distribution of the finalized containers. The instructions for building a container image is written in a Dockerfile; those instructions can include for example the installation of a software package or the execution of some code. Once the Dockerfile

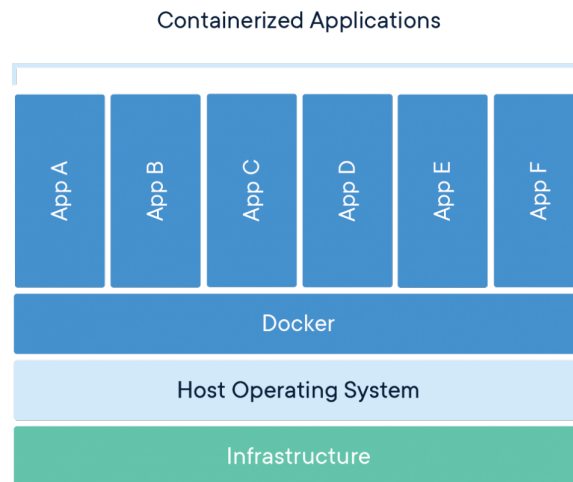


Figure 4.8: Basic structure of a docker container.

is configured, the docker image can be built from it. The images are read-only models which define the features of the developed application, its dependencies, and which processes need to be run when the application is started. Pre-built images can be also downloaded from a Docker registry, which is an open-source storage and distribution system for named Docker images, which allows the user to distribute its own images or to download pre-existing ones. Several public docker registry services exist, but the main one is Docker Hub [7].

A docker container “wraps” the application software within a box (namely, a container) that contains all the software the application needs and all the instructions it has to execute; this includes the operating system, the application code, required libraries, and so on. Containers are built upon docker images; since the latter are read-only, Docker adds a read-write file system on the read-only image file system in order to build the container. Moreover, when Docker creates the container, it creates a network interface so that the container can receive an IP address and communicate with the local host and with other containers if present. Once a container is built, it can be executed in any other environment without making any changes, offering a great advantage in terms of modularity, portability and scalability. The container approach indeed allows large applications to be strip down into smaller and easily transportable pieces which can be run anywhere. This way, the distribution of an application becomes way more efficient, easy and fast, as well as its testing.

Another useful tool within the Docker framework is the Docker Compose tool, used to define and run multi-container applications. With Compose, the user creates a YAML file to configure the application services, that is all the different containers required for the application execution, and create them from that configuration. In practice, docker Compose is an automated multi-container workflow, which orchestrates the creation and running of multiple containers as a single service. Each of the containers runs in isolation, but can interact with the others when required. As a result, Docker Compose

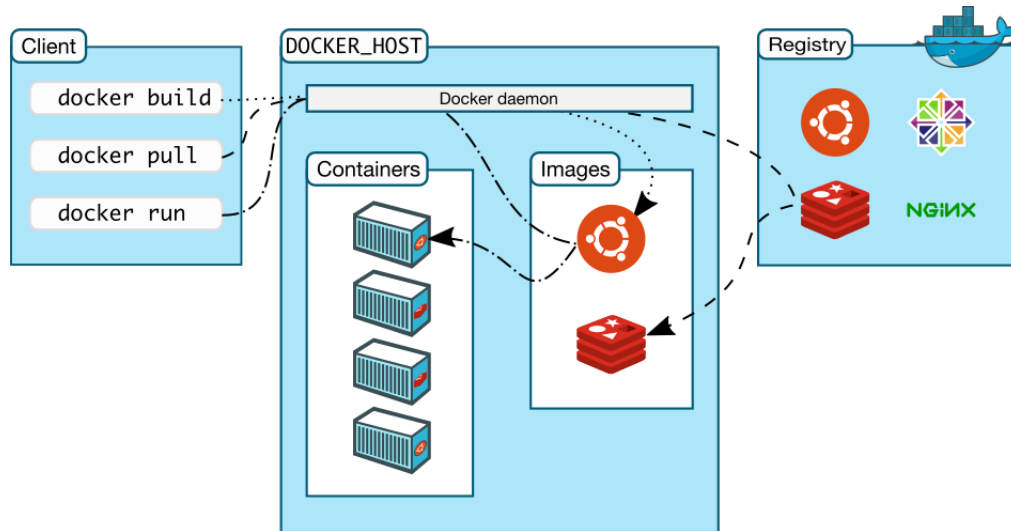


Figure 4.9: Architecture of the Docker system, composed by the Docker client and the Docker daemon. The Daemon can pull pre-built images from a Docker registry, such as Docker Hub, or push images into it.

allows one to deploy an application based on multiple containers with a quick and easy configuration, thanks to the YAML files. Moreover, it re-builds only containers that have changed, reducing times in case of updates of components.

With a view to the incoming and gradual deployment of Detection Units and the consequent need of distributing the data acquisition processes on the multiple shore station servers, the requirement of a scalable and easily distributable and testable system for instantiating the CU and the DAQ can be met exploiting the Docker technology, thus “wrapping” all the required software inside containers. Therefore, in this scenario, the user in charge of installation operation would neither have to worry about the operating system he may want on the host server, nor he would need to care about the Jpp/ControlUnit/Monrouter installation or about software updating. The only operation he would have to do is to download the pre-built docker image and start a container. In case he would like to make some changes, he could still download the Dockerfile, build its own image and start the container.

At present, the instantiation of the CU and DAQ processes inside docker containers is being tested at the BCI, both for what regards the “Broadcast” test bench and the “full WR” test bench. As a matter of fact, the Control Unit services and the TriDAS processes (as listed in Sec. 4.1) run inside two separate containers hosted on the corresponding BCI Bastion server. In this sense, the BCI allows the developers to test the deployment and verify the performances of the DAQ processes within the Docker scenario before applying it extensively on the shore station servers or on test benches in other sites.

4.3.2 Downsampling of Slow Control data

As mentioned above, a new upgraded version of the Control Unit, the version 10, has been recently developed. Most updates concerned the Detector Manager, which needed to cope with the new NG firmware version. In order to maintain its retro-compatibility, the Detector Manager has been consequently upgraded in order to control both the old

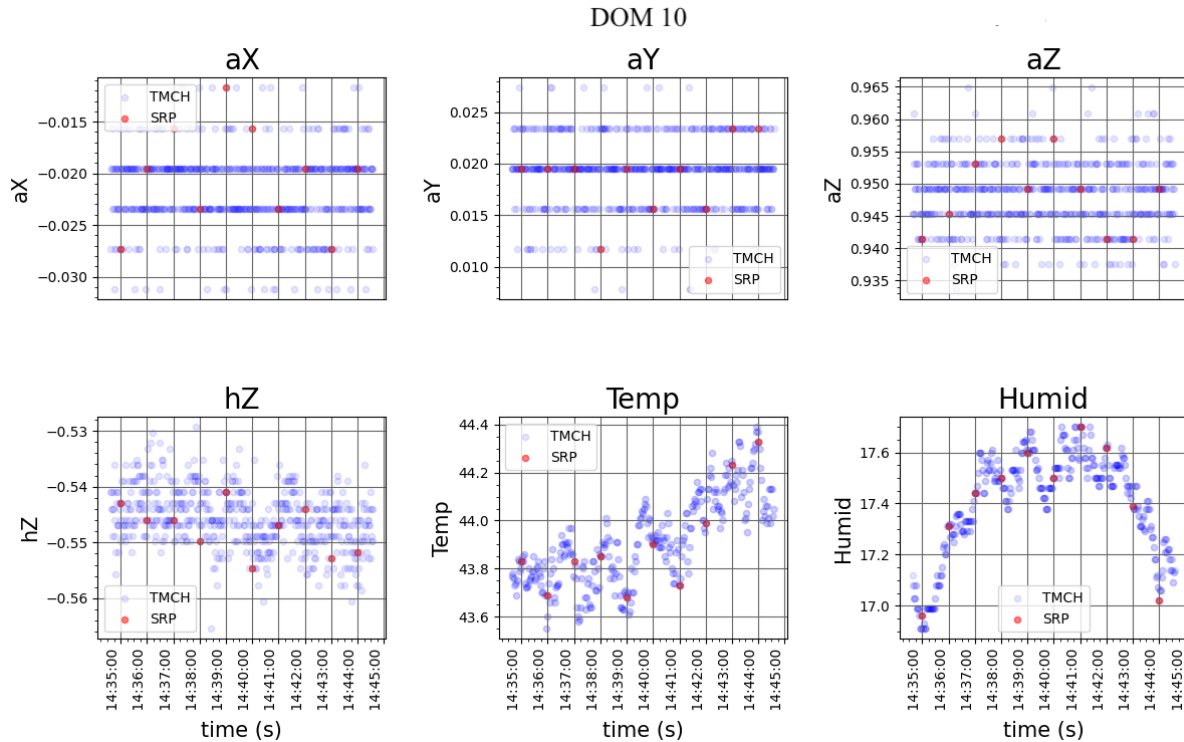


Figure 4.10: Some monitoring sensor data (the three components of the accelerometer, the third component of the compass sensor, the temperature and the humidity) retrieved by the SRP (red points) and TMCH channel (blue points) as function of time, from CLB-10 of the “full White Rabbit” setup. In this case, the downsampling was set to one update every 60 seconds.

version of the CLB firmware and the new one. The other main modification regarded the downsampling of Slow Control data from CLBs.

Information from monitoring sensors, listed in Sec. 3.3.2, is delivered via two distinct and independent channel: via the TMCH channel as explained in Sec. 3.3.2 and via the SRP protocol directly to the DM which registers them in its datalog files. While for the TMCH channel UDP packets containing monitor sensor parameters are sent every 100 ms (i. e. one per timeslice), with the SRP protocol they are sent with a shorter frequency, typically 1 packet every second, which can be also downsampled requiring information on a longer time basis only, by setting the interval of time between deliveries to larger customizable values.

As part of my activity at the BCI, I validated the downsampling feature of the CU v10, providing with the due feedbacks the CU developers in order to produce a robust algorithm. First, I have verified the correct interaction between the DM and the NG firmware on the CLB version 4 by steering them through the state machine as commanded by the DM. Then, I have written two separate Python codes aimed at retrieving and parsing respectively sensor data from the TMCH channel and from the DM datalog files. The former has been developed within the *km3pipe* [8] environment, one of the most common software framework for analysis developed by the KM3NeT collaboration. Within this framework, the script that I have designed is able to connect to

the BCI JIlgier and retrieve from it monitoring data as selected specifically with the “IO_MONIT” tag. Collected monitoring sensor parameters are gathered and stored into dataframes for a later comparison with the SRP data, which in turn were extracted by parsing the DM datalog files produced every ten minutes. By default, the SRP downsampling frequency is set to 1 Hz; hence, inside datalog files, monitoring parameters were registered every second. The downsampling frequency can be set to the desirable value by the user in the CU interface. At the BCI, I tested the setting of the downsampling that corresponds to saving data every second (default), and every 10, 30 and 60 seconds. Eventually, for each CLB composing the setup, all the monitoring parameters as retrieved both from the SRP and TMCH channel were plot as a function of time, in order to check for the downsampling accordance. A sample plot is shown in Fig. 4.10. All the resulting plots, considering all sensor data from each CLB and all the downsampling frequencies can be found here: [9]. All the tested downsampling frequency corresponded to the set values. Thus, the downsampling feature in the CU v10 indeed worked as foreseen. This check was mandatory in order to validate the proper functioning of the downsampling feature in the new CU v10 before its installation via docker container on the Bastion server of the latest configuration of the “full WR” test bench. The TriDAS processes correct functionalities have been also verified, so that I could thereby proceed with data acquisition from the TTDC and TMCH channels for the time synchronization validation of the setup and study the integrity and stability of the TMCH data.

4.4 Clock synchronization validation

After the oscilloscope validation of the PPS synchronization, in order to improve and speed up the time synchronization validation of the setup I studied the synchronization of the WR clock signal through the reconstructed times of PMT hits by the CLBs. To check this, I exploited the fact that the OctoPAES boards are able to emulate optical signals for the PMTs. As a matter of fact, the hit times of those emulated analog signals are reconstructed and digitized by the TDCs integrated within the CLBs, which assign them the timestamp according to their clock, received by the WWRSs. As a consequence, by analyzing the hit times of those signals downstream of the DAQ chain, I was able to study the time synchronization accuracy between different CLBs. Moreover, thanks to the exploitation of online analysis tools, this approach allowed me to collect data contemporaneously from all the CLBs for several days of data taking in a stable way, something which was not possible with an oscilloscope. In the following, the adopted strategy will be illustrated.

4.4.1 OctoPAES boards

For the time synchronization validation of the “full WR” setup, I have made extensive use of the OctoPAES (OP) boards, which played a crucial role in the validation procedure. Hence, in this section a brief description of the boards is given.

The OctoPAES boards (where PAES stands for Photon and Acoustic Emulation of Signals) have been developed by the KM3NeT collaboration together with the Bologna INFN electronic section. As their name suggests, they are able to emulate the presence of the PMTs, the acoustic sensor and the Octopus board of the standard DOM implemen-

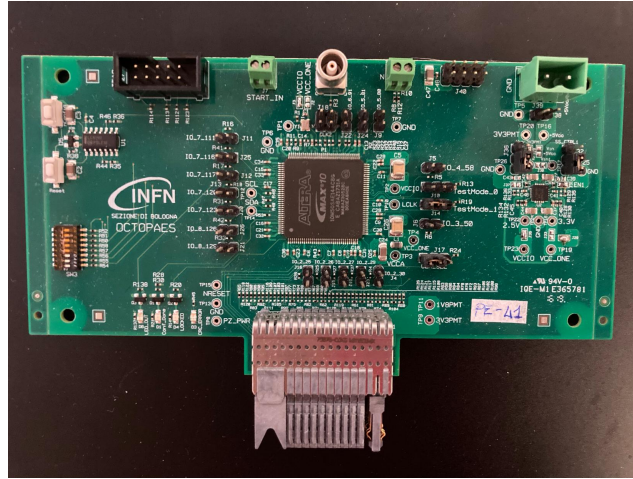


Figure 4.11: Picture of an OctoPAES electronic board; on the bottom left, the dip switches for selecting the MIF file page and the Large/Small type can be seen.

tation. Thus, they can emulate fake optical and acoustic signals to be then processed by the CLBs. Similarly to a real DOM, where one Octopus Large and one Octopus Small are present and plugged on the CLB, also CLBs at the BCI test benches host two OctoPAES boards, connected with the same specific connector of the Octopus boards: one of them, the OctoPAES Large board, emulates signals for 19 PMTs whereas the other, the OctoPAES Small board, for the remaining 12. The Large/Small configuration of an OctoPAES board can be set easily by selecting a dip switch mounted on it (shown in the bottom left of Fig. 4.14).

The emulation of optical signals is highly customizable; as a matter of fact, the boards allow one to select among different PMT single-rates and there is the possibility for the user to set per-PMT configurable hit patterns. The latter can be done by customizing and uploading on the board programmable logic the so-called “MIF” file, which encodes the instructions on the hit pattern. This is binary file which is uploaded in the ROM of the board during the flashing of the firmware inside the board Complex Programmable Logic Device (CPLD). The MIF file is organized as follows: it is partitioned in 128 pages, each of them containing 32 rows. The first 31 rows correspond to the 31 emulated PMTs of the DOM, whereas the 32th row is left for the implementation of the waveform signal for the acoustic emulation; for our purposes we will concentrate exclusively on the optical signal emulation, i.e. on the first 31 rows.

Every row consists in 256 digits which represent a tick of the board internal clock. Since this clock operates at a frequency of 80 MHz, one tick corresponds to an interval of 12.5 ns. The OctoPAES generates a square waveform for each PMT according to its related MIF row: the total available waveform duration is hence 3.2 μ s, and digits set to 1 will correspond to the high-level state of the waveform, emulating the signal generated on the PMT by a real photon, whereas digits set to 0 will correspond to the low-level state. Thus, the number of consecutive digits set to 1 defines the Time Over Threshold of the emulated optical signal; for example, two consecutive digits set to 1 in a row will emulate the presence of a photon hitting the corresponding PMT at the time indicated by the position of the said digits with a Time Over Threshold equal to 25 ns. In order to recreate hits on the PMTs and a hit pattern within PMTs of the same DOM or even

between different DOMs in the string, one just has to change the proper digits from 0 to 1 in the proper pages and rows. The desired MIF page number, whose hits will be generated, can be simply selected by setting 7 dip switches on the board and by forming with them the due binary combination corresponding to the desired page number. The rate of injection of the hits in the CLB can also be set by simply applying a jumper on the board in the proper way. Some predefined frequencies can be chosen, typically 1 Hz, 100 Hz, 1 kHz or 5 kHz. Note, however, that the signal injection is not continuous; as a matter of fact, on a single PMT (i. e. on a single row) the total available time for the hit emulation is $256 \text{ digits} \times 12.5 \text{ ns} = 3.2 \mu\text{s}$, whereas for example an injection frequency of 5 kHz corresponds to a period of $200 \mu\text{s}$ between the injection of a bunch of hits and the following one. Nevertheless, in a timeslice frame of 100 ms, still a high payload on the system can be generated, producing up to 500 bunches of hits for every timeslice.

It is important to underline the fact that the hit time as indicated by the digits in the MIF file refers to the time of the board internal clock. As a matter of fact, once they are injected in the CLB, the hit digital waveforms are timestamped by the TDCs with a nanosecond precision, according to the CLB clock received by the WWRS, and incorporated within the timeslice frames.

4.4.2 Clock synchronization validation strategy

OctoPAES boards offer a great opportunity for evaluating the time synchronization of CLBs in a test bench string, as they allow one to emulate custom-made optical signals in the absence of real PMTs. Ideally, if the OctoPAES clocks on all the CLBs composing the string were perfectly synchronized, and all the boards started injecting signals exactly at the same time according to the same MIF file, then we would have simultaneous hits on all the CLBs. Since the emulated hits are then timestamped by the CLBs via the TDCs according to their clock, by comparing the times of those hits as registered by the CLBs we could measure the delay between them. As the White Rabbit protocol ensures a time synchronization accuracy smaller or equal than one nanosecond, we would in principle expect those delays to be as such. However, this is not completely true for the following reasons.

Of course, in reality neither the OctoPAES clocks can be perfectly synchronized nor the starting signals for injection can be perfectly simultaneous for all of them; this means that if we computed the delays between the hit times as registered by the different CLBs, we would obtain values generally different from zero, as they would include not only the delays between the CLBs clocks but also the systematic offset delays between the OctoPAES ones. Nevertheless, if the precision on the CLB clock synchronization is higher than one nanosecond, as we verified with the oscilloscope analyzing the PPS signal, we would still expect the delay values to keep constant over time since they reflect the constant systematic offset introduced, and we would expect to find discrepancies of those values not larger than one nanosecond.

The other reason why we would not expect to find delays *smaller* than one nanosecond concerns the TDCs resolution. As a matter of fact, the resolution on hit times as registered by the CLBs is given by their TDC resolution. In general, the resolution of a TDC is determined by its clock frequency and the number of clock phases. For TDCs inside the CLB, the $4\times$ -oversampling technique has been chosen: a PLL inside the FPGA generates two clocks of frequency equal to 250 MHz (i. e. 4 ns period) but different phases

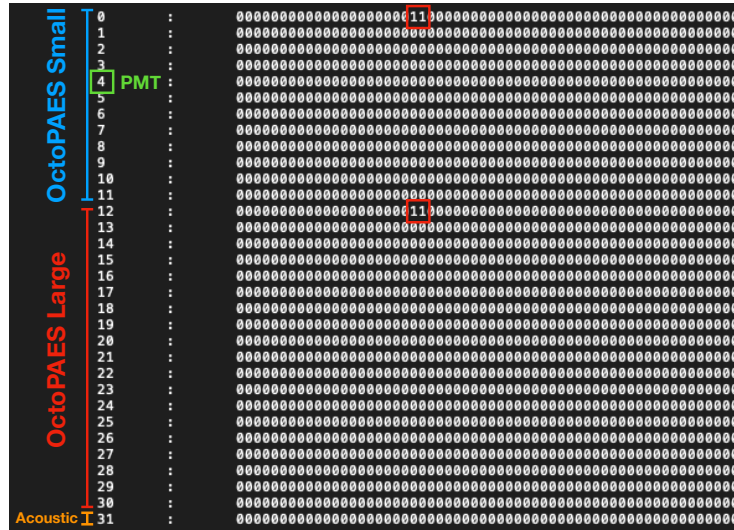


Figure 4.12: Calibration page in the MIF file. The first column refers to the PMT channels. Hits in the rows are highlighted by the red boxes.

(CLK_0 and CLK_{90}). These two phases are routed to a deserializer primitive inside the input/output blocks of the FPGA. The deserializer primitive allows the oversampling of an incoming data stream on both rising and falling edges of the generated clocks, CLK_0 and CLK_{90} , resulting in four times the sampling frequency with respect to the original clock (CLK_0 , CLK_{90} , CLK_{180} , CLK_{270}). Thus, with four phases and a frequency of 250 MHz, the obtained resolution is 1 ns (1 GHz). This technique is illustrated in Fig. 4.13.

Therefore, the nanosecond resolution of TDCs implemented in the CLB FPGA anyway prevents one from finding delays values smaller than the nanosecond. The one just described is the basic idea behind the adopted validation strategy for the time synchronization of the CLBs of the “full WR” test bench. Before making the first steps, the “full WR” test bench configuration for what concerns the OctoPAES boards was such that all of them were in Master stand alone mode; this means that the internal clock is used and the hit emulation is started and stopped by simply pressing a button on the board panel. The implemented firmware included a simple state machine which provides only “running” and “not running” modes. In running mode, the page of the MIF file are injected at a constant rate which is determined by some jumpers in the proper positions on the board panel, and the selected frequency was 3 kHz. This version of the firmware was originally developed for generating a constant data stream with the purpose of testing the performance of the DAQ system under different throughput.

As a first check, I inspected the hit waveforms with the oscilloscope by connecting it to the proper pins on the OctoPAES panel. By comparing the waveforms of different CLB hits it was immediately apparent that for several OctoPAES boards the internal clocks were migrating, whereas for others the hit frequency was unstable. For this reason, before proceeding further, it was mandatory to change the OctoPAES configuration and to replicate the stable and well-tested one existing on the “Broadcast” test bench. In the latter, all the OctoPAES boards act as Slaves whereas a further Master board, realized by means of a Kintex KC705, is required to act as a common clock source and to distribute the clock and the start/stop signal to the OctoPAES boards. The clock

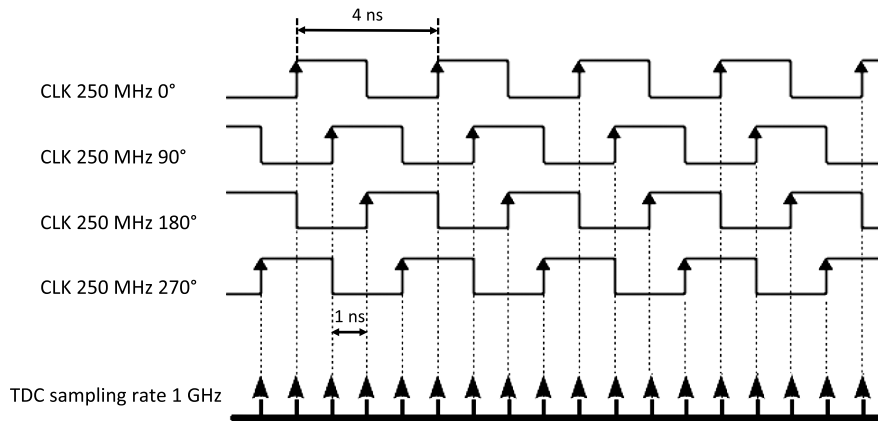


Figure 4.13: Scheme of the 4 \times -oversampling technique. The sampling quadruples the clock frequency using four phases of the original clock, shifted by 90 degrees each, thus obtaining a sampling frequency of 1 GHz when using a clock with a period of 4 ns. Figure taken from [36].

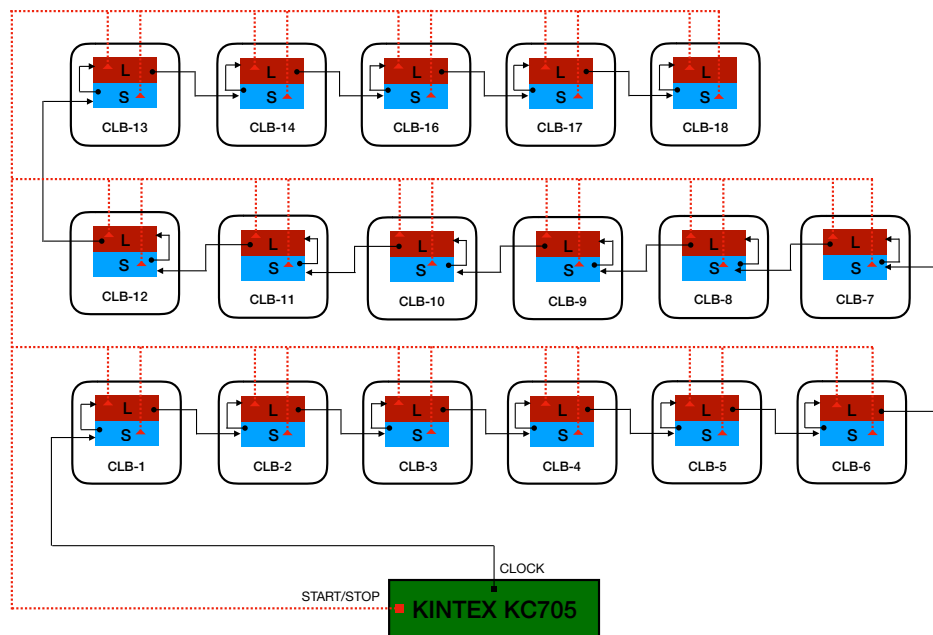


Figure 4.14: Schematic overview of the connections implemented for the OctoPAES system on the “full WR” setup: the external Kintex KC705 board acts as a master and transmits the clock signal in daisy chain to the OctoPAES (Large ones are labelled with an “L” and Small ones with an “S”) and the start/stop signal in parallel.

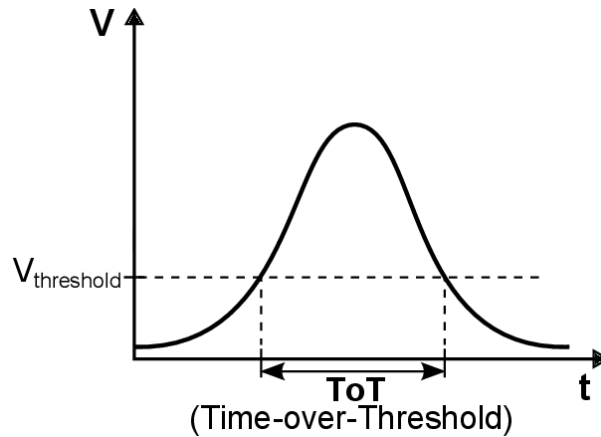


Figure 4.15: Representation of the Time Over Threshold, i. e. the time during which the signal voltage is above a voltage threshold.

signal is distributed according to a daisy-chain scheme, whereas the start/stop signals are triggered to all the OctoPAES boards simultaneously via parallel connection, as depicted in Fig. 4.14. In this way, except for the delays generating during the transmission of the clock signal in daisy chain, the above described condition is met. It is worthy to mention that the OctoPAES firmware used in these tests contained a dedicated MIF file with a *calibration* page, in which only two coincident hits with Time Over Threshold equal to 25 ns are inserted on channels 0 (OctoPAES Small) and 12 (OctoPAES Large). This means that two consecutive bits, in the same location with respect to the starting point of the rows, are set to 1, satisfying the necessary time coincidence condition (L1 condition, see Tab. 3.1) as described below. This can be seen in Fig. 4.12.

In the DataFilter process the L1 trigger condition imposes the coincidence of two or more L0 hits on different PMTs in the same DOM, within a time window of ~ 25 ns; thus, in order to recreate an L1 condition, at least two rows in the MIF file must have at least one digit set to 1, and those digit positions on the different rows must not be distant more than one bit, otherwise they will not fit inside the 25 ns time window. In our case, the position of the digits set to 1 on rows 0 and 12 was coincident. Moreover, the choice of having two consecutive bits set to 1 is due to the fact that the expected Time Over Threshold (Fig. 4.15) of a single photo-electron signal, given a typical threshold for the PMTs, is about 26.5 ns: hence, by concatenating two consecutive 1 bits a Time Over Threshold of 25 ns is obtained and a typical photo-electron signal is emulated. Another page which is present inside the MIF is the so-called *background* page: it is created inserting a hit of 25 ns ToT in a random location over the 256 bits in every row. The purpose of the background page is to emulate in an approximate way the hit rates of background photons, mainly due to ^{40}K decays and bioluminescence, on DOM PMTs. Unlike real background events which have a Poissonian probability distribution, the probability distribution of a hit over the 256 bits is assumed to be uniform. In order to emulate the real-conditions hit rates, the firmware implements a state machine that injects a background page with a selected frequency of ~ 5.08 kHz; on top of that, the calibration page is injected with a frequency which can be selected with jumpers and which can take values equal to 1 Hz or 10 Hz. With this value of background frequency for every PMT, a throughput of $31 \text{ PMTs} \times 5.08 \cdot 10^3 \text{ Hz} \times 6 \text{ B} \simeq 940 \text{ kBps}$ per CLB is

CLB	Mean (ns)	Min (ns)	Max (ns)	std. dev. (ps)	Measures
2	3.021	2.800	3.347	93	1179
4	-2.956	-3.380	-2.023	120	1012
5	-5.294	-5.521	-3.868	170	1044
6	4.185	3.986	4.550	87	1058
7	1.705	1.518	1.970	69	1026
8	-1.243	-1.631	-0.6	104	1041
9	-4.133	-4.595	-3.875	85	1009
10	0.81	0.54	1.5016	98	1016
11	-1.400	-2.642	-1.905	106	1020
12	-4.376	-4.645	-3.880	68	1013
13	-0.74	-0.89	0.58	70	1048
14	-3.451	-2.815	-3.764	91	1003
16	-6.183	-5.419	-6.721	89	1121
17	3.029	2.631	3.667	101	1096
18	2.100	1.840	2.848	117	1253

Table 4.2: Delays between signals injected by the OctoPAES “Large” boards on the CLBs. Delays are computed with respect to the reference OP on CLB-1, and are measured with an oscilloscope with 200 ps sampling frequency.

obtained. The hit injection frequency was chosen to be 1 Hz for all the boards, implying the generation of one L1 hit per channel every ten timeslices. The channel from the ‘Large’ OctoPAES boards on the CLBs was chosen as the reference one, i.e. only hits from channel 12 were selected, and then I computed the delays between those hits and the ones belonging to a reference CLB, namely the CLB-1.

In order to do that, I developed an online tool able to measure those time delays: it consists in a Python program based on km3pipe, which connects to the BCI JLigier and fetches “IO_L1” data. Collected and gathered information is then parsed, the hits on channel 12 are selected and their times are extracted. Hit times are combined in order to compute the time differences between hits on the reference CLB-1 and hits on all the other CLBs. The resulting values are stored inside a dataframe and written regularly every few hours to a csv file in order to be analyzed off-line. By plotting the time differences over time, the synchronization accuracy and its stability can be investigated. Beside this, the actual L1 injection frequency can be computed from the period between consecutive hits. The injection frequency turns out to be approximately $f \simeq 0.98$ Hz.

A period of almost 9 days of data taking was considered. During this period, data taking was interrupted several times to perform power cycles of the whole setup. This was done in order to verify the stability of the delays to power interruptions. The results are shown in Fig. 4.16, where also the turn-off/turn-on moments are highlighted. After the power cycles, delay values remained the same. Out of the 18 CLBs of the setup, two of them (namely the CLBs numbered as CLB-3 and CLB-15) presented hardware issues which prevented them to be considered for those time synchronization validation measures. In particular, CLB-3 was not able to lock to the White Rabbit clock signal, and this prevented the state machine to perform the transition into running state. CLB-15 instead showed an issue concerning the I²C bus that again caused the CLB to enter in “ERROR” state and prevented it from going into running state. Thus, the global

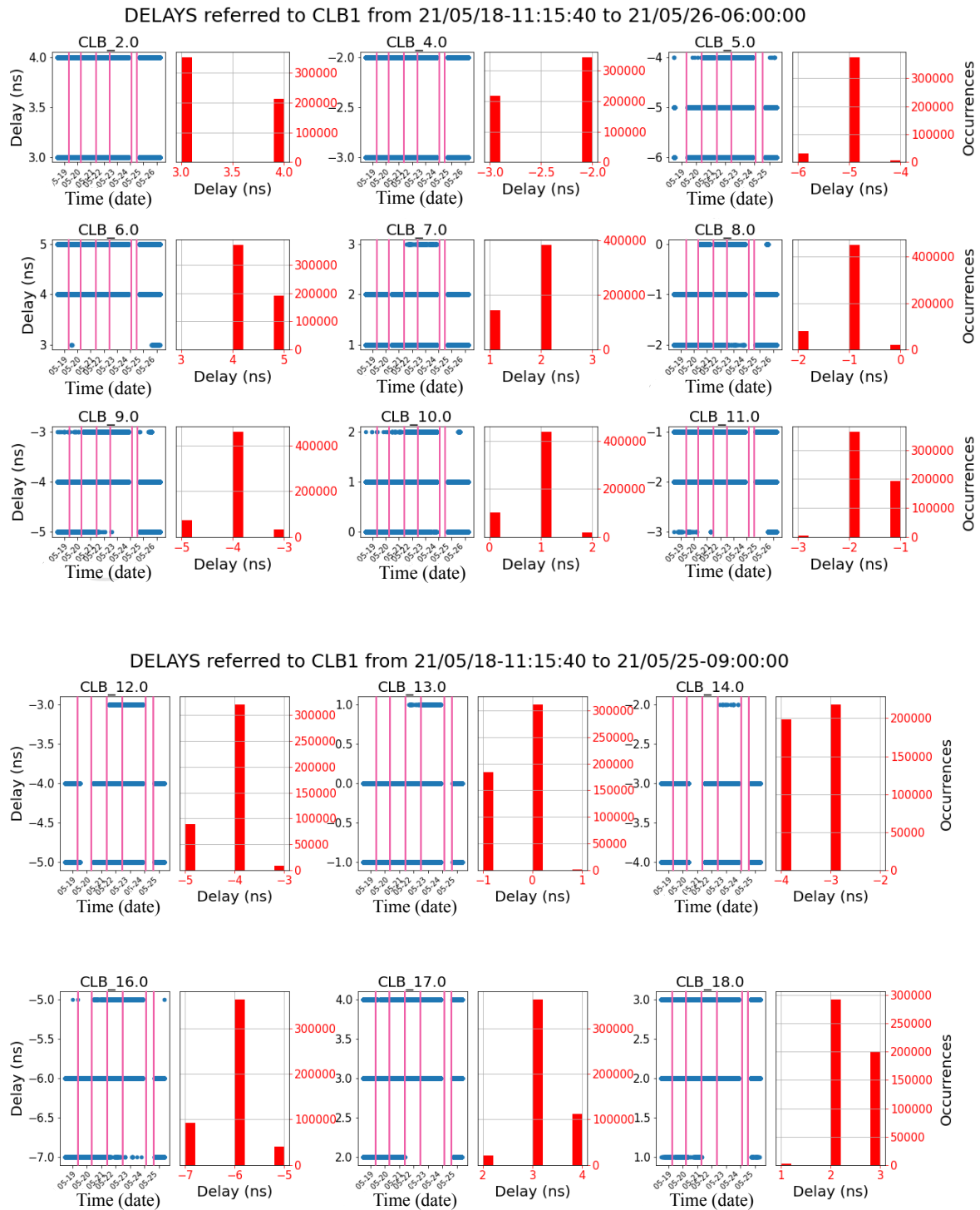


Figure 4.16: Delays between the hits generated by the OctoPAES boards and time-stamped by the respective CLBs. Time differences are computed for each CLB with respect to the hits registered by the CLB-1. On the left-hand plots, the time differences are plotted over time, whereas the right-hand plots shows the relative distribution of delay values. Turn-off/turn-on cycles are highlighted by the pink vertical lines on the plots: in the first four cases, the turn-off and turn-on are so near in time that their lines appear superimposed in the plots; in the last case instead, the turn-off and turn-on moment are visibly separated.

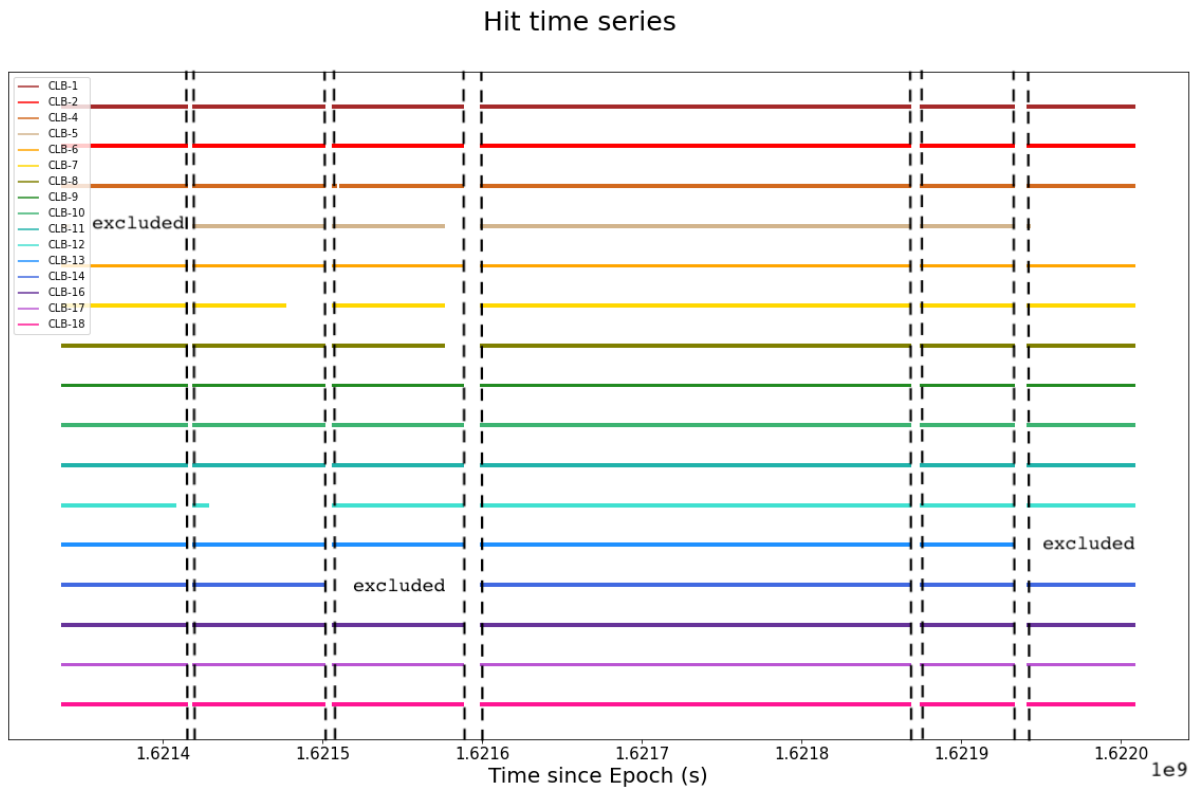


Figure 4.17: L1 hit occurrences distribution over time. Black dashed lines highlights the turn-off and turn-on times of data acquisition, due to the power cycles of the CLBs. Gaps in the distribution within acquisition time, as occurred for some CLBs, indicate that the CLB has lost the clock Track-phase. In some occasions, some CLBs were excluded from the measurements due to issues with cables delivering the start and stop signals for the OctoPAES boards or with the software program: those cases are marked with the “excluded” label in the plot.

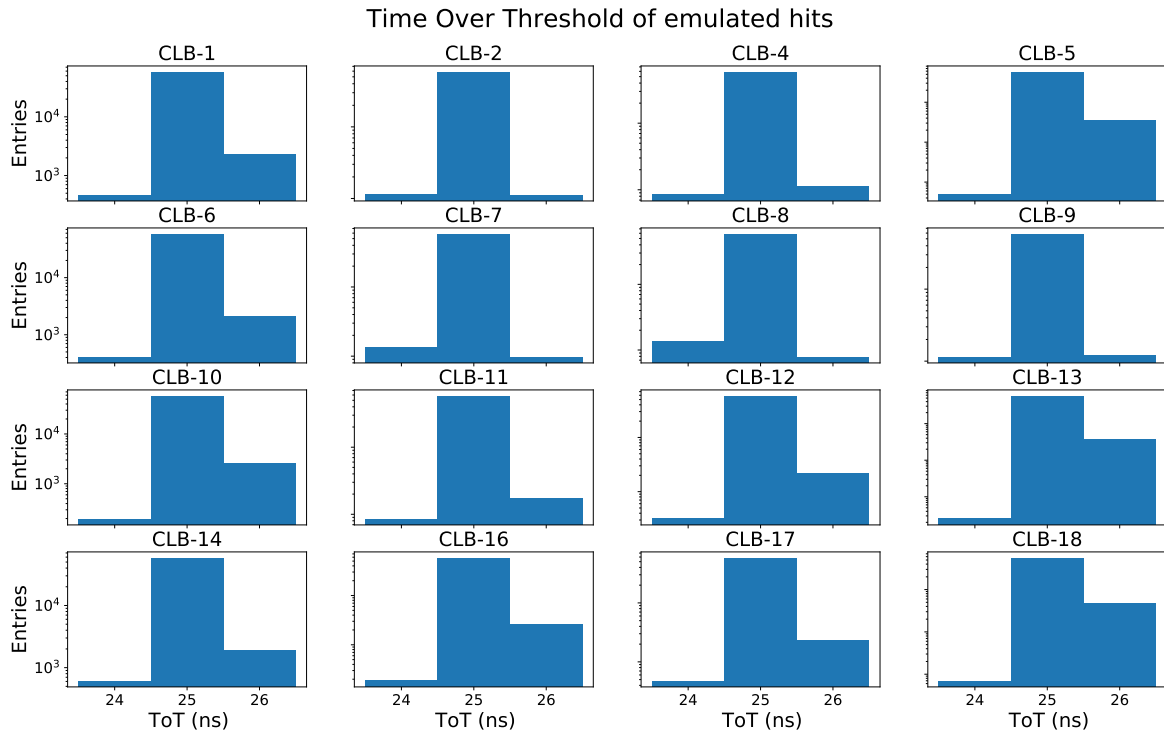


Figure 4.18: Time Over Threshold distributions of the L1 hits as emulated by the OctoPAES boards and timestamped by the CLBs. Distributions are centered on 25 ns which is the ToT specified in the MIF file, with a discrepancy of 1 ns due to the TDC resolution.

throughput from the string reached the value of $\simeq 15$ MBps. The PMT single rates and the input throughput on the DAQ server were monitored over time exploiting the CLBSwissKnife tool and the Linux *dstat* tool [10], confirming their stability throughout the whole observation window apart from the periods where some CLBs lost the Track-phase causing the TTDC packets to be discarded by the DataQueue and the throughput to decrease. Such de-synchronizations were confirmed also by the developed monitoring program (see later), which highlighted this loss of Track-phase. As one can see from Fig. 4.16, the delay values for all the CLBs fluctuate around a specific value, given by the delay between the OctoPAES Large clock and the clock of the OctoPAES Large on CLB-1, with discrepancies not larger than one nanosecond. The delays between the injected signals from the OctoPAES were also measured with an oscilloscope extracting the signal from the corresponding pin, in order to compare them with the observed delay values in Fig. 4.16. Taking into account the nanosecond resolution of the TDCs, the measured values, reported in Fig. 4.2, are compatible with the delay values retrieved by the program, indicating that the observed delays refer indeed to the systematic delays between the OctoPAES boards and not to delays between the WR clocks of the CLBs. Some CLBs happened to occasionally lose the WR clock Track-phase during data acquisition, as one can see from Fig. 4.17. This was observed for 5 CLBs, with a frequency of 1-2 occurrences over the 9 days of data taking. To recover from this situation, a reboot of the CLBs has proved necessary. This represents an unexpected behaviour which needs to be better investigated, as it undermines the synchronization stability of the system.

As a further integrity check on the TTDC data stream, the ToT of L1 hits have been extracted and plotted over time. Results are shown in Fig. 4.18: considering almost 18 hours of data taking, ToT distributions are centered on the value of 25 ns as set in the MIF file and include also values equal to 24 and 26 ns, compatible with the 1 ns resolution of the TDCs. The code of the developed Python program is available on the following GIT repository [11].

4.5 Monitoring channel validation

The other validation step which I performed during my thesis work relates to the monitoring channel (TMCH, see Sec. 3.3.2). In particular, I have studied the TMCH data stream from the “full White Rabbit” setup, verifying its stability and its integrity. This includes monitoring and inspecting the correct stream of TMCH UDP packets sent by the CLBs and looking for eventual packet losses, slowdowns, or other malfunctions such as de-synchronization issues.

For this purpose, I developed a Python program for retrieving the TMCH data from the KM3NeT detector elements (i. e. DOM and Base Module CLBs) and analyzing the stability and the synchronization of the data stream. Originally conceived for the specific task of monitoring the TMCH data stream flowing out from the “full WR” setup, it has been progressively improved and adapted for the more extensive purpose of real-time monitoring the TMCH channel of several DUs, like for example the six ones which currently compose the ARCA detector, as it will be illustrated in the following.

The main core of the program was first developed and tested within the well-known and safe environment of the BCI “Broadcast” test bench and ported only afterward on the “full White Rabbit” test bench. Built around the km3pipe framework, it subscribes the “IO_MONIT” tag, collecting from the BCI JLigier the monitoring channel UDP packets coming from the CLBs of the test bench. The script analyzes each incoming UDP packet, extracts the relevant information and fills a dataframe whose rows contain the following values:

- The source of the packet, i. e. the CLB (DOM) number; all the other values in the same row refer to this particular CLB;
- The corresponding run number;
- The timestamp in milliseconds, that is the start time of the timeslice to which the packet belongs. For simplicity, we will refer to it as the *packet time*;
- The time, in milliseconds, of packet processing as recorded by the machine on which the program is running. In the following, this will be referred to as the *machine time*;
- The difference between the current *packet time* and the *packet time* of the previous one ($T_{100\text{ms}}$); as one packet per timeslice is produced, this value is expected to be 100 ms, i. e. equal to the timeslice duration:

$$T_{100\text{ms}} = (\textit{packet time})_i - (\textit{packet time})_{i-1} \quad (4.1)$$

- The total number of UDP analyzed packets by the program from the start of the run up to the current incoming packet ($N_{observed}$);
- The expected number of UDP packets so far ($N_{expected}^{packet\ time}$), calculated as the difference between the current *packet time* and the *packet time* of the first packet of the run:

$$N_{expected}^{packet\ time} = \frac{(packet\ time)_i - (packet\ time)_{start}}{100} \quad (4.2)$$

- The expected number of UDP packets so far ($N_{expected}^{machine\ time}$), but calculated as the difference between the *machine time* of the current packet and the *machine time* of the first packet of the run:

$$N_{expected}^{machine\ time} = \frac{(machine\ time)_i - (machine\ time)_{start}}{100} \quad (4.3)$$

- The transmission ratio ($R_{packet\ time}$), calculated as the ratio of the total number of packets analyzed up to the current one over the expected number of UDP packets as calculated considering the *packet time*:

$$R_{packet\ time} = \frac{N_{observed}}{N_{expected}^{packet\ time}} \quad (4.4)$$

- The transmission ratio ($R_{machine\ time}$), calculated as the ratio of the total number of packets analyzed up to the current one over the expected number of UDP packets as calculated considering the *machine time*:

$$R_{machine\ time} = \frac{N_{observed}}{N_{expected}^{machine\ time}} \quad (4.5)$$

- The *delay* between the *machine time* and the *packet time* of the current packet:

$$delay = (machine\ time)_i - (packet\ time)_i \quad (4.6)$$

- The value of a bit related to the synchronization status of the CLB: value “1” means that the CLB is synchronized and in Track-phase, whereas value “0” means that the CLB is not synchronized.

The dataframe is then refreshed regularly every ten seconds and written on csv files. If the difference between two consecutive packets T_{100ms} is different from the expected 100 ms, the program outputs an error message, as this is an indication of a possible loss of packets. In that case, dividing the time difference by 100 ms, the number of missing packets is calculated.

At this point, in order to enhance the monitoring program usability and to make it more user-friendly I implemented it within the Grafana [12] analysis framework.

Grafana is a multi-platform open source analytics and interactive visualization web application. It provides charts, graphs, alerts and many other features for the web when connected to supported data sources. End users can create complex monitoring dashboards using interactive query builders, so it represents the ideal graphical interface

for my monitoring program. Grafana works with databases, which are taken as input data sources: in fact, it supports natively dozens of databases, among which InfluxDB [13], the one I chose for my purposes. InfluxDB is an open-source time series database developed by InfluxData. It is specifically optimized for fast, high-availability storage and retrieval of time series data in fields such as operations monitoring and real-time analytics. InfluxDB has no external dependencies and provides an SQL-like language (Structured Query Language), listening on port 8086, with built-in time-centric functions for querying a data structure composed of points, series and measurements. Each *point* consists of several key-value pairs formed by a field, whose values can be integers, floating points, string or booleans, and a timestamp. Those points can be grouped together by a set of key-values called *tags*, forming a *series*. Finally, series are grouped together by a string identifier to form a *measurement*. Therefore, points inside an Influx database are indexed by their time and tags. Influx allows one also to define and set retention policies on a measurement, that is to control how data are downsampled and deleted.

In order to write the dataframes filled by my monitoring program into a Influx database it was necessary to write a Python script which runs in parallel to the monitoring program and has the role of importing the csv files generated by it and transfer their content into the database, associating properly the timestamp, tags, and field values: the UDP packet *machine time* becomes the timestamp of the database points, the DOM number serves as tag, and all the other monitoring parameters, listed above, act as fields.

Thus, every row in the csv file created by the monitoring program becomes a point in the database, identified from the tag given by the DOM number; all points with same tag, i. e. all rows with the same DOM number, form a series of points as a function of the timestamp, which is the packet machine processing time. Since a new csv file is written every ten seconds, the script needs to be run for every new csv file created, in order to extract its data and load them on the database. This job is handled by a shell script which constantly looks for new csv files and launches the latter script whenever it finds one; after that, it deletes the previous file in order to save disk space. As for what concerns the adopted retention policy, data in the database are conserved for 25 hours; after that, the first hour of acquisition points is deleted. This way, the user has at his disposal at least the last 24 hours of monitoring data. At this point, the database can be read by the Grafana web application, thanks to which the user can visualize graphically and in an interactive way all data in the database.

4.5.1 Dockerization of the monitoring program

A further step in the development of the monitoring program consisted in the implementation of the processes in the Docker scenario (see Sec. 4.3.1). Hence, it was decided to run the different services inside separate docker containers interacting with each other. In particular, three containers are created: one of them includes the two Python scripts and the shell script, another one includes the InfluxDB service and the last one the Grafana service. The InfluxDB and Grafana container images can be easily downloaded from Docker Hub, the world’s largest library for docker images, whereas the image of the container that includes the scripts is created via a custom Dockerfile. The task of managing the containers, i. e. building their images, running them, exposing the proper ports (port 8086 for InfluxDB and port 3000 for Grafana) and making them interact with each other, is handled by the docker-compose tool, whose instructions are encoded

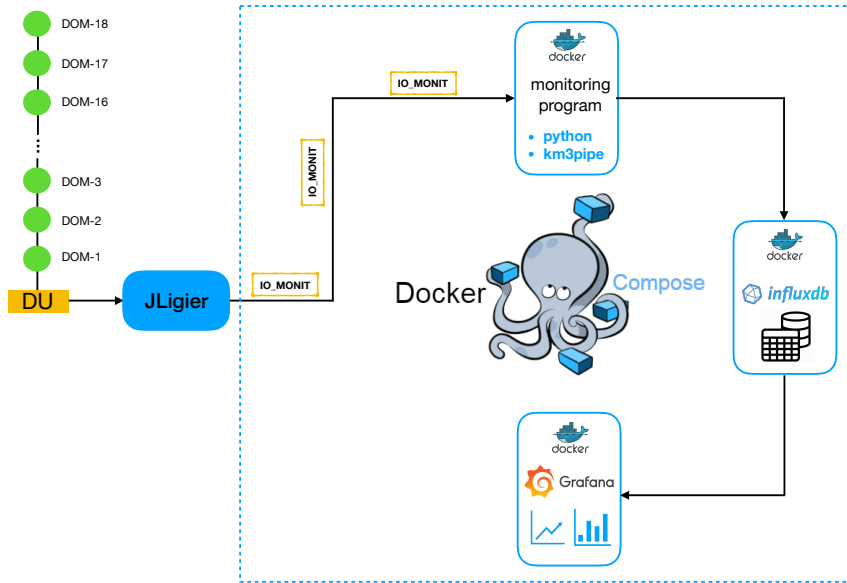


Figure 4.19: Scheme of the processes behind the TMCH monitoring multi-processes program. The Python programs, the InfluxDB service and the Grafana service run inside separate containers, managed by the docker-compose tool.

in a YAML file. This approach automatizes the processes running behind the scenes, so that the end user needs just to docker-compose the YAML file and can then freely navigate the Grafana web interface. In addition, this system allows the monitoring program together with the required services to be easily distributed as if it was a one-block item anywhere it may be need, e. g. on the “full WR” test bench BCI Bastion server for monitoring the TMCH channel of the “full WR” setup.

As a first test for checking the appropriate functionalities of the Python programs and the docker implementation, the containers were run for a preliminary data taking test on the BCI Bastion server of the “Broadcast” setup. On the one hand, this gave me the opportunity to verify that the monitoring program worked indeed as expected; on the other hand, it allowed me to create the Grafana dashboards with plots and bar charts useful for visualizing and monitoring the stability and integrity of the TMCH data stream, as one can see in Figs. 4.22,4.23. Once created, the dashboard configurations can be exported in order to be applied and replicated also elsewhere. In particular, during the said preliminary data taking test the occurrence of the clock reset phenomenon, explained in the next section, was observed. The fact that this event was correctly registered by the program and easily spotted by inspecting the dashboards showed the usefulness of this monitoring tool for the debugging of such events.

4.5.2 Clock reset issue

The clock reset phenomenon consists in the temporary and randomic reset of the clock of a CLB to its “zero” date, that is the 01/01/1970 - 00:00:00 . After few seconds though, the clock returns back to the current date, re-synchronizing. This error was first observed in ARCA and still has not found a proper explanation. Hence, it is still under investigation.

The clock reset has been observed during a monitoring session on the “Broadcast” test bench at the BCI thanks to the developed monitoring tool, as shown in Fig. 4.20: when such an error occurs, the incoming timeslice timestamp, i. e. the *packet time* (recalling the adopted terminology), shifts suddenly to the 01/01/1970 date, so that the time difference with the previous packet time, $T_{100\text{ms}}$, diverges from the expected value of 100 ms, becoming as large as $T_{100\text{ms}} \simeq -51$ years. Just after that, the clock remained de-synchronized for a few seconds while packets continued to arrive with the correct $T_{100\text{ms}} = 100$ ms; then, when the clock re-synchronizes shifting to the current date, a positive peak with $T_{100\text{ms}} \simeq +51$ years occurs. Therefore, a complete clock reset event can be clearly seen in the graph showing the evolution of $T_{100\text{ms}}$ over time as two peaks, one negative and one positive, intersperse by a period in which $T_{100\text{ms}} = 100$ ms. At the same time, when the clock shifts back to the 01/01/1970 also the transmission ratio $R_{\text{packet time}} = N_{\text{observed}}/N_{\text{expected}}^{\text{packet time}}$ undergoes a dramatic change, as the module of the denominator $N_{\text{expected}}^{\text{packet time}}$ increases drastically, causing the $R_{\text{packet time}}$ to approach zero for the whole time of the clock reset event. This can be seen in Fig. 4.21

4.5.3 Monitoring of the “full White Rabbit” setup

Once the monitoring program proved to be functioning and effective on the “Broadcast” test bench, it was ported to the “full WR” test bench. This gave me also the opportunity of testing the deployment operation of the program on a different server. Thus, I downloaded from the GitLab repository [14] the Dockerfile of my custom-made container and the YAML file with the instructions for the docker-compose, I modified the necessary configurations (e. g. the address of the JLigier process on the current Bastion server) and I simply executed the docker-compose command. At this point, the container proper execution is totally handled by the docker-compose and the operations completely automatized. Finally, connecting on a web browser to the test bench Bastion server where the program is running, on port 3000 which is the one exposed by the Grafana service (<http://131.154.102.188:3000>), I was able to connect to the Grafana interactive application, where I imported the dashboards that I set up and exported previously on the “Broadcast” test bench. These are shown in Figs. 4.22,4.23.

While the TTDC data stream was investigated for the study of the clock synchronization, also the TMCH data stream was monitored through the dashboards; during this period, about 9 days long, the data stream has proved to maintain the required stability. Neither loss of packets nor slowdowns were observed and no clock reset issues were found. Nevertheless, by checking the parameter related to the loss of synchronization (the bit value), it was observed that 5 CLBs sporadically lost the Track-phase, with a frequency of 1-2 occurrences in the monitored period, as concurrently noticed by looking at Fig. 4.17 from the TTDC data stream analysis. In fact, when a de-synchronization occurs, the corresponding bit value changes from “1” to “0”, as it can be seen in Fig. ,4.24.

4.5.4 Extension for multiple Detection Units

The monitoring program can be extended for analyzing data also from multiple Detection Units at the same time, as for the case with the real detector. In order to do that, some changes must be introduced. In particular, a containerized “JLigier mirror” process whose task is to receive TMCH data from the detector DUs and to tag each packet with the



Figure 4.20: Screenshots from the Grafana dashboard representing the plot of the difference T_{100ms} between two consecutive TMCH packets for CLB-1 of the “Broadcast” setup, when clock reset errors were observed. **Up:** positive and negative peaks with height equal to $T_{100ms} \simeq 51$ years (time difference between the 01/01/1970 and 07/05/2021) indicate the occurrence of a clock reset. In the shown time frame, 40 occurrences with a more or less regular frequency ($\simeq 2$ min. period) can be seen. **Bottom:** zoom on the time frame between two consecutive positive and negative peaks; after the clock resets to the 01/01/1970 date a negative peak appears, as the time difference between consecutive packets is between 01/01/1970 (current packet) and 07/05/2021 (previous packet). Then packets continue to arrive with the correct frequency, i. e. $T_{100ms} = 100$ ms while the clock is still back at 01/01/1970, and finally after few seconds the clock comes back to the current date and a positive peak appear, as the time difference between consecutive packets is between 07/05/2021 (current packet) and 01/01/1970 (previous packet).



Figure 4.21: Screenshot from the Grafana dashboard representing the plot of the transmission ratio $R_{packet\ time}$ for CLB-1 of the “Broadcast” setup, when clock reset errors were observed. The transmission ratio $R_{packet\ time} = N_{observed}/N_{expected}^{packet\ time}$ which is expected to be equal to one if no issue of any kind is present, drops drastically to zero during a clock reset event, as $N_{expected}^{packet\ time}$ grows sharply.

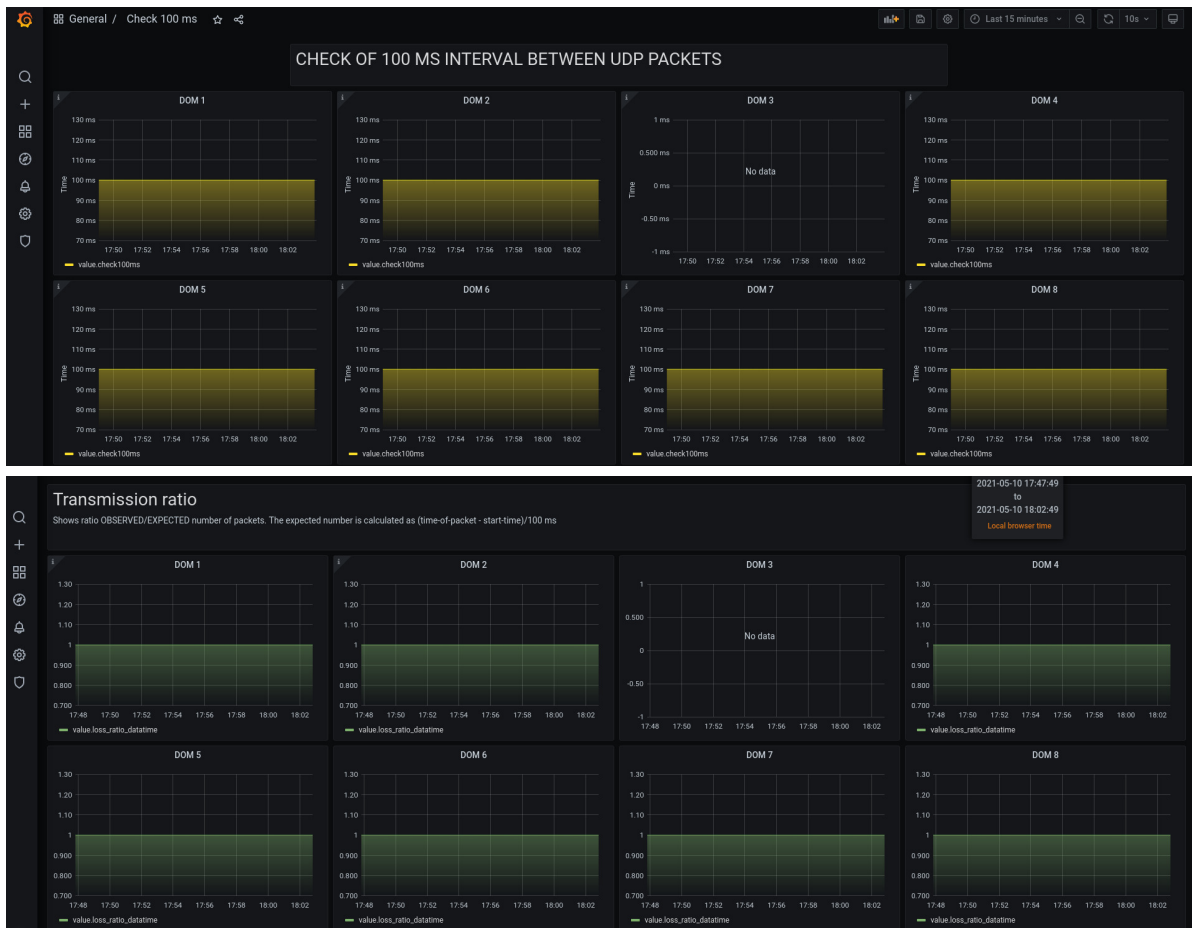


Figure 4.22: Screenshots of Grafana dashboards of the monitoring program. **Up:** plots of T_{100ms} over time for the different CLBs (DOMs). **Bottom:** plots of the transmission ratio $R_{packet\ time}$ over time for the different CLBs.



Figure 4.23: Screenshot of a Grafana dashboard of the monitoring program. This dashboard includes a summary of the information about DOMs of a DU: the run number, the synchronization status (Track-phase bit value), the plot of T_{100ms} over time, the delay between the *packet time* and the *machine time*, the clock reset counters, and bar plots showing the total number of arrived TMCH packets and the expected numbers $N_{packet\ time\ expected}$ and $N_{machine\ time\ expected}$.

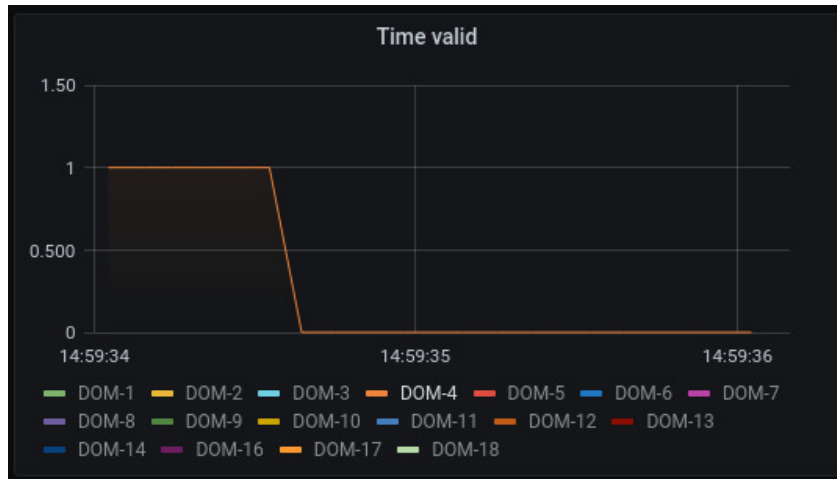


Figure 4.24: Screenshot of the panel representing the bit value which refers to the synchronization status of the CLBs. Values of CLB-4 are shown. When the CLB loses the Track-phase, the bit value goes to 0.

parent DU identity information is added. The process consists in a Python program exploiting km3pipe which connects to the primary JLigier, picks up TMCH packets coming from DOMs in DUs by subscribing the “IO_MONIT” tag, and changes their tag labelling them with their parent DU number, e. g. “IO_DU1”, “IO_DU2”, etc. This is done by accessing the detector DataBase where detector configuration information is stored and making the correct association between the DOM identity information contained inside each UDP packet and the corresponding Detection Unit to which the DOM belongs. The packets are then redistributed to another JLigier running on a separate container built on an available image which includes JPP; this takes on the role of the JLigier process in Fig. 4.19, dispatching monitoring packets according to the tags that specify their origin in terms of Detection Units.

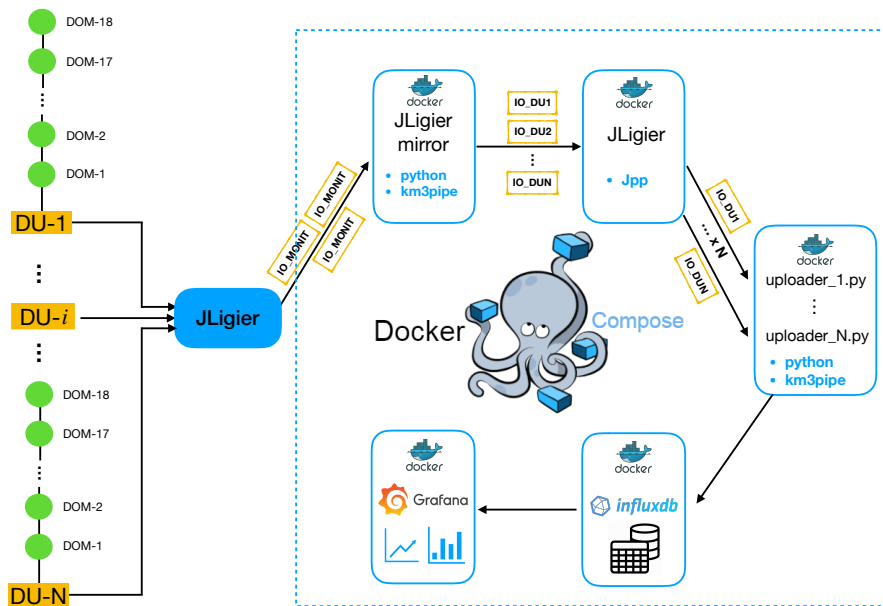


Figure 4.25: Extension of the monitoring program to multiple Detection Units.

The layout of this extension is depicted in Fig. 4.25. Inside the container which includes the code for analyzing packets several Python programs now run: each of them retrieves data from the JLigier by subscribing the tag of a specific Detection Unit, for a total number of running programs equal to the number of Detection Units. All of them write on the very same Influx database, specifying the DU number as an extra tag together with the DOM number. Finally, the database can be displayed on Grafana dashboards, where data from the different Detection Units can be easily filtered by selecting the desired DU tag.

4.6 Result discussion

The “full White Rabbit” setup at the BCI is a complex system including many hardware and software components specifically developed for this purpose. The fact that all the involved parts have been integrated together for the first time at the BCI test bench introduces a new level of complexity in the validation procedure. One of the key components of the system is the CLB. A prerequisite for the proper functioning of the CLB

is the ability of steering it, moving it along the states of the state machine implemented in its FPGA. Since the setup is composed by 19 CLBs, the management of a such large number of boards can be rather cumbersome and time-consuming if not handled appropriately. For this reason, the role of the CU is crucial in order to steer all the CLBs in a correct and automatized way. The development of the CU v10 was necessary in order to cope with the newly designed NG CLB firmware. I have contributed in testing and validating the CU v10, which is now running effectively on the Bastion server of the setup. This allowed me to proceed with the validation of the setup.

Time synchronization accuracy

As the White Rabbit technology has been chosen by the collaboration on the basis of the requirement of a sub-nanosecond time synchronization accuracy between the detector elements, the validation of the time synchronization of the setup is one of the most relevant aspects to consider. I have verified the sub-nanosecond synchronization accuracy between the CLBs of the setup in two ways. First, I carried out a measurement with the oscilloscope of the delays between the PPS signals produced by the CLBs, which provides an optimal indicator of the time offsets between CLBs. The results (see Fig. 4.7 for reference) have shown that accuracies on time synchronization much smaller than the nanosecond are achieved. Then, I have conducted a more extensive test exploiting the OctoPAES boards to emulate photon hits on PMTs. I have simulated the occurrence of simultaneous hits on a selected PMT on the CLBs and I verified the time synchronization by analyzing the delays between hit times, as reconstructed by the TDCs, embedded into TTDC packets, and processed by the whole DAQ chain. I carried out these measurements for a period of about nine days, after which I had to dismantle the setup since the CLBs were needed in another laboratory. During this period, I interrupted data taking several times to perform power cycles on the setup. Taking into account that the resolution of TDCs in the CLB is 1 ns, results (see Fig. 4.16 for reference) have shown that a nanosecond accuracy on time synchronization is achieved. Delay values kept constant after every power cycle, proving the stability of the system to power interruptions.

Time synchronization stability

The loss of Track-phase from different CLBs has been observed, with a frequency of 1-2 occurrences in the 9 days period. The loss of Track-phase causes TTDC packets to get discarded by the DataQueue process, so that the concurrent absence of TTDC data downstream of the DAQ chain has been observed, as one can see in Fig. 4.17. This issue was also seen in the monitoring program that I have developed, which displays online the synchronization status of the CLBs. An example of such an event is shown in Fig. 4.24. To recover the de-synchronized CLBs, the manual reboot has proven to be necessary. Thus, synchronization stability is not ensured and further investigations must be conducted to settle this misbehaviour. The causes of this issue can be various. The problem can be related to a malfunction of the crystal oscillator implemented in the CLB FPGA and which provides the clock signal of the CLB. For this reason, electronic experts in the collaboration have been notified and a revision of the oscillator is currently being carried out. The problem can also lie within the WR-PTP packet data stream from the DWRS or the WWRSs. Therefore, a proposed test consists in monitoring the WR-PTP

data stream from the switches and verifying eventual packet losses which may cause the de-synchronization of CLBs. Data throughput from CLBs can also be varied, verifying whether throughput values correlate with de-synchronization occurrences. In general, increasing the observation period can allow one to better inspect the frequency and the repetitiveness of such events. Moreover, problematic CLBs may be tested individually to check if the error still occurs. Finally, no clock reset events were observed.

Data stability and integrity

Throughput stability of TTDC and TMCH data streams has been monitored throughout the nine days observation period via the Linux *dstat* tool. I have verified that the nominal streaming, calculated taking into account the number of running CLBs and the PMT rates, was kept over time. Considering the 16 running CLBs, the PMT rates which are set to ~ 5.08 kHz, and the payload of UDP packets containing digitized hits, a nominal throughput value of $31 \text{ PMTs} \times 5.08 \cdot 10^3 \text{ Hz} \times 6 \text{ B} \times 16 \text{ CLBs} \simeq 15 \text{ MBps}$ is expected. Moreover, I have exploited the monitoring program that I have developed to inspect the stream of TMCH packets and to analyze its stability. In particular, the time period between consecutive packets sent by the CLBs and the delay between the packet timestamp and the packet processing time on the machine have been monitored. The former showed itself to keep stable at the nominal value, equal to 100 ms as one packet is sent every timeslice. Moreover, no evidences of slowdowns were found analyzing delay values, which also kept constant over time. During data taking, no malformed packets or packet losses were observed either for the TTDC data stream and for the TMCH data stream. The check on the TTDC packets has been done by looking at the hit occurrences over time (see Fig. 4.17 for reference), finding no evidences of missing packets. In fact, it is worthy to remember that the gaps which can be seen in the plot refer to CLBs which lost the Track-phase. In such cases, the corresponding TTDC packets are discarded by the DataQueue process. The absence of TMCH missing packets was verified by checking the time period between consecutive packet timestamps and finding no discrepancies from the nominal 100 ms value. This proves the absence of malformed or missing packets, as smaller or larger values than the nominal one may indicate.

Data consistency

Checks on data consistency for both TTDC and TMCH packets have been performed. Concerning TTDC packets, the consistency of the hit times with the nominal values is shown by the correct L1 trigger condition identification and the detection of the TTDC packets themselves. Furthermore, I have analyzed the Time Over Threshold values of the hits and verified that they correspond to the nominal value of 25 ns as set in the MIF file of the OctoPAES (see Fig. 4.18 for reference). Regarding TMCH data consistency, I have verified, exploiting the CLBSwissKnife tool, that the PMT rates kept the nominal values over time. Parameters of monitoring sensors (AHRS sensors, accelerometer, temperature sensors,...) have been also analyzed and compared to Slow Control data (see Fig. 4.10 for reference), which follow a completely independent channel. Values showed themselves to be in perfect agreement.

Conclusions

The current network configuration for the KM3NeT-ARCA detector involves the first 32 Detection Units and its Data Acquisition system is based on the “Broadcast” scenario. This foresees that every single DOM has a unidirectional uplink to communicate with the shore station, delivering data and Slow Control reply messages, whereas the shore station exploits a unique unidirectional downlink to communicate with all DOMs. However, this approach is not scalable to a large number of Detection Units due to the limitation on the number of fibres which can fit inside the submarine cable that runs along the seabed, connecting the shore station to the off-shore detector. In view of the next completion of the KM3NeT detector, consisting of 230 DUs, the solution is to move to a “full White Rabbit” configuration: this implies the placement of two “Wet” White Rabbit switches inside the Base Module of each Detection Unit, connected with bi-directional links to the DOMs of the string and to the “Dry” White Rabbit switches located on-shore. Traffic from DOMs will hence be routed through the two cables which connect the switches to the shore station, providing a reduction of a factor 10 in the number of required fibres inside the submarine cable. To achieve this result, it is essential to test and validate as a whole the new technologies and developments, both from the electronics and from the software side, designed and engineered for this future network architecture. For this purpose, at the Bologna Common Infrastructure laboratory, we have built a test-bench setup that recreates the full Data Acquisition chain from a complete Detection Unit-like string in the Full White Rabbit configuration, comprising 19 CLBs v4, two Wet White Rabbit switches and the Dry White Rabbit switch, together with the required networking infrastructure and Data Acquisition processes. The main goal of this thesis is focused on the validation of this setup, evaluating several factors and considering both the optical (TTDC) and monitoring (TMCH) data streams. Checks have been performed during a follow-up period of nine days of data taking. First of all, the throughput stability of the data streams has been verified to keep stable at the nominal value over time, calculated taking into account the number of running CLBs, the PMT hit rates and the packet payload. Then, data integrity has been evaluated, reporting no occurrences of malformed packets or of packet losses. Consistency of data has been verified by inspecting PMT rates and Time Over Threshold values and finding no evidences of deviations from the nominal values, and by comparison of TMCH data with Slow Control data, again finding complete accordance between them. Finally, the time synchronization of the system has been assessed. The nanosecond accuracy on time synchronization, ensured by the White Rabbit Precision Time Protocol, has been verified analyzing both the Pulse Per Second signals extracted from the CLBs and the delays between emulated PMT hit times on the CLBs. Nevertheless, the synchronization stability throughout the observation period has been compromised due to the observed sporadic loss of Track-

phase from some of the CLBs of the setup. For the synchronization to be restored, an external intervention, consisting in the manual reboot of the board, has proven to be necessary. This misbehaviour will have to be more deeply investigated, possibly extending the observation campaign, and its origin identified before proceeding with the conformity report. In this regard, the monitoring program tool that I have developed has proven to be extremely useful for the online supervision of the synchronization status of the CLBs and its usage can be expanded by displaying not only parameters related to the status of the monitoring channel data stream but also the data content itself, that is the values registered by the sensors on the CLBs. Beside this, the extended and adapted for multiple Detection Units version of the monitoring program has been recently deployed at the ARCA shore station servers and configured for its application on the current six Detection Units of the detector.

Acronyms

AGN Active Galactic Nuclei.

AIACE Automatic Installation And Configuration procedurE.

AMANDA Antarctic Muon And Neutrino Detector Array.

ARCA Astroparticle Research with Cosmics in the Abyss.

BCI Bologna Common Infrastructure.

CC Charged Current.

CLB Central Logic Board.

CMB Cosmic Microwave Background.

CPLD Complex Programmable Logic Device.

CR Cosmic Rays.

CU Control Unit.

DAQ Data AcQuisition.

DBI DataBaseInterface.

DBW DataBaseWriter.

DFES DOM Front End Switches.

DIS Deep Inelastic Scattering.

DM Detector Manager.

DOM Digital Optical Module.

DSA Diffusive Shock Acceleration.

DU Detection Unit.

DUMAND Deep Underwater Muon and Neutrino Detector.

DWRS Dry White Rabbit Switch.

EM Electromagnetic.

FAD Fast Acquisition Data.

FPGA Field Programmable Gate Array.

GRB Gamma Ray Burst.

GW Gravitational Wave.

GZK Greizen-Zatsepin-Kuzmin.

JB Junction Box.

LAN Large Area Network.

LOM Launcher vehicle for Optical Modules.

LVDS Low Voltage Differential Signals.

MAC Media Access Controller.

MCP Master Control Program.

MEOC Main Electrical-Optical Cable.

NC Neutral Current.

NG Next Generation.

OP OctoPAES.

ORCA Oscillation Research with Cosmics in the Abyss.

PAO Pierre Auger Observatory.

PB Power Board.

PCB Printed Circuit Board.

PLL Phase Locked Loop.

PMT Photomultiplier Tube.

PPS Pulse Per Second.

PWNe Pulsar Wind Nebulae.

QE Quasi Elastic scattering.

QUOLAM QUasi On-Line Analysis and Monitoring.

RES Resonant production.

SC Slow Control.

SCB Switch and Control Board.

SCBD Slow Control and Base Data.

SCSF Star Centre Switch Fabric.

SDN Software Defined Networks.

SFP Small Form-factor Pluggable.

SNO Sudbury Neutrino Observatory.

SNR Supernova Remnants.

SPI Serial Peripheral Interface.

SRP Simple Retransmission Protocol.

TA Telescope Array.

TCP Transmission Control Protocol.

TDC Time to Digital Converter.

TM TriDAS Manager.

TOA Time Of Arrival.

ToT Time over Threshold.

TriDAS Trigger and Data Acquisition System.

UDP User Datagram Protocol.

UHECR Ultra High Energy Cosmic Rays.

UTC Coordinated Universal Time.

WR White Rabbit.

WRPC White Rabbit time precision Protocol Core.

WRS White Rabbit Switch.

WRS-BR White Rabbit Switch Broadcast.

WWRS Wet White Rabbit Switch.

Bibliography

- [1] KM3NeT Website, <https://www.km3net.org>.
- [2] White Rabbit website, <http://www.ohwr.org/projects/white-rabbit>.
- [3] Seven Solution website, <https://sevensols.com/white-rabbit-technology/>.
- [4] Glenair website, <https://www.glenair.com/>.
- [5] CLBSwissKnife wiki page, https://wiki.km3net.de/index.php/CLB_Swiss_Knife.
- [6] Docker website, <https://docker.com>.
- [7] Docker Hub website, <https://hub.docker.com/>.
- [8] KM3Pipe website, <https://km3py.pages.km3net.de/km3pipe/index.html>.
- [9] CU v10 downsampling checks, https://github.com/francescobenfenati/Supernova2/tree/main/MONITORING_CHECKS/Images.
- [10] Linux dstat tool repository, <https://github.com/dstat-real/dstat>.
- [11] Full-WR time synchronization repository, <https://github.com/francescobenfenati/Supernova2/tree/main/Phase2>.
- [12] Grafana website, <https://www.grafana.com>.
- [13] InfluxDB website, <https://influxdata.com>.
- [14] GitLab TMCH monitoring repository, https://git.km3net.de/daq/shore-station/tmch_monitoring.
- [15] *KM3NeT: Conceptual Design Report*. <https://www.km3net.org/wp-content/uploads/2015/07/CDR-KM3NeT.pdf>.
- [16] M. AARTSEN ET AL., *The IceCube Neutrino Observatory - Contributions to ICRC 2017 Part II: Properties of the Atmospheric and Astrophysical Neutrino Flux*, ArXiv: 1710.01191, (2017).
- [17] —, *Multimessenger observations of a flaring blazar coincident with high-energy neutrino IceCube-170922A*, *Science*, 361 (2018), p. eaat1378.

- [18] —, *Neutrino emission from the direction of the blazar TXS 0506+056 prior to the IceCube-170922A alert*, *Science*, 361 (2018), pp. 147–151.
- [19] —, *IceCube Search for High-Energy Neutrino Emission from TeV Pulsar Wind Nebulae*, *Astrophys. J.*, 898 (2020), p. 117.
- [20] M. AARTSEN ET AL., *Transient optical emission from the error box of the γ -ray burst of 28 February 1997*, *Nature*, 591 (2021), pp. 220–224.
- [21] M. G. AARTSEN ET AL., *Measurement of the ν_μ energy spectrum with icecube-79 - icecube collaboration*, *Eur. Phys. J. C*, 77 (2017), p. 692.
- [22] R. ABBASI ET AL., *Study of Ultra-High Energy Cosmic Ray composition using Telescope Array’s Middle Drum detector and surface array in hybrid mode*, *Astropart. Phys.*, 64 (2015), pp. 49–62.
- [23] B. ABBOTT ET AL., *Observation of Gravitational Waves from a Binary Black Hole Merger*, *Phys. Rev. Lett.*, 116 (2016), p. 061102.
- [24] —, *Gravitational Waves and Gamma-rays from a Binary Neutron Star Merger: GW170817 and GRB 170817A*, *Astrophys. J. Lett.*, 848 (2017), p. L13.
- [25] —, *Multi-messenger Observations of a Binary Neutron Star Merger*, *Astrophys. J. Lett.*, 848 (2017), p. L12.
- [26] A. ABEYSEKARA ET AL., *Very high energy particle acceleration powered by the jets of the microquasar SS 433*, *Nature*, 564 (2018), pp. 82–85.
- [27] S. ADRIAN-MARTINEZ ET AL., *Measurement of the atmospheric ν_μ energy spectrum from 100 GeV to 200 TeV with the ANTARES telescope*, *Eur. Phys. J. C*, 73 (2013), p. 2606.
- [28] —, *Letter of intent for KM3NeT 2.0*, *J. Phys. G*, 43 (2016), p. 084001.
- [29] M. AGERON ET AL., *ANTARES: the first undersea neutrino telescope*, *Nucl. Instrum. Meth. A*, 656 (2011), pp. 11–38.
- [30] Q. AHMAD ET AL., *Direct evidence for neutrino flavor transformation from neutral current interactions in the Sudbury Neutrino Observatory*, *Phys. Rev. Lett.*, 89 (2002), p. 011301.
- [31] S. AIELLO ET AL., *Characterisation of the Hamamatsu photomultipliers for the KM3NeT Neutrino Telescope*, *JINST*, 13 (2018), p. P05035.
- [32] —, *KM3NeT front-end and readout electronics system: hardware, firmware and software*, *J. Astron. Telesc. Instrum. Syst.*, 5 (2019), p. 046001.
- [33] —, *Sensitivity of the KM3NeT/ARCA neutrino telescope to point-like neutrino sources*, *Astropart. Phys.*, 111 (2019), pp. 100–110.
- [34] —, *Deep-sea deployment of the KM3NeT neutrino telescope detection units by self-unrolling*, *Journal of Instrumentation*, 15 (2020), pp. P11027–P11027.

- [35] —, *The Control Unit of the KM3NeT Data Acquisition System*, Comput. Phys. Commun., 256 (2020), p. 107433.
- [36] —, *Architecture and performance of the KM3NeT front-end firmware*, Journal of Astronomical Telescopes, Instruments, and Systems, 7 (2021), pp. 1 – 24.
- [37] A. ALBERT ET AL., *Search for High-energy Neutrinos from Binary Neutron Star Merger GW170817 with ANTARES, IceCube, and the Pierre Auger Observatory*, Astrophys. J. Lett., 850 (2017), p. L35.
- [38] R. ANTONUCCI, *Unified Models for Active Galactic Nuclei and Quasars*, Annual Review of Astronomy and Astrophysics, 31 (1993), pp. 473–521.
- [39] V. AYUTDINOV ET AL., *Results from the BAIKAL Neutrino Telescope*, in 28th International Cosmic Ray Conference, 5 2003.
- [40] J. BABSON ET AL., *Cosmic ray muons in the deep ocean*, Nucl. Phys. B Proc. Suppl., 14 (1990), pp. 157–161.
- [41] M. BARKOV AND G. KOGAN, *Infrared Afterglow of the Gamma Ray Burst GRB041219 as the Result of Reradiation from Dust in a Circumstellar Cloud*, Astrophysics, 48 (2005), pp. 369–373.
- [42] M. BOEZIO AND E. MOCCHIUTTI, *Chemical Composition of Galactic Cosmic Rays with Space Experiments*, Astropart. Phys., 39-40 (2012), pp. 95–108.
- [43] S. BRAIBANT, G. GIACOMELLI, AND M. SPURIO, *Particles and Fundamental Interactions*, Springer-Verlag Italia, 2012.
- [44] D. CALVO AND D. REAL, *The new clbv4 for the km3net neutrino telescope*, EPJ Web of Conferences, 207 (2019), p. 06003.
- [45] A. CASTELLINA, *AugerPrime: the Pierre Auger Observatory Upgrade*, EPJ Web Conf., 210 (2019), p. 06002.
- [46] T. CHIARUSI, L. CHIARELLI, E. GIORGIO, S. ZANI, AND S. CELLI, *The Software Defined Networks implementation for the KM3NeT networking infrastructure*, PoS, ICRC2017 (2018), p. 940.
- [47] R. CONEGLIONE, *Status and plans for the KM3NeT detectors*. Very Large Neutrino Volume Telescopes 2021 Conference, Valencia https://indico.cern.ch/event/639198/contributions/2964989/attachments/1653397/2645644/30_okumura-180523-ISVHECRI.key.pdf.
- [48] E. COSTA, F. FRONTERA, H. J., ET AL., *Discovery of an X-ray afterglow associated with the γ -ray burst of 28 February 1997*, Nature, 387 (1997), pp. 783–785.
- [49] G. DANBY, J. GAILLARD, K. GOULIANOS, L. LEDERMAN, N. MISTRY, M. SCHWARTZ, AND J. STEINBERGER, *Observation of high-energy neutrino reactions and the existence of two kinds of neutrinos*, Physical Review Letters, 9 (1962), pp. 36–44.

- [50] O. DELIGNY, *The energy spectrum of ultra-high energy cosmic rays measured at the Pierre Auger Observatory and at the Telescope Array*, PoS, ICRC2019 (2020), p. 234.
- [51] O. DELIGNY, K. KAWATA, AND P. TINYAKOV, *Measurement of anisotropy and the search for ultra high energy cosmic ray sources*, PTEP, 2017 (2017), p. 12A104.
- [52] E. FERMI, *On the Origin of the Cosmic Radiation*, Phys. Rev., 75 (1949), pp. 1169–1174.
- [53] J. A. FORMAGGIO AND G. P. ZELLER, *From eV to EeV: Neutrino cross sections across energy scales*, Rev. Mod. Phys., 84 (2012), pp. 1307–1341.
- [54] F. FRASCHETTI, *On the acceleration of ultra-high-energy cosmic rays*, Phil. Trans. R. Soc., 366 (2008).
- [55] T. GAISSER AND F. HALZEN, *IceCube*, Annual Review of Nuclear and Particle Science, 64 (2014), pp. 101–123.
- [56] T. K. GAISSER, R. ENGEL, AND E. RESCONI, *Cosmic Rays and Particle Physics*, Cambridge University Press, 2 ed., 2016.
- [57] T. GAL, *Live monitoring and quasi-online event reconstruction for km³net*, EPJ Web of Conferences, 116 (2016), p. 05003.
- [58] R. GANDHI, C. QUIGG, M. H. RENO, AND I. SARCEVIC, *Ultrahigh-energy neutrino interactions*, Astropart. Phys., 5 (1996), pp. 81–110.
- [59] E. GIORGIO, T. CHIARUSI, AND R. BRUIJN, *The Automatic Installation And Configuration Procedure for the Data Acquisition System of KM³NeT.*, PoS, ICRC2019 (2019), p. 898.
- [60] C. GIUNTI AND W. K. CHUNG, *Fundamentals of Neutrino Physics and Astrophysics*, Oxford University Press, 2007.
- [61] S. L. GLASHOW, *Resonant Scattering of Antineutrinos*, Phys. Rev., 118 (1960), pp. 316–317.
- [62] K. GREISEN, *End to the Cosmic-Ray Spectrum?*, Phys. Rev. Lett., 16 (1966), pp. 748–750.
- [63] C. HAACK AND C. WIEBUSCH, *A measurement of the diffuse astrophysical muon neutrino flux using eight years of IceCube data.*, PoS, ICRC2017 (2018), p. 1005.
- [64] T. M. HECKMAN AND P. BEST, *The Coevolution of Galaxies and Supermassive Black Holes: Insights from Surveys of the Contemporary Universe*, Ann. Rev. Astron. Astrophys., 52 (2014), pp. 589–660.
- [65] S. HEINZ AND R. SUNYAEV, *Cosmic Rays from Microquasars: a Narrow Component to the CR Spectrum?*, Astronomy & Astrophysics, v.390, 751-766 (2002), 390 (2002).

- [66] W. HOFMANN AND J. A. HINTON, *Cosmic Particle Accelerators*, Springer International Publishing, 2020.
- [67] D. HOOPER AND A. M. TAYLOR, *On the heavy chemical composition of the ultra-high energy cosmic rays*, *Astroparticle Physics*, 33 (2010), pp. 151 – 159.
- [68] G.-Y. HUANG AND Q. LIU, *Hunting the Glashow Resonance with PeV Neutrino Telescopes*, *JCAP*, 03 (2020), p. 005.
- [69] A. KARLE, *The Path from AMANDA to IceCube*, *Proc. IAU Symposium 288, Astrophysics from Antarctica*, (2012).
- [70] K. KAWATA ET AL., *TA Anisotropy Summary*, *EPJ Web Conf.*, 210 (2019), p. 01004.
- [71] K. KODAMA ET AL., *Observation of tau neutrino interactions*, *Phys. Lett. B*, 504 (2001), pp. 218–224.
- [72] W. R. LEO, *Techniques for Nuclear and Particle Physics Experiments*, Springer-Verlag Berlin Heidelberg, 1994.
- [73] Z. MAKI, M. NAKAGAWA, AND S. SAKATA, *Remarks on the Unified Model of Elementary Particles*, *Progress of Theoretical Physics*, 28 (1962), pp. 870–880.
- [74] A. MARGIOTTA, *Status of the KM3NeT project*, *JINST*, 9 (2014), p. C04020.
- [75] M. MARKOV, *On high energy neutrino physics*, in *10th International Conference on High Energy Physics*, 1960, pp. 578–581.
- [76] A. OBERMEIER, P. BOYLE, J. HÖRANDEL, AND D. MÜLLER, *The Boron-to-Carbon abundance ratio and galactic propagation of cosmic radiation*, *The Astrophysical Journal*, 752 (2012), p. 69.
- [77] K. OKUMURA, *Atmospheric neutrino flux measurement*. 20th International Symposium of Very High Energy Cosmic Ray Interactions, https://indico.cern.ch/event/639198/contributions/2964989/attachments/1653397/2645644/30_okumura-180523-ISVHECRI.key.pdf.
- [78] A. PALLADINO, M. SPURIO, AND F. VISSANI, *Neutrino Telescopes and High-Energy Cosmic Neutrinos*, *Universe*, 6 (2020), p. 30.
- [79] W. PAULI, *Pauli letter collection: letter to Lise Meitner*. Typed copy.
- [80] C. PELLEGRINO AND T. CHIARUSI, *The Trigger and Data Acquisition System for the KM3NeT neutrino telescope*, *EPJ Web Conf.*, 116 (2016), p. 05005.
- [81] A. A. PENZIAS AND R. W. WILSON, *A Measurement of excess antenna temperature at 4080-Mc/s*, *Astrophys. J.*, 142 (1965), pp. 419–421.
- [82] D. H. PERKINS, *Introduction to High Energy Physics*, Cambridge University Press, 2000.
- [83] B. PONTECORVO, *Inverse beta processes and nonconservation of lepton charge*, *Sov. Phys. JETP*, 7 (1958), pp. 172–173.

- [84] M. S. POTGIETER, *Solar Modulation of Cosmic Rays*, Living Reviews in Solar Physics, 10 (2013), p. 3.
- [85] F. REINES AND C. L. COWAN, *The Neutrino*, Nature, 178 (1956), pp. 446–449.
- [86] L. RESMI, *Radio Afterglows of Gamma Ray Bursts*, Journal of Astrophysics and Astronomy, 38 (2017), p. 56.
- [87] E. RICHARD ET AL., *Measurements of the atmospheric neutrino flux by super-kamiokande: Energy spectra, geomagnetic effects, and solar modulation*, Phys. Rev. D, 94 (2016), p. 052001.
- [88] M. SANGUINETI, *ANTARES and KM3NeT: The Latest Results of the Neutrino Telescopes in the Mediterranean*, Universe, 5 (2019), p. 65.
- [89] P. SOKOLSKY, *Observation of the GZK cutoff by the HiRes Experiment*, Nuclear Physics B - Proceedings Supplements, 196 (2009), pp. 67–73.
- [90] P. SOKOLSKY AND G. B. THOMSON, *Highest energy cosmic-rays and results from the HiRes experiment*, Journal of Physics G: Nuclear and Particle Physics, 34 (2007), pp. R401–R429.
- [91] M. SPURIO, *Probes of Multimessenger Astrophysics*, Springer International Publishing, 2018.
- [92] T. STANEV, *High Energy Cosmic Rays*, Springer-Verlag Berlin Heidelberg, 2 ed., 2010.
- [93] J. VAN PARADIJS, P. GROOT, T. GALAMA, ET AL., *Transient optical emission from the error box of the γ -ray burst of 28 February 1997*, Nature, 386 (1997), pp. 686–689.
- [94] S. VIOLA, M. ARDID, V. BERTIN, R. LAHMANN, C. PELLEGRINO, G. RICCOBENE, M. SALDAÑA, P. SAPIENZA, AND F. SIMEONE, *Acoustic positioning system for KM3NeT*, 08 2016, p. 1169.
- [95] E. WAXMAN AND J. N. BAHCALL, *High-energy neutrinos from astrophysical sources: An Upper bound*, Phys. Rev. D, 59 (1999), p. 023002.
- [96] C. WU, E. AMBLER, R. HAYWARD, D. HOPPES, AND R. HUDSON, *Experimental Test of Parity Conservation in β Decay*, Phys. Rev., 105 (1957), pp. 1413–1414.
- [97] E. YEN, *New Scaling Variable and Early Scaling in Single Particle Inclusive Distributions for Hadron-Hadron Collisions*, Phys. Rev. D, 10 (1974), p. 836.
- [98] G. ZATSEPIN AND V. KUZMIN, *Upper limit of the spectrum of cosmic rays*, JETP Lett., 4 (1966), pp. 78–80.

Ringraziamenti

Desidero ringraziare innanzitutto la mia relatrice Prof.ssa Annarita Margiotta e il mio correlatore Dr. Tommaso Chiarusi per il loro costante supporto e incoraggiamento e per avermi saputo guidare, con suggerimenti pratici sempre utili, nell'attività di ricerca e nella stesura dell'elaborato. Ringrazio inoltre tutti i membri del gruppo di ricerca KM3NeT di Bologna per aver riposto fiducia in me e avermi fatto sentire parte di loro, così come i membri del gruppo della BCI, a Bologna e non, il cui contributo è stato fondamentale per lo svolgimento del mio lavoro. Ringraziamenti speciali vanno poi a Luigi Degli Esposti per l'assistenza, la disponibilità e la pazienza che non ha mai mancato di fornire, e a Francesco, senza il quale tutto questo non sarebbe stato possibile. Desidero infine esprimere la mia gratitudine alla mia famiglia, per avermi sempre fornito gli strumenti per seguire le mie passioni e sostenuto in esse; ai miei amici, per avermi sopportato (non è un refuso) in questi anni e in questi mesi; ad Anna Stella, per l'amore dimostrato lungo tutto questo percorso costellato di gioie e soddisfazioni, ma anche di dolori e incertezze. A tutti loro vanno i miei più sentiti ringraziamenti.